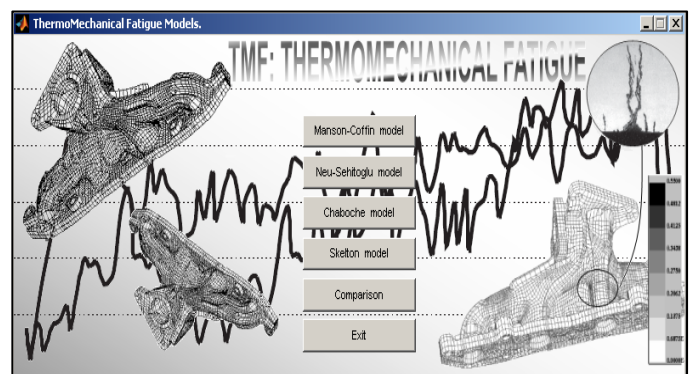
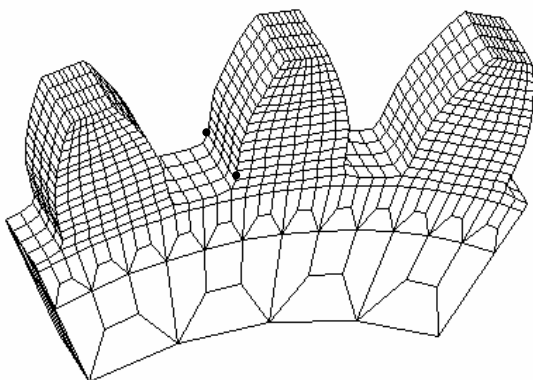
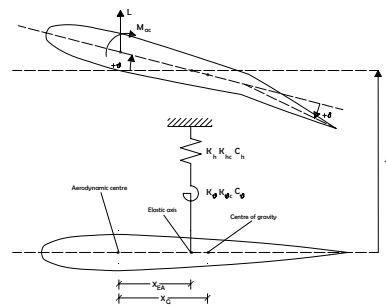
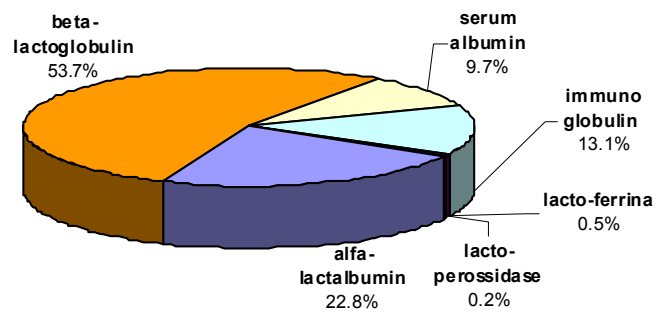
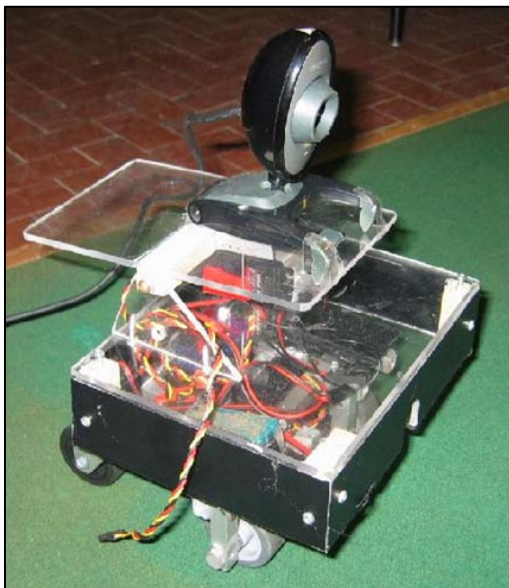


International Journal of Mechanics and Control

Honorary Editor: Guido Belforte

Editor: Andrea Manuello Bertetto



Editorial Board of the
International Journal of Mechanics and Control

Published by Levrotto&Bella – Torino – Italy E.C.

Honorary editors

Guido Belforte

Kazy Yamafuji

Editor: Andrea Manuello Bertetto

General Secretariat: Elvio Bonisoli

Anindya Ghoshal
Arizona State University
Tempe – Arizona – USA

Andrea Manuello Bertetto
University of Cagliari
Cagliari – Italy

Domenico Appendino
Prima Industrie
Torino – Italy

Stamos Papastergiou
Jet Joint Undertaking
Abingdon – United Kingdom

Kenji Araki
Saitama University
Shimo Okubo, Urawa
Saitama – Japan

Mihailo Ristic
Imperial College
London – United Kingdom

Guido Belforte
Technical University – Politecnico di Torino
Torino – Italy

János Somló
Technical University of Budapest
Budapest – Hungary

Bruno A. Boley
Columbia University,
New York – USA

Jozef Suchy
Faculty of Natural Science
Banska Bystrica – Slovakia

Marco Ceccarelli
LARM at DIMSAT
University of Cassino
Cassino – Italy

Federico Thomas
Instituto de Robótica e Informática Industrial
(CSIC-UPC)
Barcelona – Espana

Amalia Ercoli Finzi
Technical University – Politecnico di Milano
Milano – Italy

Lubomir Uher
Institute of Control Theory and Robotics
Bratislava – Slovakia

Carlo Ferraresi
Technical University – Politecnico di Torino
Torino – Italy

Furio Vatta
Technical University – Politecnico di Torino
Torino – Italy

Nunziatino Gualtieri
Space System Group
Alenia Spazio
Torino – Italy

Kazy Yamafuji
University of Electro-Communications
Tokyo – Japan

Giovanni Jacazio
Technical University – Politecnico di Torino
Torino – Italy

Official Torino Italy Court Registration
n.5390, 5th May 2000

Deposito presso il Tribunale di Torino
numero 5390 del 5 maggio 2000
Direttore responsabile:

Andrea Manuello Bertetto

Takashi Kawamura
Shinshu University
Nagano – Japan

Kin Huat Low
School of Mechanical and Aerospace Engineering
Nanyang Technological University
Singapore

International Journal of Mechanics and Control

Editor: Andrea Manuello Bertetto

Honorary editor: Guido Belforte

General Secretariat: Elvio Bonisoli

The Journal is addressed to scientists and engineers who work in the fields of mechanics (mechanics, machines, systems, control, structures). It is edited in Turin (Northern Italy) by Levrotto&Bella Co., with an international board of editors. It will have not advertising.

Turin has a great and long tradition in mechanics and automation of mechanical systems. The journal would will to satisfy the needs of young research workers of having their work published on a qualified paper in a short time, and of the public need to read the results of researches as fast as possible.

Interested parties will be University Departments, Private or Public Research Centres, Innovative Industries.

Aims and scope

The *International Journal of Mechanics and Control* publishes as rapidly as possible manuscripts of high standards. It aims at providing a fast means of exchange of ideas among workers in Mechanics, at offering an effective method of bringing new results quickly to the public and at establishing an informal vehicle for the discussion of ideas that may still in the formative stages.

Language: English

International Journal of Mechanics and Control will publish both scientific and applied contributions. The scope of the journal includes theoretical and computational methods, their applications and experimental procedures used to validate the theoretical foundations. The research reported in the journal will address the issues of new formulations, solution, algorithms, computational efficiency, analytical and computational kinematics synthesis, system dynamics, structures, flexibility effects, control, optimisation, real-time simulation, reliability and durability. Fields such as vehicle dynamics, aerospace technology, robotics and mechatronics, machine dynamics, crashworthiness, biomechanics, computer graphics, or system identification are also covered by the journal.

Please address contributions to

Prof. Guido Belforte
Prof. Andrea Manuello Bertetto
PhD Eng. Elvio Bonisoli

Dept. of Mechanics
Technical University - Politecnico di Torino
C.so Duca degli Abruzzi, 24.
10129 - Torino - Italy - E.C.

e_mail: jomac@polito.it

Subscription information

Subscription order must be sent to
the publisher:

Libreria Editrice Universitaria
Levrotto&Bella
2/E via Pigafetta – 10129 Torino – Italy

www.levrotto-bella.net
e_mail: info@levrotto-bella.net
tel. +39.011.5097367
+39.011.5083690
fax +39.011.504025

LOW COST INDOOR NAVIGATION SYSTEM FOR AUTONOMOUS VEHICLE

S. Chiesa, V. De Iakovo, G. Malnati, M. Murciano, K. M. Pluciński, F. Stesina, C. Zunino

Politecnico di Torino, Torino, 10129, Italy

ABSTRACT

This paper presents low cost navigation system for autonomous vehicles, that navigate indoor in known environment. The navigation bases on estimated change of vehicle's position due to given command and is updated by means of recognition of images taken by onboard camera. The position calculation bases on finding on the image the relative distances, from camera's point of view, between the light landmarks, that have known position in reference environment. Entire system has been integrated under Microsoft Windows XP and Linux environment to make possible future application of PC104 as the controller.

Keywords: robotic vehicle, autonomous navigation, image recognition, surveillance, indoor

1 INTRODUCTION

The concept of low cost navigation system has been developed for needs of autonomous indoor surveillance vehicle Autonomous Robotic Guardian&Observer (ARGO) developed by AeroSpace System Engineering Team (ASSET) at Politecnico di Torino (Polytechnic of Turin).

In classical sense the term navigation applies to the process directing a ship to its destination. This process consists of three repeating steps. In the first one the navigator determines the ship's position on a chart as accurately as possible. In the second step he relates its position to the destination and possible hazards. In the third step, basing on this information, navigator sets the new course of the vessel. In case that is going to be described in article, the process is similar. The vehicle has to estimate its position, confront it with the position of the destination, and then start its route to desired destination.

In the process described above, the most difficult element is to determinate the actual position. In outdoor cases in common use is GPS (Global Positioning System). In indoor

cases the situation is much complex and such system can't be used.

The autonomous vehicle ARGO has been designed for indoor surveillance (example: institutes, museums etc...). It has to navigate in known environment. One of the considered navigational solutions is application of inertial navigation. Big disadvantage of Inertial Measurement Unit (IMU) is that it usually suffer from accumulated error. To cancel such error has been thought the application of image recognition system, that would update the vehicle's position (if necessary) by recognition of the system of landmarks constituted by light sources placed in some rooms on the robot's way.

To verify such idea the simplified version of autonomous vehicle (rover), SRL (System of Reference Lights) and test rig has been created. The position of vehicle is calculated by adding of movements, that are responses for given command, measured before the experiment. Because of the physical imperfection of the system, the response (understood as movement of the vehicle) varies for the given commands. It means, that with the number of given commands the difference between real vehicle's position and calculated position is growing up. Such system in simplified way is simulating increasing error between reality and calculated position, as it is in case of use of IMU. Vehicle is expected to follow the path of WP (WayPoint). At each waypoint rover's position is updated by means of interpretation of the image of SRL taken by on board camera. The system has been tested, by ASSET, at Polytechnic of Turin in January-April 2008.

Contact author: S. Chiesa¹, V. De Iakovo², G. Malnati³, M. Murciano⁴, K. M. Pluciński⁵, F. Stesina⁶, C. Zunino⁷

¹ sergio.chiesa@polito.it

² valerio.deiacovo@polito.it

³ giovanni.malnati@polito.it

⁴ marco.murciano@polito.it

⁵ krzysztof.plucinski@polito.it

⁶ fabrizio.stesina@polito.it

⁷ claudio.zunino@polito.it

2 HARDWARE CONFIGURATION

The system is composed by (Figure 1):

- Personal Computer (PC) and remote controller;
- Rover with receiver, motors and webcam;
- System of Reference Lights.

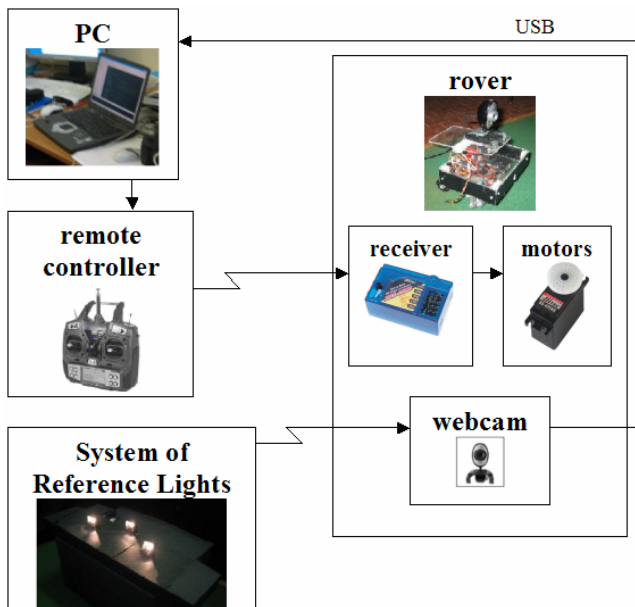


Figure 1 System's architecture.

PC is hosting control algorithm. Commands are being send by remote controller attached to PC. Rover receives commands by means of receiver and actuates motors. Eventual position update is effectuated by means of webcam, that sends information to PC by means of Universal Serial Bus (USB) cable.

2.1 PERSONAL COMPUTER

The system has been integrated in Microsoft (MS) Windows XP and Linux environment.

For system integration under Microsoft Windows XP has been used

Acer Aspire 1604LC; Pentium 4; 2,8 GHz; 512 Mb RAM computer.

For system integration under Linux has been used HP Pavillon ZV 6069EA; 2,4 GHz; 1,2 Gb RAM, AMD64 CPU computer.

2.2 REMOTE CONTROLER

For the needs of the experiment has been used the normal radio remote controller, which is used usually for flying models control (HI TEC OPTIC 6, 6 channel digital proportional FM radio control system).

According to [1], the controller has six, proportional, independent channels. The remote controller is equipped with the port, which usually is used to connect other remote controller, normally controlled by instructor during the student training phase. The port is called the student-master port. In considered case this port is connected to the PC

serial port (RS 232). By this port the computer can manage all the six cannels, giving the control signals.

The signal transmitted by one of the six cannels is the square wave, with invariant amplitude (0 – 5 V). Such a signal is generated from the “monostable oscillating” circuit, regulated by the potentiometer based on the proportional resistance, given by the command, that vary the duration of the impulse (5 V).



Main technical data	
Channels	6 (FM/Q-PCM signal)
Channels type	Proportional
Trim	Digital
Band	40 MHz
Flight Mode	3 (Manual, semiautomatic, automatic)
Dimensions	190 mm x 175 mm x 40 mm

Figure 2 Remote controller and its characteristics.

2.3 ROVER

As the vehicle has been adapted undercarriage and control system of differential rover described in [1] and [2] used before for various purposes.

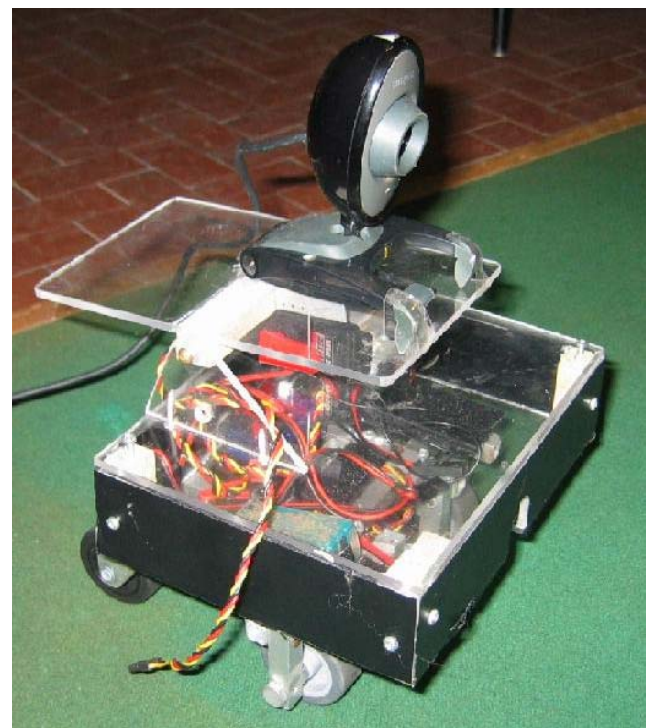


Figure 3 Rover assembled for autonomous navigation tests.

On the board of the rover are placed: receiver, 2 motors, camera and battery.

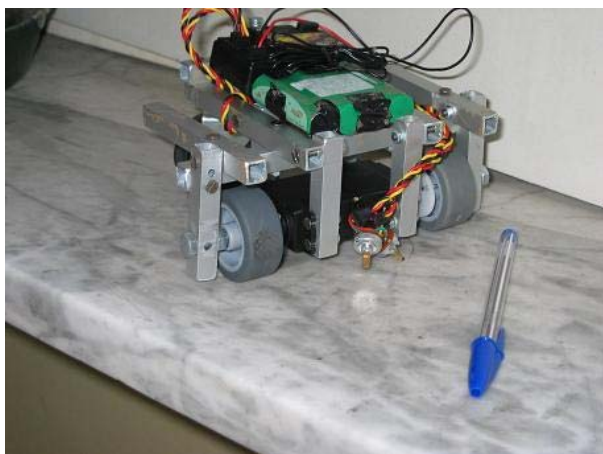


Figure 4 Undercarriage and control system of the rover.

2.3.1 Receiver

As on-board vehicle's receiver has been used HITEC HFS-05MJ.



Figure 5 Receiver.

2.3.2 Motors and driving system

Rover has been equipped with two HITEC HS-475 HB servomechanisms commonly used in aeromodeling (Figure 6).



Figure 6 HITEC HS-475 HB servomechanism.

Used servos consist of the electric motor, the system that controls that motor and the multistage gearbox (of high reduction level). The shaft of the last gearbox stage is connected to the position transducer in the form of

potentiometer. From the electronic point of view, the servo is connected to the relative channel of the receiver by means of three-polar cable (mass, feeding, signal). The transducer is connected to the circuit that generates the square impulses between 1 and 2 ms (depends of the resistance value of the transducer, with the identical logic as for remote controller transmitter). Signals that comes from receiver are being send into the comparator's circuit, that compare the duration of the signal. If the impulse generated by the transducer's circuit is different from the one that comes from receiver, the comparing circuit feeds the motor, giving also the correct polarity to make it rotate in the correct direction (in the way to make the difference if impulse duration smaller). During the motor's motion, the position of the transducer changes, what makes the changes in the duration of the signal generated by its circuit. The process last up to the moment when the equal duration of the impulses is verified. In practice, the logic of the command of the servo is following the signal that is coming from remote controller up to the moment when the servo's circuit will be able to generate the equal signal, so will obtain the result of positioning the servomechanism with the angle equal to the desiderated, given by transmitter.

For the purposes of giving torque to the driving wheels, mentioned servomechanisms has been used, but with some changes implemented by ASSET in the way, that the servo is controlled not in the position, but velocity. The modification has been obtained by physical disconnection of the position transducer from the last stage of the gearbox and elimination of the mechanical movement limiters. The choice to use this kind of solution instead of the use of classical motor was caused by the possibility of having the motor easily interfaced with remote control's receiver and use of the good multi stage gearbox (with high reduction level) originally integrated with servo.

The modified servos are used as the driving motors of the anterior wheels, while posterior wheels remain orientable. The velocity command is realized by contemporary work of both motors with the same velocity. The change of the direction command is realized by differential work of motors.

At the Figure 4 it is possible to see the transducers mechanically disconnected from the shafts of the gearbox and outside of the servos boxes, but still connected to the electronic circuits. The transducers are still giving the reference signal. To make the system work correctly they need to be set up in the position that give the signal equal to the signal generated by remote controller when the command is set up to 0.

Very interesting is the solution of the driving wheel suspension realized by the screw in the aluminum tube supported directly, by the structure, from only one side of the wheel. From the other side to the wheel is attached the shaft that connects servo and wheel. Because of the fact that the load caused by the Mini-Rover weight is taken by described suspension and the suspension of the other wheels the shaft carries only torsion loads.

2.3.3 Camera

As on-board vehicle's receiver has been used CREATIVE LABS INC VF-0050 webcam with resolution 320x240 pixels. Camera is connected with PC by USB cable.



Figure 7 CREATIVE LABS INC VF-0050

2.4 SYSTEM OF REFERENCE LIGHTS

System of Reference Lights (SRL) physically is made from wooden board with attached three 3,8 V light bulbs (supplied from the battery) and the switch. All the surfaces are covered black. All bulbs are in black hoods to minimize illumination of the environment. Position of the light sources is fixed and known. All bulbs are on the plane parallel to the ground. The middle light source is placed "not in line" (deeper) than other bulbs, so looking from above, the bulbs can be seen as placed in the vertices of the triangle. Schematic view of the SRL can be seen on the Figure 11.



Figure 8 System of Reference Lights.



Figure 9 System of Reference Lights without black cover.

3 SOFTWARE CONFIGURATION

As the starting point, for algorithm verification, the system has been integrated under MS Windows XP. The final point would be the application of embedded computer in PC104 standard that could be placed on-board of the rover. Unfortunately small dimensions of the adapted rover, makes on-board physical placement of PC104 hazardous. Additionally variances between PC104 versions would cause the significant waste of time, while adapting periphery devices in case of change of the embedded computer, or mentioned devices in case of system upgrade. Because of these reasons it has been decided to limit, at this stage of system development, to integrate software and hardware under Linux environment. Such operating system has been chosen because of its wide use by PC104 embedded computer standard.

All the installed software has been created in C programming language and is working on the PC (Figure 1).

3.1 SYSTEM DESCRIPTION

As it has been said before, in the future, the rover is expected to navigate with on-board PC104 computer. That is why the system under Linux has been configured in the way, that can be relatively easily adapted to such computer.

3.1.1 Embedded Linux development environment

Considered development platform is an ultra low power PC104 compatible single board microcomputer based on the Intel 400MHz PXA255 XScale Reduced Instruction Set Computer (RISC) microprocessor. The PXA255 is an implementation of the ARMv9 compliant Intel XScale microarchitecture, combined with a comprehensive set of integrated peripherals including a flat panel graphics controller (not available for used development board), a Direct Memory Access (DMA) controller, an interrupt controller and a real time clock and multiple serial ports (four RS 232 and two USB 1.1).

Mentioned board includes an Embedded Linux distribution, featuring a compact implementation of the GNU/Linux operating system based on the 2.6 Linux kernel release or a MS Windows XP Embedded Operating System (OS). The Linux version has been optimized in order to be used on applied platform, by customizing the kernel binary with the actual supported hardware: this kernel has been pre-loaded and configured into the embedded Flash. This offers an embedded version of Linux with a proven background, combined with a high reliability journaling Flash File System (NOTE: a journaling file system is an archive database where files and relative transactions are stored and indexed in order to guarantee the highest levels of robustness with respect to power-supply and/or hardware failures).

3.1.2 Development architectures and configurations for Embedded Systems

The basic embedded system development architectures can be divided into three main configurations (linked,

removable storage and standalone setup), whose classification depends upon:

- The existing relationship between the host environment (our PC in this case) and the target machine;
- The possibility of connecting different devices to the target environment;
- The applicative independence with respect to the possibility of developing software without any other intermediate step (i.e., directly, without compiling and distributing the code from a machine to a different one).

In the linked setup configuration, host and target interfaces are always connected via wired interfaces (i.e., serial or ethernet). The host environment is a desktop environment suitable for editing, compiling and possibly debugging the code, while the target is just the execution environment for pre-compiled binaries, once they are transferred using the previously mentioned connection.

In the removable storage setup, the host represents just a development (and deployment) environment, while the target uses the binaries stored on a removable media by the host, and executes them. Finally, the standalone setup incorporates the development feature and the execution capability within the same machine. This requires the target to be endowed of an adequate storage capacity and a of complete development and debugging environment.

3.1.3 Cross-development toolchain

A cross-development toolchain is a prerogative of the linked setup and of the removable storage setup configurations. When a cross-development architecture is present, the host machine features at least a compiler (e.g., Gnu CC or gcc) and a debugger (e.g., GNU debugger (DB) or gdb), tuned in such a way that the former is able to execute on the host producing code that is runnable on the target, and the latter is capable of inspecting the execution on a remote machine.

A cross-development environment is mandatory whenever the host and the target architecture differ (e.g., the host is an x86 machine and the target features an ARM CPU). Examples of cross-development environments are MS Visual Studio or MS Platform Builder. An open source distribution of cross-development tools is also available for Linux, and it is called Embedded Linux Development Kit (ELDK).

3.1.4 Architecture used

For the purpose of the project has been used a MS Windows XP Embedded architecture and a standard Linux (kernel v. 2.6.9) distribution, compiled for ARMv9.

Cross-development environment used is MS Visual Studio for the Windows XP Embedded application and the standard GNU toolchain for Linux.

3.1.5 Picture grabbing procedure

Grabbing pictures from the capture device is one of the most expensive side activities related to the rover navigation system. Images are usually provided as a continuous stream of data, and the sampling frequency

depends on the image size and on the capture device capabilities (larger images require more data to be exchanged with the host bus, i.e. the USB, Universal Serial Bus in modern computer architectures).

A fixed (and sometimes very long) slot of time is usually dedicated to the device initialization, as digital cameras mandate to activate analog sensors before start capturing data. Once the device is set up properly, it is be able to capture up to 15-20 frames per second, thus the control algorithm may be very fast, achieving a good level of fluency and granularity during the motion phase.

For the purpose of considered navigation system, the size of the image capture can be within small ranges of width and height (e.g., 320x240 pixels) and this guarantees sample images to be captured very frequently. Unfortunately, this is also power-consuming, and it is not feasible to keep grabbing and discarding data just not close the device, in order not to restart it later.

Loss of power can be attributed either to analog sensors and to the USB bus switching activity. Analog sensors are disabled whenever the digital camera is de-activated, while USB bus consumes power as long as data keeps on being exchanges (i.e., while the host bus sends capture requests to the external device). Trading-off power consumption and speed is one of the goal of our algorithm, that is tuned in such a way that images are grabbed only when required. The device is switched off during the motion phase, and it is restored when a new reference point is needed.

3.2 SOFTWARE INTEGRATION FROM THE FUNCTIONAL POINT OF VIEW

Software can be divided, from the functional point of view in three parts:

- behavioral algorithm;
- motor control;
- image acquisition.

3.2.1 Algorithm

Algorithm is a program written in C language that controls all the vehicle's activity. If it is necessary it calls external applications used for image acquisition and motor control. More about algorithm is possible to find in chapter 4.

3.2.2 Motor control

Motors are controlled by separate executable application (called *Angolo*), that in case of necessity can be called from movement algorithm with additional parameters. For example in DOS-like (Disk Operating System) Windows Command Shell the execution command to execute the program will be:

```
angolo.exe P0 P1 P2 P3 P4 P5 P6 P7 P8 Pt
```

The *angolo.exe* is the name of executable file stored in the PC. Parameter *P0* indicates which port needs to be opened. The parameters *P1-P8* indicate which rotational velocity that have to be applied at the channels 1-8. The parameters *P1-P8* have to be inserted in the form of the numbers. Value 125 is equal to the 0 velocity. Value 250 is equal to

the maximum velocity and the value 0 is equal to the maximum velocity, but in the opposite direction.

3.2.3 Image acquisition

Similar, as motors, also the camera is controlled by separate application (called *CameraGrabber*), that in case of necessity can be called from movement algorithm with additional parameters. Called with parameter $-g$ takes a picture and writes it on hard disk of the computer in the form of *.pgm* text file.

4 BEHAVIOURAL ALGORITHM

Behavioural Algorithm is the part of the main program, called *Navro*. It describes the control algorithm and calls functions and external programs if necessary.

The scope of this algorithm, stored and executed on the PC (Figure 1) is to make the vehicle follow the path constituted by waypoints specified by user (vehicle's operator).

Behavioural algorithm uses following algorithms:

- Position Calculation using Image Recognition Algorithm (PCIRA);
- Position Calculation by Summing Movements Algorithm (PCSMA);
- Position Update Algorithm (PUA);
- Go To the Waypoint Algorithm (GTWA);
- Passing π/π Heading Algorithm (PHA);
- Main Algorithm (MA).

4.1 POSITION CALCULATION USING IMAGE RECOGNITION

PCIRA works as the function of main program and is called, if necessary. As the result it is giving vehicle's position (camera is fixed to the rover and is pointing forward of the vehicle) in the Main Reference System (MRS) (Figure 11), and vehicles rotation (camera's pointing) respect to this system (Figure 12).

Three light landmarks are placed in the plane parallel to the ground, that is also the movement surface of the vehicle. Elevation of the plane, that contain bulbs, above the rover's movement surface is the same, as the elevation of onboard camera.

PCIRA reads acquired image stored in *.pgm* text file (Chapter 3.2.3) and load it, for elaboration, as the matrix. Then is searching for the columns in which exist pixels brighter than threshold (so called "bright pixels"). Algorithm performs its research until stopping conditions will occur. Stopping conditions are:

- after the column that contain bright pixel/pixels occur the column with no bright pixels;
- end of the matrix.

The assumption is that all the columns of the matrix that contain bright pixels, as a consequence of representation of the light source, are adjacent. When the stopping conditions will occur, algorithm calculates the number of bright pixels in the function of column number and calculates weighted

value, that is considered to be the column in which is placed the centre of seen light source.

Because of the necessity of localization of three lights, this procedure is being performed three times. Each time matrix is being elaborated from the beginning. Because of this fact, each localized bright pixel is being changed into "darker" (changing its value to smaller than threshold), not to be considered as bright pixel in the following loops.

Algorithm calculates the number of light sources found. If this number is smaller than 3, then proceeds as described in chapter 4.3.

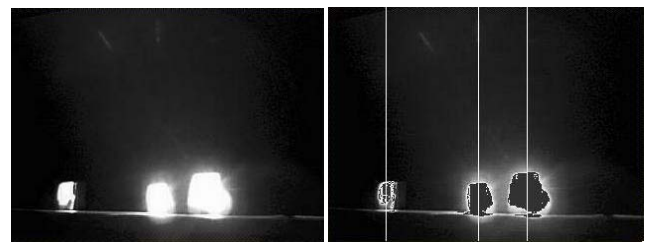


Figure 10 On the left: the image of SRL taken by onboard camera. On the right: the correctly recognized columns (signed by white lines) containing centres of the light sources.

To the reference lights is "attached" Main Reference System. This reference system is the system in which the rover navigates. MRS is centred on one of the lights, called Central Light (CL), as on the Figure 11.

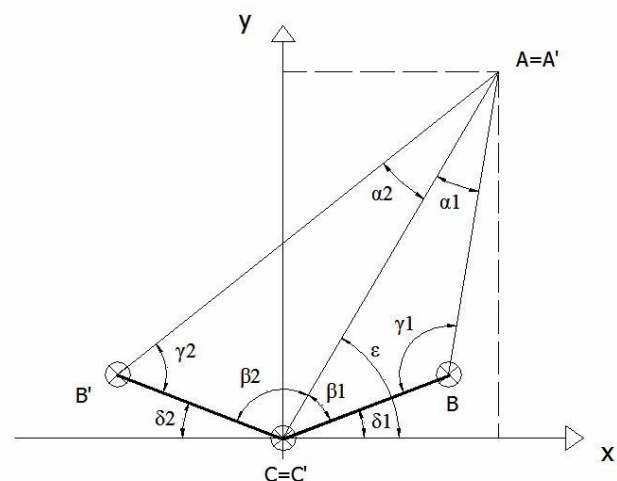


Figure 11 Main Reference System and System of Reference Lights (light sources: B, B', C=C'). C=C' is the Central Light. A=A' is the actual position of the camera.

The main idea is that depending on the position of the camera, changes the relative position of the light sources seen in the Field Of View (FOV) of the camera. α_1 and α_2 can be estimated by means of image recognition, than using the geometric relations can be find position of the camera.

By image recognition can be find also rotation ξ of the Vehicle Reference System VRS, that is fixed to onboard camera, respect MRS (Figure 12).

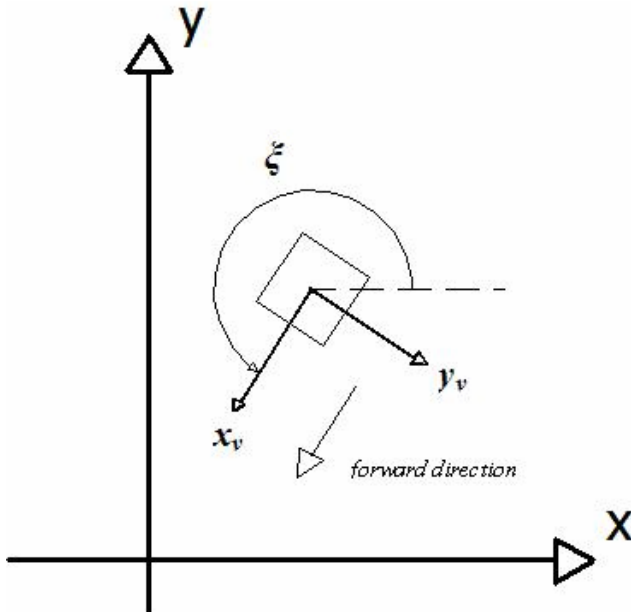


Figure 12 Rotation of the camera respect Main Reference System. Camera is pointing along the x_v axis of the VRS (Vehicle Reference System) centred on the camera.

In camera certain number of registered pixels corresponds with certain angle covered by FOV. In case of measure of horizontal angle between two objects, it is necessary to know, how many columns of pixels, between mentioned objects, represents this angle. This proportion has been find experimentally, and for used camera is equal to 0.146 deg/column. It has been also find that, for the tested webcam, variation of this proportion is negligible dependent from the section of FOV in which the measure has been taken.

In this way, knowing the column of pixel in which are placed two objects in the FOV it is possible to find the angular distance between them.

Knowing the position of the light sources of the SRL, it is possible to find angles α_1 , α_2 and the angle between CL and direction of x_v (camera's pointing), that after calculation of ε (Figure 11), allows to calculate ξ (Figure 12).

SRL geometry is known (δ_1 , δ_2 and distances CB and $C'B'$). Once knowing α_1 , α_2 , writing equations (using sinus theorem) for triangles ABC and $A'B'C'$ (Figure 11) and making observation that $AC=A'C'$ it is possible to calculate actual position (x, y) of the camera in MRS. Additionally in case under consideration: $\delta_1=\delta_2=\delta$.

Obtained system of equations:

$$\begin{cases} \arcsin\left[\frac{\sin \alpha_1}{\sin \alpha_2} \sin(\varepsilon + \delta - \alpha_2)\right] + \delta - \alpha_1 - \varepsilon = 0 & \text{for } \alpha_1 \leq \alpha_2 \\ \arcsin\left[\frac{\sin \alpha_2}{\sin \alpha_1} \sin[(\pi - \varepsilon) + \delta - \alpha_1]\right] + \delta - \alpha_2 - (\pi - \varepsilon) = 0 & \text{for } \alpha_1 > \alpha_2 \end{cases} \quad (1)$$

$$|AC| = \frac{|BC| \sin(\varepsilon - \delta_1 + \alpha_1)}{\sin \alpha_1}$$

$$x = |AC| \cos \varepsilon$$

$$y = |AC| \sin \varepsilon$$

can be solved numerically.

Of course position cannot be defined for $(\pi - \delta_2) < \varepsilon < \delta_1$.

PCIRA algorithm works only if it is called from Position Update Algorithm.

4.2 POSITION CALCULATION BY SUMMING MOVEMENTS

PCSMA calculates the rover's position, that not bases at image recognition. Instead the position is calculated each simulation step, by making the sum of single movements measured and introduced into the algorithm, before the experiment.

The position of the vehicle is described by 3 points (looking from behind the vehicle: point under centre of the left wheel (x_l, y_l) , point under the camera (x_s, y_s) , point under centre of the right wheel (x_p, y_p) ; coordinates expressed in MRS). Camera is assumed to be placed perfectly between wheels. Position of the vehicle can be also described as position of the central point, under the camera (x_s, y_s) and the orientation ξ . Orientation of the rover is equal to the camera's pointing. Camera is fixed firmly to the vehicle, so it can be assumed that position and orientation of the vehicle and camera are the same at each instant.

Position can be estimated in two ways. The first one is by image recognition. This one is considered as accurate measure. The second one is the estimation made by adding to the last determined position (by Position Update Algorithm), mathematically modelled movements, describing the change of vehicle's position each step of the execution of the programme (this is not valid for PCIRA). Mentioned changes of the vehicle's position are responses for a given command (single activation of *angolo* program). The value of the response for each command has been measured and inserted into the program.

Commands possible to give are: go forward, turn left, turn right. While giving single "go forward" command, both engines are being activated, what cause the progressive movement of the vehicle forward with a distance *go_forward* that should be measured before experiments and value inserted to the program. In case of giving single "turn left", or "turn right" command, only one engine is being activated, that cause the vehicle's rotation of the value ξ_{turn_left} , ξ_{turn_right} . Values ξ_{turn_left} , ξ_{turn_right} also should be measured end introduced to the program as constant.

For each motor actuation the new position of the vehicle is being calculated.

In case of going forward, the new position is:

$$\begin{cases} x_{l(n)} = x_{l(n-1)} + go_forward * \cos(\xi) \\ y_{l(n)} = y_{l(n-1)} + go_forward * \sin(\xi) \\ x_{s(n)} = x_{s(n-1)} + go_forward * \cos(\xi) \\ y_{s(n)} = y_{s(n-1)} + go_forward * \sin(\xi) \\ x_{p(n)} = x_{p(n-1)} + go_forward * \cos(\xi) \\ y_{p(n)} = y_{p(n-1)} + go_forward * \sin(\xi) \end{cases} \quad (2)$$

Where n is the number of the step.

In case of turns, two additional reference systems has been introduced. Local, centred on the left wheel, and local centred on the right wheel (Figures 13 and 14).

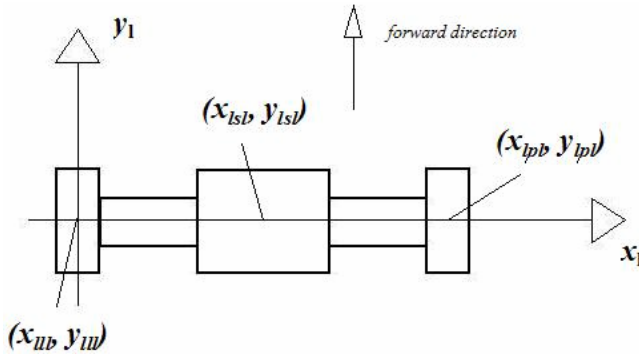


Figure 13 Local, centred on the left wheel, coordinate system. (x_{llr}, y_{llr}) , (x_{lsr}, y_{lsr}) , (x_{plr}, y_{plr}) are the coordinates of the points under the left wheel, camera and the right wheel.

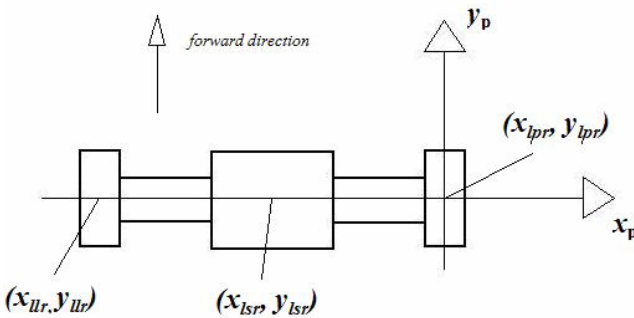


Figure 14 Local, centred on the right wheel, coordinate system. (x_{llr}, y_{llr}) , (x_{lsr}, y_{lsr}) , (x_{plr}, y_{plr}) are the coordinates of the points under the left wheel, camera and the right wheel.

Each time when turn command is given, the values ξ_{turn_left} , or ξ_{turn_right} are being added to ξ .

Rotational difference between Vehicle Reference System and Local Reference Systems is $-\pi/2$. Considering direction cosines matrix and taking in account that y_l , y_p coordinates of all points are always equal to 0, it is possible to write equations.

In case of turning left, the new position is:

$$\begin{cases} \xi_{(n)} = \xi_{(n-1)} + \xi_{turn_left} \\ x_{l(n)} = x_{l(n-1)} \\ y_{l(n)} = y_{l(n-1)} \\ x_{s(n)} = x_{l(n-1)} + x_{lsl} * \cos(\xi_{(n)} - \frac{\pi}{2}) \\ y_{s(n)} = y_{l(n-1)} + x_{lsl} * \sin(\xi_{(n)} - \frac{\pi}{2}) \\ x_{p(n)} = x_{l(n-1)} + x_{lpl} * \cos(\xi_{(n)} - \frac{\pi}{2}) \\ y_{p(n)} = y_{l(n-1)} + x_{lpl} * \sin(\xi_{(n)} - \frac{\pi}{2}) \end{cases} \quad (3)$$

In case of turning right, the new position is:

$$\begin{cases} \xi_{(n)} = \xi_{(n-1)} + \xi_{turn_right} \\ x_{l(n)} = x_{p(n-1)} + x_{llr} * \cos(\xi_{(n)} - \frac{\pi}{2}) \\ y_{l(n)} = y_{p(n-1)} + x_{llr} * \sin(\xi_{(n)} - \frac{\pi}{2}) \\ x_{s(n)} = x_{p(n-1)} + x_{lsr} * \cos(\xi_{(n)} - \frac{\pi}{2}) \\ y_{s(n)} = y_{p(n-1)} + x_{lsr} * \sin(\xi_{(n)} - \frac{\pi}{2}) \\ x_{p(n)} = x_{p(n-1)} \\ y_{p(n)} = y_{p(n-1)} \end{cases} \quad (4)$$

4.3 POSITION UPDATE

PUA is the procedure, that moves the vehicle in the way that all the three lights of the SRL are within FOV of on board camera in order to take a measure (effectuate PCIRA).

Each time the image is taken, the image recognition algorithm is calculating the number of the light sources founded. If the number of lights is smaller then 3, then algorithm actuate one of two motors that rotate entire vehicle with an angle ξ_{turn_left} , or ξ_{turn_right} . After each movement the photo is taken again. The process is repeated up to the moment, when all three light sources are within FOV.

In case of first time PUA execution (when for rover the position of SRL is unknown), rover rotates into right direction. In case of use of PUA successive times, the algorithm is estimating position of the SRL and is rotating in the proper direction in order to cover minimum angle between camera's actual pointing and direction towards SRL.

4.4 GO TO THE WAYPOINT

The scope of GTWPA is to bring the rover to the vicinity of the waypoint. At each loop it is calculating the new heading necessary to arrive to the waypoint. If the actual vehicle's heading is not very different, then desired heading (within the certain tolerances) both engines are being actuated. If the rover is not following required direction, left, or right motor are being actuated, in the way that rover follow to the waypoint.

Each actuation of the motors, new position is being calculated. Distance between the vehicle and each waypoint is expressed as the distance between the centre of the waypoint and the point under camera of the rover. The algorithm stops if the rover enters within certain range, from the waypoint, defined by user.

Each calculation step, the new position of the rover is being calculated by using PCSMA.

The small simulation of the work of the algorithm has been made.

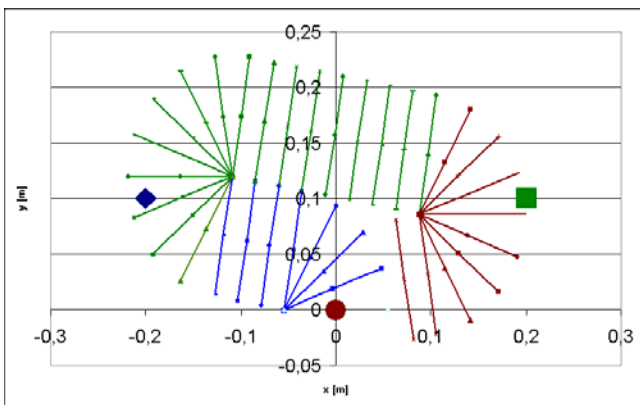


Figure 15 Simulation of the differential rover that uses Go To WayPoint Algorithm. WayPoint1 –blue, WayPoint2 – green, WayPoint3 – brown. Lines represents sequent vehicle's position: blue – when going to the blue waypoint, green – when going to the green waypoint, brown – when going to the brown waypoint.

Example (Figure 15):

Hypothetical autonomous vehicle moves between three waypoints expressed in MRS: WayPoint1 (-0,2; 0,1) m - blue, WayPoint2 (0,2; 0,1) m - green, WayPoint3 (0; 0) m - brown. Distance to accept the waypoint is 0,01 m. "Go forward" command makes the vehicle move 0,025 m. "Turn left/right" makes the rover change the movement's direction 20°. Rover starts its movement from the point (0; 0) m directed along the y axis. On the Figure 15 the sequence (each calculation step) of the autonomous vehicle positions are represented as lines. Vehicle turns left and approaches to the WayPoint1 for the distance smaller then 0,01 m (positions of the rover signed blue). Then turns right, go forward and goes toward WayPoint2 (positions of the rover signed green). After reaching acceptance zone of the second waypoint, turns right again and goes toward WayPoint3. When vehicle reaches the acceptance zone of the third waypoint, algorithm stops.

4.5 PASSING II/-II HEADING PROCEDURE

This algorithm takes part of GTWA. The vehicle's heading is described as a value between π and $-\pi$. Sometimes may happen that vehicle's actual heading and desired heading to the next waypoint are placed in the II-nd and III-rd quadrants of the MRS. In this situation to pass between both quadrants it is necessary to "pass" Ist and IVth quadrant, what would result in waste of time and energy and in some particular cases would not allow to arrive to the waypoint. To avoid this main algorithm starts PHA. This simple algorithm checks the actual heading and desired one and in case if they are in different quadrants, that are the IInd and the IIIrd quadrants, it actuates right, or left motor in order to pass directly between mentioned quadrants. Then 2π is added, or subtracted from actual heading ξ .

4.6 MAIN ALGORITHM

As it has been said before, the scope of this algorithm is to make the vehicle follow the path specified by user (vehicle's operator). The route can be defined by introducing into the program coordinates of the waypoints expressed in the Main Reference System.

After running of the program, rover placed randomly in MRS, but in different position then $(\pi-\delta_2) < \varepsilon < \delta_1$, starts its Position Update Algorithm to determinate actual position. Then calculates the heading to the first waypoint and actuating oportune motors starting its way toward it (GTWPA).

To increase precision, each waypoint is surrounded by two tolerance zones. The zone with the smaller radius (ZONE1), and with bigger radius (ZONE2) (Figure 16).

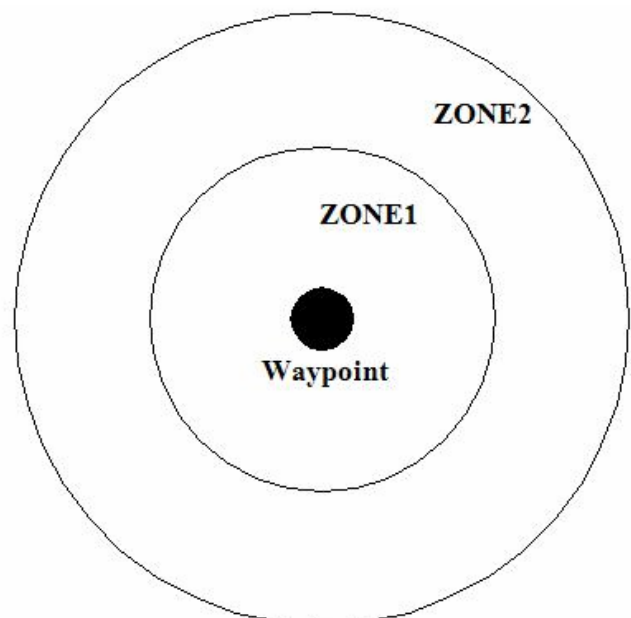


Figure 16 Each waypoint is surrounded by two tolerance zones. The zone with the smaller radius (ZONE1), and with bigger radius (ZONE2).

The Go To the WayPoint Algorithm continues its run up to the moment when the vehicle will arrive to the ZONE1. Then main algorithm starts PUA. If the image recognition recognize that the camera is within the ZONE2, the rover starts its way toward the next waypoint, or stops if there are no more waypoints. If PUA recognize that the rover is outside ZONE2, it starts its way again towards ZONE1 of the waypoint. The GTWPA conducts the vehicle to the "smaller" zone, this way introducing the vehicle quite in the centre of the "bigger" zone that is also the zone of acceptance of the waypoint by means of PUA.

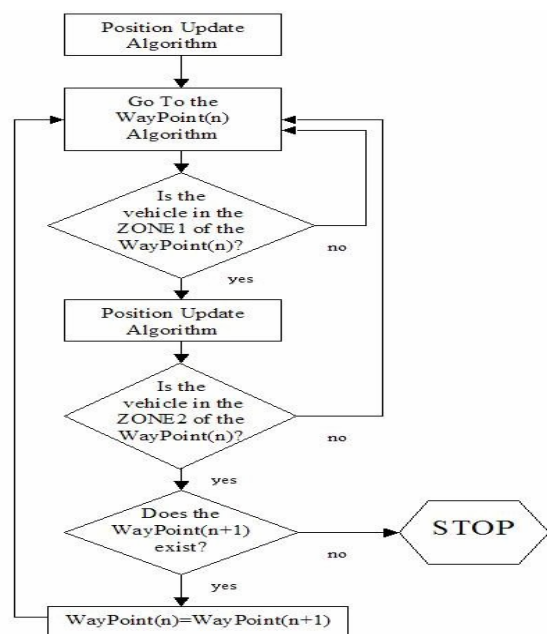


Figure 17 Main Algorithm, n – actual waypoint.

5 TEST RIG

To test the described solutions, the Test Rig has been created (Figure 18)



Figure 18 Test rig

The test rig has been created on the office floor. The physical architecture has been shown on Figure 1. On the floor (test area) has been placed SRL (Figure 8). Behind SRL is placed black background to minimise the possibility of misinterpretation of the image. For the same purpose, the general illumination of the test area and surroundings (office) has been kept low. On the same floor are placed white, paper circles, to indicate (for user) where the WayPoints are. On the same floor is operating the autonomous vehicle (Figure 3) described in chapter 2.3.

The program containing main algorithm registers in the file rover's position after each movement execution. The experiments are also filmed to have basic paragon of the real rover position and calculated position.

The dimensions of the System of Reference Lights are: $\delta_1 = \delta_2 = \delta = 30^\circ$ and $CB = C'B' = 0,104$ m.

6 TESTS

There have been many experiments of the system performed and many of them were successful. Because of the extensive experimental result documentation, only 3 experiments are presented, that show the correct work and might help to the reader understand, how the system work. Two of them shows the work of the system integrated under MS Windows XP and one under Linux.

6.1 EXPERIMENT 1

System integrated in MS Windows XP environment.

WayPoint1 is (0; 1,5)m - yellow

WayPoint2 is (0; 1)m - green

Radius of the ZONE2 (Radius of the tolerance to accept the waypoint): 0,15 m

Radius of the ZONE1: 0,03 m,

Vehicle placed randomly in the operation zone. After running the program, it is starting PUA and recognize its position in MRS. The recognized actual vehicle's position is (-0,575; 0,876) m (Figure 19) and is placed 0,848 m from the center of the first waypoint (Figure 20, point 1). This situation can be seen on the Figure 21 on the left.

Once determined its position, rover starts GTWP algorithm and starts its approach to the waypoint, what can be seen on the Figures 19 and 20 (points 1-33). After crossing the border of the ZONE1 (point (-0,012; 1,492) m in the Figure 19, point 33 on the Figure 20, middle picture on the Figure 21) Main Algorithm starts PUA again and finds, that real position of the vehicle is (-0,05; 1,385) m (Figure 19), point number 34 (Figure 20). Determined distance to the first waypoint is 0,126 m, so the rover is within the ZONE2 and the WayPoint1 can be accepted. Now vehicle refers its position to the WayPoint2 and starts its movement toward this point. The travel continues up to the moment when vehicle enters the ZONE2 of the second waypoint (point (0,005; 1,016) m (Figure 19) m, point 47 (Figure 20)) and starts its PUA, that finds that updated position is (-0,033; 1,114) m (Figure 19), point 48 (Figure

20), right picture on the Figure 21 and the distance to the WayPoint2 is 0,119 m, so the rover is within the ZONE2 and the WayPoint2 can be accepted. There is no more waypoints. Main Algorithm stops.

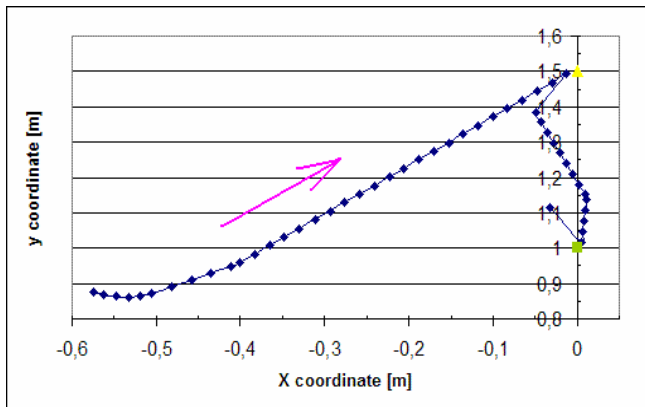


Figure 19 Route of the autonomous vehicle registered by Main Algorithm, expressed in MRS. The arrow indicates the direction of movement.

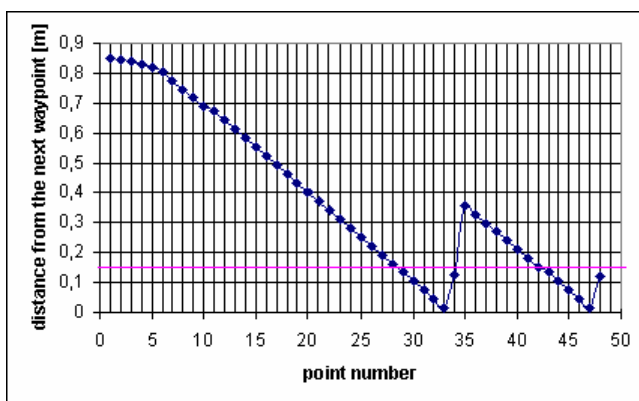


Figure 20 Distance between the autonomous vehicle and the next waypoint registered by Main Algorithm in the function of the program execution step number. The magenta line symbolize the range of 0,15 m (ZONE2 radius) from the next waypoint, necessary to accept waypoint.

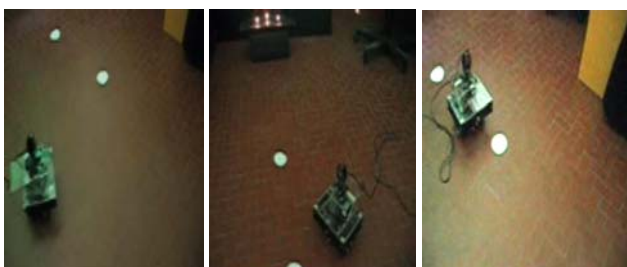


Figure 21 Three photos showing autonomous vehicle in the: first position update (left), before position update when arriving to the first waypoint (middle), after acceptance of the second waypoint (right).

5.2 EXPERIMENT 2

System integrated in MS Windows XP environment.

Waypoint1 is (0;1,5)m - yellow

Waypoint2 is (0;1)m - green

Radius of the ZONE2 (Radius of the tolerance to accept the WayPoint): 0,15 m

Radius of the ZONE1: 0,03 m,

Vehicle placed randomly in the operation zone. After running the program, it is starting PUA and recognize its position in MRS, that is (0,361481; 1,490751) m (Figure 22), point 1 (Figure 23), upper-left picture at Figure 24, and distance 0,362 m. Then it starts walking toward the first waypoint, each step calculating its new position. At the Figure 23 it is possible to see decreasing distance between rover and the center of the first waypoint (points 1-14). After crossing the border of the ZONE1 (point (0,021; 1,485) m in the Figure 22, point 14 on the Figure 23) Main Algorithm starts PUA again and finds, that actual position of the vehicle is (0,148; 1,37) m (Figure 22), point 15 (Figure 23), upper-middle picture on the Figure 24 and actual distance to the first waypoint is 0,197 m. It means that that the vehicles position is outside the acceptance zone of the waypoint. Main Algorithm starts again its GTWPA (points 15-27). The travel continues up to the moment when vehicle enters the ZONE2 of the first waypoint (point (-0,002; 1,487) m (Figure 22) m, point 27 (Figure 23)) and starts its PUA, that finds that updated position is (-0,11; 1,455) m (Figure 22), point 28 (Figure 23), upper-right picture on the Figure 24 and the distance to the WayPoint1 is 0,119 m, so the rover is within the ZONE2 of the first waypoint and the WayPoint1 can be accepted. Now vehicle refers its position to the WayPoint2 and starts its movement toward this point. The travel (points 29-43, Figure 23) continues up to the moment when vehicle enters the ZONE2 of the second waypoint (point (0,002; 1,006) m (Figure 22) m, point 43 (Figure 23)) and starts its PUA, that finds that updated position is (0,202; 1,015) m (Figure 22), point 44 (Figure 23), lower-left picture on the Figure 24 and the distance to the WayPoint1 is 0,202 m, what exceeds the range, required for waypoint acceptance, of 0,15 m. Rover again starts travel to the second waypoint (points 44-55, Figure 23). The travel continues up to the moment when vehicle enters the ZONE2 of the second waypoint (point (0,011; 0,991) m (Figure 22) m, point 55 (Figure 23)) and starts its PUA, that finds that updated position is (-0,051; 0,966) m (Figure 22), point 28 (Figure 23), lower-right picture on the Figure 24 and the distance to the WayPoint2 is 0,062 m, so the rover is within the ZONE2 of the second waypoint and the WayPoint2 can be accepted. There is no more waypoints. Main Algorithm stops.

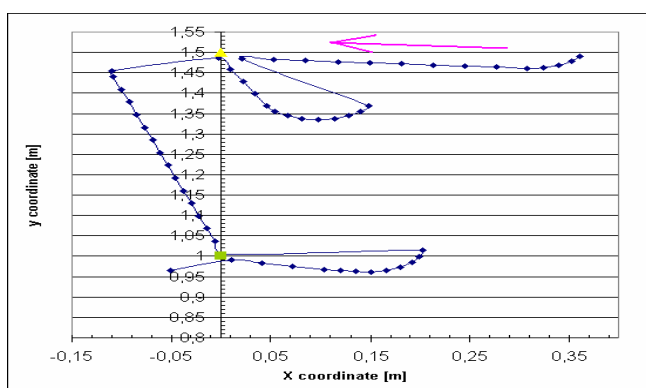


Figure 22 Route of the autonomous vehicle registered by Main Algorithm, expressed in MRS. The arrow indicates the direction of movement.

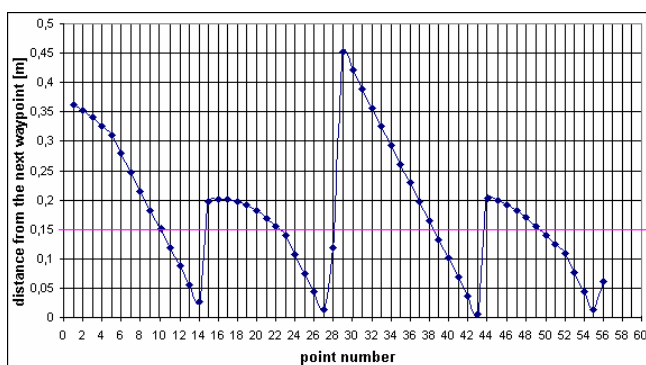


Figure 23 Distance between the autonomous vehicle and the next waypoint registered by Main Algorithm in the function of the program execution step number. The magenta line symbolize the range of 0,15 m (ZONE2 radius) from the next waypoint, necessary to accept waypoint.

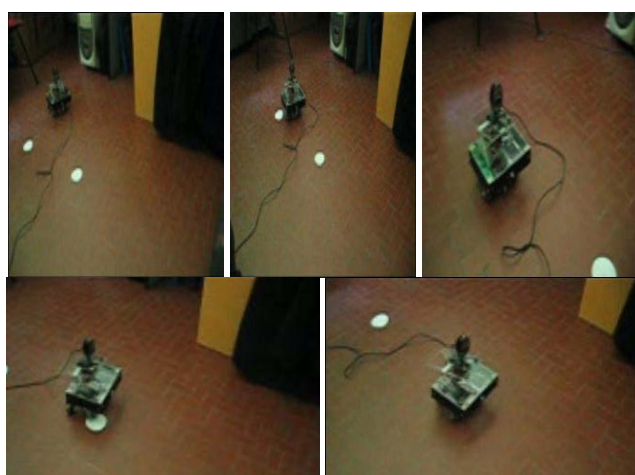


Figure 24 Five photos showing autonomous vehicle in the: first position update (upper-left), after position update when first time arriving to the first waypoint (upper-middle), after position update and acceptance of the first waypoint (upper-right), after position update when first time arriving to the second waypoint (lower-left), position update and acceptance of the second waypoint (lower-right).

5.3 EXPERIMENT 3

System integrated in Linux environment. Also in Linux environment has been performed many successful tests, but only one has been choose to be represented in this paper.

Waypoint1 is (0;1,5)m - yellow

Waypoint2 is (0;1)m - green

Radius of the ZONE2 (Radius of the tolerance to accept the WayPoint): 0,15 m

Radius of the ZONE1: 0,03 m

Vehicle placed randomly in the operation zone. After running the program, it is starting PUA and recognize its position in MRS. The recognized actual vehicle's position is (0,094046; 1,076494) m (Figure 25) and is placed 0,433823 m from the center of the first waypoint (Figure 26, point 1). This situation can be seen on the Figure 27 on the left.

Once determined its position, rover starts GTWP algorithm and starts its approach to the waypoint, what can be seen on the Figures 25 and 26 (points 1-30). After crossing the border of the ZONE1 (point (-0,010713; 1,480083) m in the Figure 25, point 30 on the Figure 26, middle picture on the Figure 27) Main Algorithm starts PUA again and finds, that real position of the vehicle is (0,000114; 1,411242) m (Figure 25), point number 31 (Figure 26). Determined distance to the first waypoint is 0,088758 m, so the rover is within the ZONE2 and the WayPoint1 can be accepted. Now vehicle refers its position to the WayPoint2 and starts its movement toward this point.

The travel continues up to the moment when vehicle enters the ZONE2 of the second waypoint (point (0,009074; 1,025846) m (Figure 25) m, point 47 (Figure 26)) and starts its PUA, that finds that updated position is (0,115973; 1,029368) m (Figure 25), point 48 (Figure 26), right picture on the Figure 27 and the distance to the WayPoint2 is 0,119634 m, so the rover is within the ZONE2 and the WayPoint2 can be accepted. There is no more waypoints. Main Algorithm stops.

Additional observations: In case of use of experiments performed with system integrated under Microsoft Windows XP the work of motor is irregular. For the same command the response slightly varies. There is no such problem in case of integration under Linux what influence positively the precision. Additionally in the second case the execution of the program is faster what makes shorter the pauses between the program execution steps and vehicle movements.

- [2] Chesa S., Corpino S., Viola N., Pluciński K. M., Stesina F., *Algoritmi per il controllo di flotte di piccole piattaforme aerospaziali e verifica sperimentale*. 18th AIDAA National Congress, Volterra, 2005
- [3] Murciano M., *Controllo Remoto Hardware e Software di Sistemi Aerospaziali a Basso Costo*, MSc thesis, Politecnico di Torino, 2005
- [4] www.wikipedia.org
- [5] Cabodi G., Quer S., Sonza Reorda M., *Introduzione alla programmazione in linguaggio C*.
- [6] Mikołajczak P., *Podstawy programowania w języku C/C++*, UMCS, Lublin, 2002

COMPARISON BETWEEN DAMAGE CRITERIA IN THERMO-MECHANICAL FATIGUE

Cristiana Delprete

Carlo Rosso

Raffaella Sesana

Department of Mechanics, Politecnico di Torino – Corso Duca degli Abruzzi 24, Torino, Italy

ABSTRACT

Weight reduction becomes increasingly important in design of engine components, but in the same time designers have to improve engine efficiency increasing in-cylinder pressure and temperature. The paper presents a description of literature damage models and life assessment methods for thermo-mechanical fatigue. The aim is to investigate the life prediction results in the case of a specific load history such as thermal and mechanical loading conditions upon an exhaust manifold. The literature methodologies are tested considering AISI 1070 steel for which calibration and experimental data are available from literature. Different literature damage models are analysed and applied to a finite element specimen undergoing thermal and mechanical loads. The computed life assessments are compared by means of a dedicated post-processor code. As result of methodology comparison it is underlined that Skelton and Chaboche models are the most appropriate models for life assessment when temperature load rates, magnitudes and mechanical load history allow creep to influence fatigue behaviour. The Manson-Coffin approach is the superior limit for durability when mechanical fatigue is more relevant and Sehitoglu model has great performance in any loading case even if it requires a great effort in defining material parameters.

Keywords: thermo-mechanical fatigue, life prediction, damage models

1 INTRODUCTION

According to standard (ASTM E2368-04e1) a thermo-mechanical fatigue (TMF) cycle takes place when uniform temperature and strain field over the specimen gage section vary in time simultaneously and independently. TMF occurs when components undergo time dependent thermal, stress and strain histories. In these conditions it is generally recognized that the prevalent damage mechanism in metals involves three major aspects: mechanical fatigue, oxidation and creep.

The fatigue damage is mainly due to cyclic plasticity-driven, time- and temperature- dependent phenomena that occur during cyclic loading [1]. Fatigue process in Low Cycle Fatigue (LCF) is quantitatively and qualitatively different than in High Cycle Fatigue (HCF) [2-4]. In LCF the nominal stress and plastic strain cyclically change much more than the micro-plastic changes of strain in HCF. The stabilized hysteresis loop permits the estimation of the

elastic and plastic strain amplitudes. The stress-strain curve can be obtained by means of the tips loci of the stabilized hysteresis loops under different total strain amplitudes [5]. With this curve the amplitude of elastic and plastic strains can be calculated and, independently on softening or hardening behaviour, by introducing the true stress and strain values in the constitutive law of the material, it is possible to obtain a realistic assessment of material behaviour.

The creep phenomenon is defined as irreversible, time-dependent, viscous material deformation at a constant tensile stress level [1, 6]. The creep behaviour is dependent on stress and temperature: as temperature or stress increases, the time to rupture decreases and vice versa [5, 7, 8]. As creep deformation helps the formation and propagation of micro-cracks, it leads to failure and it can modify the material mechanical properties, e.g. the elastic modulus. In TMF, creep and residual stresses occur in presence of tensile stresses and dwell time.

Oxidation is often defined as a worsening phenomenon above all when acting at crack tip [4, 9]. It is described as a long term effect introducing the oxidized layer sensitivity to cyclic loading. High temperature favours oxidation phenomenon. Physical models of oxidation are present in

Contact author: Cristiana Delprete
cristiana.delprete@polito.it

literature but the material calibration needs complex experimental tests.

The material damage mechanisms may interact or not, depending on material and operating conditions. Generally fatigue-creep-oxidation interactions are expected when operating temperature exceeds a third of the material melting temperature. TMF behaviour depends on material properties (for example thermal conductivity, thermal strain coefficient, elastic modulus, mechanical properties, ratchetting and cyclic hardening/softening behaviour [1]) and on operating conditions (for example maximum and minimum temperatures, temperature range, mechanical strain range, strain rate, phasing between temperature and mechanical load, stationing time, environmental factors). Phase transformations and ageing can influence the damage development but they are often described as second order phenomena [1].

In literature, approaches for TMF life assessment describing the damage development and interactions between the different damaging phenomena are numerous [1]. A reference framework for the prediction of TMF life has not been set because the involved phenomena and their interactions are numerous and complex and not completely understood. In [10] a detailed description and analysis of different approaches of the damage models is reported.

The first aim of the present paper is to compare, by means of numerical comparisons, five of the more diffused TMF life estimation methods. The second goal is to point out which of the different methods best simulates the effects of the different factors influencing the damage in the defined temperature and stress conditions.

2 TMF LIFE PREDICTION MODELS

A model of TMF life estimation is generally made of three parts: material constitutive law, damage equation and failure criterion.

The material constitutive law describes stress-strain material response. The most used models are elastic-plastic, visco-plastic [1, 11-13] and visco-elastic-plastic [7, 14], and their applicability is related to stress, strain and above all thermal conditions [7]. They consider the dissipative phenomena which take place in TMF life as creep, flow, damping, viscosity. Constitutive laws can be gathered in two groups [1]: the first group is composed of plasticity theory based laws, the second group is based on incremental plasticity theory like visco-plastic models. The damage equations return parameters which quantify the damage evolution in the structure, with respect to time, temperature, stress and many other parameters depending on material and loading conditions. The failure criteria express the limiting value for the damage parameter.

Considering the damage parameter definition, damage models can be divided in general or empirical (phenomenological).

General models [15] (general damage models, damage-rate models, TMF Strain-Strain Range Partitioning methods,

modified J-integral models) are mainly based on physical laws related to fracture mechanics. They describe in detail the damaging mechanisms (from a physical or phenomenological point of view) involved in material degradation as fatigue, creep, oxidation, ageing and their interactions. In general models, according to different loading conditions, a selection of damaging phenomena can be considered affecting TMF life. In [1, 15-22] for Sehitoglu and [23, 24] for Miller, creep, fatigue and oxidation interact for every stress value. In [9, 11, 12, 24-26] oxidation and fatigue are taken into account. In [11-13, 27-30] creep-fatigue interaction including an oxidation contribution are considered by Chaboche. In [7, 9, 31-34] an alternative approach to the linear [9, 36] or non-linear interaction between creep and fatigue is described. In general models, the damage parameter definition is related to different factors: cycle to failure (Sehitoglu, SRP, Chaboche), plastic strain amplitude (total plastic strain for Manson-Coffin [7], TS-SRP and SRP), strain range (Chaboche), crack width (Dai, Miller, Reuckert and Remy), crack propagation velocity (Baragetti [37], modified effective J-integral fracture mechanics models, all the damage rate models, BMW [35]). Some models (Manson-Coffin, TS-SRP) discriminate between LCF and HCF behaviour [7, 9, 12, 24, 26, 29, 34, 38]. General models also analyze the partitions of strain: plastic, elastic and thermal components (Manson-Coffin and TS-SRP methods); elastic, plastic and defined depending on the causes of strain (SRP method) [7]. The partition of strains is important to permit the proper definition of the damage parameters: plastic, elastic and thermal components due to creep and plastic (cyclic fatigue) deformations. In [1] it is noted that the effects of each damaging mechanism can be implicitly taken into account (oxidation damage accounted for in material parameters in TS-SRP or separately described in Sehitoglu method and stress-based methods as Chaboche). In these models the damage contributions can be linearly added (general linear accumulation models: Dai, Manson-Coffin, Sehitoglu) or non-linearly interacting (Chaboche, TS-SRP). The damage parameter can be expressed by means of an integral (Manson-Coffin) or incremental formulation (Dai, Sehitoglu, Chaboche, Miller, Reuckert and Remy). Fatigue damage is described by means of room temperature fatigue mechanisms and classical LCF equation [17, 18, 39]. Creep damage formulation considers the phase between thermal and mechanical load [18] and a phasing factor can be also defined for oxidation. Oxidation behaviour changes depending on thermal or mechanical strain. Generally speaking, both creep and oxidation are considered damaging only for tensile strains. Transition phenomena, which can be relevant in LCF, are often neglected and their description is attributed to constitutive laws (recovery, strain related phenomena; creep transition, ratchetting). To preserve from long solving times Chaboche, Reuckert and Remy and others [11, 25] suggest applying TMF damage criteria to a stabilized cycle thus obtaining a conservative life estimation.

Empirical models are based on the analysis of the hysteresis loop, like TS-SRP models [1], Charckaluk [14], Skelton [40-42] refer to the effects of the physical damaging phenomena: the damage equation is directly related to the hysteresis cycle parameters. For further details of TMF damage models and life estimation methods see [1, 9, 10, 14, 39, 41, 43]. In particular, in [37, 39, 40] a great attention is dedicated to the experimental characterization of model parameters, with both isothermal and temperature dependent tests. Finite element analysis (FEA) results associated with damage criteria allow a description of the design curve which is independent from temperature. Empirical models base the failure criterion on the hypothesis that material fails when the dissipated energy per volume unit (related to hysteresis cycle amplitude) exceeds a threshold (Skelton [40-42]); analogous hypothesis is formulated in [43].

3 TMF DAMAGE MODEL IMPLEMENTATION

As far as the numerical implementation and calibration are concerned, general models need a wide experimental basis and result in complex equations. Often these equations are not easy to use for engineering application but they are powerful and, once calibrated, they can be applied to different stress, strain and thermal loading conditions. Empirical models are less general, but more easily implemented for TMF life prediction.

Due to the complexity of the phenomena which take place in TMF, any mathematical description can be only incomplete. A phenomenological approach is probably more direct to describe the effects of physical damaging TMF phenomena as it contains the qualitative and quantitative aspects (dependence on temperature, stress level, strain rate, etc.) even if it does not investigate on the causes of the damaging phenomena. The limitation of a phenomenological approach is that the model needs to be calibrated in every loading condition; on the other hand the calibration is quite easy because for most of phenomenological methods it needs the acquisition of the hysteresis cycles in TMF or isothermal tests and static tests, see for example [40, 44].

The application of a TMF model includes the following steps:

- Calibrating the material parameters by means of isothermal and temperature dependent material tests;
- Defining a finite element (FE) model and implementing an appropriate material constitutive law;
- Applying the thermal and mechanical load histories, and computing the corresponding stress and strain states;
- Calculating the damage: simulation results (mechanical strain range, creep hold time, strain temperature phasing, stresses) are the input of the damage model;
- Estimating the residual life calculated by means of the relation between damage and number of cycles to failure.

By considering the constitutive law of the material and its influence on the computation of stress and strain distributions, two different FEA approaches are possible when a component undergoing TMF is analyzed.

The first approach consists in post-processing stress and strain data obtained from a non-linear thermal and mechanical FEA (for example [45, 46]). This computation should implement a constitutive model of the material describing strain and temperature rate effects (cyclic hardening or softening, creep, ratcheting, etc.). The material behaviour is therefore described in the constitutive model and its parameters are taken into account in a non-linear iterative computation of stresses and strains which are subsequently post-processed for the estimate of damage and life. The model definition is complex and FE computation results are time-intensive.

The second approach consists in post-processing stress and strain data obtained from a linear non-stationary temperature and load FEA. As an example, in [37, 47] material properties with non-linear rate dependent behaviour are taken into account in post-processing analysis which estimates the component damage and residual life on the base of specific material database and damage model. A Manson-Coffin damage model approach is used, but its parameters can change with temperature and strain rate, for every load and temperature history step. Miner cumulative damage law is applied.

In the following the first approach is chosen starting from a non-linear thermal and mechanical FEA with a rate independent material model.

4 MATERIALS AND METHODS

A dedicated code has been developed in MATLAB[®] by implementing the TMF damage models. This post-processor of FEA results allows qualitative and quantitative comparison of the life assessment curves obtained from different damage models: Manson-Coffin [45, 47], Neu-Sehitoglu [15-18], Chaboche [7, 12, 13], BMW [35], and Skelton [40-42]. In Figure 1 the first window of the code is shown.

For every damage model a numerical procedure has been implemented to calculate the damage time dependence in relation to stress, strain and temperature, and to obtain the material life curve in relation to plastic and total strain. The post-processor requires matrices containing strains and stresses obtained from FEA and a set of parameters depending on material and on experimental results and conditions that can be obtained from literature or tests. The Miner cumulative damage is assumed as failure criterion. In the following the damage models implemented in the post-processing routine are briefly described, together with their calibration procedure used in the present research work. To compare the results of different damage models, the computed life estimates are plotted versus the plastic component of strain (material life curve $N_F - \epsilon_p$).

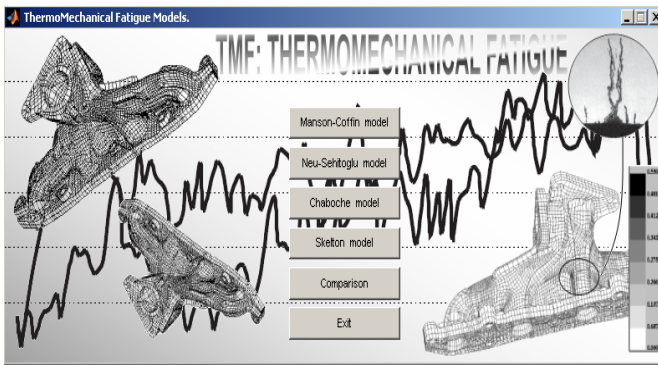


Figure 1 Thermomechanical Fatigue Post-Processor developed by the authors.

The damage models have been applied to stress and strain data obtained from a numerical simulation of a standard steel specimen FE model. Literature data [16, 17] related to AISI 1070 steel have been used to calibrate the damage models. Other information have been obtained from a test run on an actual component. All the plots comparing the obtained results in terms of cycles to failure have been set in arbitrary units. The TMF damage phenomenon has been analyzed by using local strain criteria (Manson-Coffin, Neu-Sehitoglu, Chaboche, and BMW models) and by using an energetic approach (Skelton model) based on the local dissipation of energy that is measured by means of the hysteresis cycles of the plasticized material.

4.1 MANSON-COFFIN MODEL

The classical and basic TMF damage model is the Manson-Coffin model that relates cycles to failure with total strain, i.e. the mechanical strain as composed by elastic and plastic components both related to cyclic life. This model considers mechanical fatigue as the only damaging phenomenon; it can be considered as the superior limit for durability. Life prediction can be described by the following equation:

$$\Delta\varepsilon_{tot} = \Delta\varepsilon_e + \Delta\varepsilon_p = \frac{\Delta\sigma}{E} + \Delta\varepsilon_p = \frac{G}{E} \cdot N_F^\gamma + M \cdot N_F^z, \quad (1)$$

where $\Delta\varepsilon_{tot}$, $\Delta\varepsilon_e$ and $\Delta\varepsilon_p$ are respectively the total, the elastic and the plastic strain, $\Delta\sigma$ is the stress amplitude, E the Young elastic modulus, N_F the cycles to failure, M the fatigue resistance coefficient, G the fatigue ductility coefficient, z the fatigue resistance exponent, and γ the fatigue plasticity exponent. The last four are material parameters.

The Manson-Coffin model can be applied to every kind of fatigue with the limitation of small strains at high temperatures or low temperature and when the strain phenomena are so rapid that the creep can be neglected. In other cases variation of M , z , G , γ , and E with temperature have to be taken into account [47].

A correct approach [5, 7] to calibrate the relation between cyclic strain and cycles to failure N_F of a test component is to refer to the cyclic σ - ε curve. The best region for obtaining M and z constants is in the LCF range, on the

contrary it is better to evaluate G and γ in the HCF region where elastic strain is mainly relevant. In [40] the parameter calibration is obtained from isothermal static tests. In the following, the calibration is referred only to M and z parameters because the reference LCF duration is the life expected for the component experimentally tested. The value of z is known from literature, plastic strain is obtained from FEA and N_F is obtained from experimental data. The value of M can be obtained knowing the cycles to failure of the bench test as $M = \Delta\varepsilon_p / N_F^z$.

4.2 NEU-SEHITOGLU MODEL

Evolutions of the Manson-Coffin model are the Sehitoglu [15] and the Neu-Sehitoglu [16-17] models which define high temperature fatigue damage by means of the fatigue, creep and oxidation terms. The Neu-Sehitoglu model defines the total damage as linear contribution of mechanical fatigue, creep and oxidation damages:

$$D_{tot} = D_{fat} + D_{creep} + D_{ox}. \quad (2)$$

Equation (2) refers to Miner formulation and the total damage can be defined as $D_{tot} = 1/N_F$. By assuming a linear damage formulation that becomes equal to 1 when failure occurs, every term of (2) can be formulated as a function of the cycles to failure N_F .

The fatigue damage D_{fat} is related to mechanical strains

$\Delta\varepsilon_{mech}$ and can be described from the classical equation (1) with a calibration procedure analogous to that of the Manson-Coffin model.

The creep damage can be computed as:

$$D_{creep} = \Phi_{creep} \int_0^{t_c} A e^{(-\Delta H/RT)} \left(\frac{\alpha_1 \bar{\sigma} + \alpha_2 \sigma_H}{K} \right)^m dt, \quad (3)$$

where t_c is the time to failure, $\bar{\sigma}$ the equivalent stress, σ_H the hydrostatic stress, K the maximum tensile stress acting on maximum stress axis, α_1 and α_2 the traction and compression damage factors, A and m the material constants, ΔH the activation energy for the rate controlling creep mechanism and Φ_{creep} the ε - T phase factor for the creep phenomenon.

The phase factor Φ_{creep} can be evaluated as a function of thermal and mechanical strain ratio as:

$$\Phi_{creep} = \exp \left[-\frac{1}{2} \left(\frac{\frac{\dot{\varepsilon}_{th}}{\dot{\varepsilon}_{mech}} - 1}{\xi_{creep}} \right)^2 \right], \quad (4)$$

where ξ_{creep} is the creep sensitivity of the phasing to the creep damage. The function Φ_{creep} is exponentially related to $\dot{\varepsilon}_{th}/\dot{\varepsilon}_{mech}$ and expresses the severeness of the creep phenomenon for every ratio of thermal and mechanical strain rate. The function is represented by a normal distribution with a maximum value equal to 1 when the

phase between the two mechanisms is much damaging, that is during in phase (IP) TMF.

In the present paper the parameters $\bar{\sigma}$, σ_H , $\dot{\varepsilon}_{th}$ and $\dot{\varepsilon}_{mech}$ result from FEA, α_1 and α_2 from literature, Φ_{creep} from loading conditions. The constant A and the exponent m are not known for the considered material. As m is a parameter for describing the hardening phenomenon, by assuming $A = 1$ a parametric study has been carried out varying m between 0.1 and 0.5 to estimate its effect on damage.

The oxidation damage mechanism includes the nucleation of the crack on the oxidized surface and the crack growth due to oxide induction. The temperature, the strain amplitude, range and the phase between temperature and strain have a critical role in the determination of oxidation crack's way to grow. All factors that affect the crack growth can be related to the critical thickness that is the threshold value the oxidized layer fails beyond. The oxidation damage can be integrated on a cycle and, for constant amplitude strain, it can be computed as:

$$D_{ox} = \left(\frac{h_{cr} \delta_0}{B \Phi_{ox} k_p^{eff}} \right)^{-\frac{1}{\beta}} \frac{2 \Delta \varepsilon_{mech} \left(\frac{1+\frac{2}{\beta}}{1-\frac{a}{\beta}} \right)}{\dot{\varepsilon}_{mech} \left(\frac{1-\frac{a}{\beta}}{1+\frac{2}{\beta}} \right)}, \quad (5)$$

where h_{cr} is the thickness of the oxidized layer, δ_0 the material ductility, B and β the material constants, a the strain rate sensitivity constant, k_p^{eff} the parabolic oxidation constant, $\dot{\varepsilon}_{mech}$ the mechanical strain velocity, $\Delta \varepsilon_{mech}$ the mechanical strain amplitude, and Φ_{ox} the ε - T phase factor for the oxidation phenomenon. The constant values can be experimentally determined and the phase factor Φ_{ox} can be computed with an equation similar to (4).

In the present paper it has not been possible to evaluate the parameters of equation (5), so the oxidation damage has not been taken into account.

4.3 CHABOCHE MODEL

The Chaboche fatigue damage evolution model is based on stresses and it assumes that the cumulated damage is non-linear, its main aspect is the definition of a reciprocal interaction between creep and mechanical fatigue. This model defines an incremental damage as the sum of mechanical fatigue and creep damage contributions, both depending on the instantaneous value of the total damage:

$$dD = dD_{fat} + dD_{creep}, \quad (6)$$

with

$$dD_{fat} = \left[1 - (1 - D)^{-b+1} \right]^\alpha \left[\frac{\sigma_{max} - \sigma_m}{A(1 - D)} \right]^{-b} dN \quad (7a)$$

and

$$dD_{creep} = \left(\frac{\sigma}{A} \right)^r (1 - D)^{-h} dt, \quad (7b)$$

where σ_{max} and σ_m are the maximum and medium stress, A , b and α material constants, \bar{A} , r and h parameters

related to temperature, σ the instantaneous value of the stress, and D the instantaneous values of cumulate damage. The model calibration is obtained by means of independent experimental creep and mechanical fatigue tests.

The incremental calculation of the interaction between creep and mechanical fatigue highlights many intermediate effects in variable amplitude TMF loading histories. On the other side, this can be a drawback as the implementation requires long calculation time. The Chaboche model can be applied to every TMF loading history; the main objection could be that a stress based model is not suitable in case of LCF.

In the present paper the values of σ_{max} and σ_m result from FEA, b from literature, α and A from experiments; also the creep parameters (\bar{A} , r and h) have been obtained from literature.

4.4 BMW MODEL

The BMW model starts from Chaboche works on TMF and it develops a numerical model able to calculate damage in complex time varying TMF load histories, basing on fracture mechanics analysis.

In particular the paper [35] considers a vehicle exhaust system, undergoing severe thermal cycles between room temperature and 880 °C. The proposed damage model is time and temperature dependent and it is based on constitutive equations related to elasto-plastic fracture mechanics, leading to a general non-linear equation which defines the failure location and the cycles to failure by means of a database (non available in [35]). A damage parameter is defined for temperature dependent arbitrary shaped cycles as a function of stress distribution and Von Mises equivalent stress:

$$D = \left(1.45 \frac{\Delta \sigma_I^2}{\sigma_{cy} E} + \frac{2.4}{\sqrt{1+3n}} \frac{\Delta \sigma_I^2}{\sigma_{cy} \Delta \sigma_{eq}} \varepsilon_p \right)^F, \quad (8)$$

where σ_{cy} is the 0.2% cyclic yield stress with respect to the point strain rate reversal, $\Delta \sigma_I$ twice the maximum principal strain, $\Delta \sigma_{eq}$ the Von Mises equivalent stress, ε_p twice the Von Mises equivalent plastic strain, F a parameter that considers creep and dwell time effects, and n the Ramberg-Osgood hardening parameter [49]. Subscript *eff* indicates that the effect of crack closure is taken into account.

The damage parameter is related to the number of cycle to failure as:

$$N_F = \tilde{A} D^{-\tilde{B}}, \quad (9)$$

where the coefficients \tilde{A} and \tilde{B} are related to the thermal and mechanical loads stressing the component.

4.5 SKELTON MODEL

The Skelton model uses an energetic approach derived from crack propagation theory. The energy locally dissipated, measured by means of the hysteresis cycle of the plasticized material, can be correlated to a damage parameter and to component life [43].

Hysteretic behaviour of cycles in isothermal fatigue differs from TMF because in the last case cycle plastic and elastic strain cannot be distinguished [43, 48] and stiffness changes with temperature. Moreover, in TMF, thermal deformation varies with time and it is in general more relevant and more damaging.

The thermal strain energy, described as the energy dissipated in the shape of heat and absorbed in the material, due to dislocation motion until crack nucleates, can be assumed as parameter of TMF damage. The damage criterion is related to deformation energy calculated from stress-strain hysteresis loops.

The energy density associated to an hysteresis cycle (σ - ε) can be partitioned in contributions related respectively to elastic, plastic and thermal strain:

$$\Delta U_{tot} = \Delta U_e + \Delta U_p + \Delta U_{th}. \quad (10)$$

Each strain energy density can be expressed as:

$$\Delta U_e = \oint \sigma d\varepsilon_e = \frac{\Delta \sigma^2}{2E}, \quad (11)$$

$$\Delta U_p = \oint \sigma d\varepsilon_p \quad \text{and}$$

$$\Delta U_{th} = \oint \sigma d\varepsilon_{th},$$

where $\Delta \sigma$ is the amplitude of the stress acting in the specimen or component.

It is also possible to calculate the energy density associated to the mechanical strain as the sum of elastic and plastic contributions:

$$\Delta U_{mech} = \oint \sigma d\varepsilon_{mech} = \oint \sigma d\varepsilon_e + \oint \sigma d\varepsilon_p. \quad (12)$$

The total strain energy density can be obtained by contributions of mechanical and thermal components:

$$\Delta U_{tot} = \Delta U_{mech} + \Delta U_{th}. \quad (13)$$

Thus defining the energy density associated to mechanical and thermal strains, it is possible to compute and compare the damage due to mechanical and thermal cycles respectively. It is more conservative and easier to calculate these quantities by means of the stabilized hysteresis cycle (whenever it stabilizes).

5 THE FE SPECIMEN MODEL

A flat standard specimen for mono-axial fatigue test has been modelled with FE. The mesh has been obtained by means of 5852 eight-nodes brick elements (Figure 1).



Figure 1 FE model (5852 eight-nodes brick elements).

The material constitutive model is visco-plastic with rate dependent properties. The thermal and mechanical time histories are shown in Figure 2 and 3; they are typical of automotive exhaust manifolds.

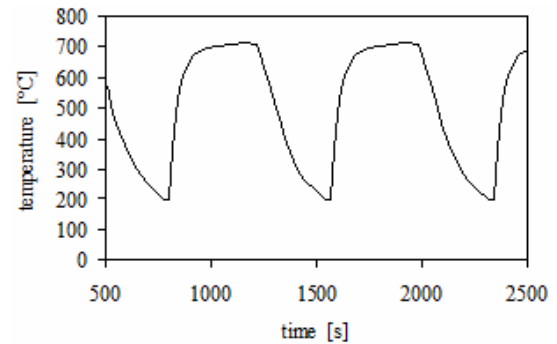


Figure 2 Thermal cycle applied to the FE specimen.

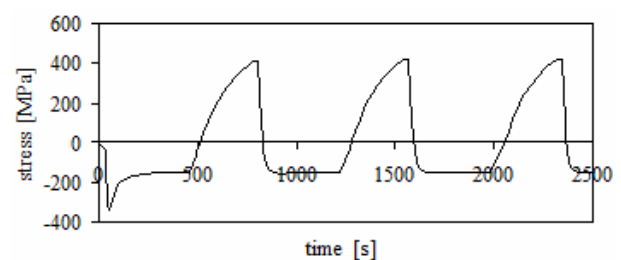


Figure 3 Axial stress applied to the FE specimen.

The pre-processor, solver and post-processor used for FE analysis is ABAQUS[®] 6.6. Running a thermo-structural FEA, the thermal strains versus time vary between 0.002 and 0.0096, as shown in Figures 3 and 4. A linear behaviour with respect to temperature is highlighted in the range between minimum and maximum temperature as the constitutive model forces.

Elastic strains are related to load and to elastic modulus which has been defined variable with temperature. The computed elastic strains are ten times lower than thermal strains. Plastic strains, which are relevant in LCF, after an initial transition, settle on a constant value. Plastic strain is equal to 0.0089. The obtained stress and strain values (Figure 4) are the input values for the above mentioned post-processing MATLAB[®] routines authors developed for estimating the TMF life of the specimen.

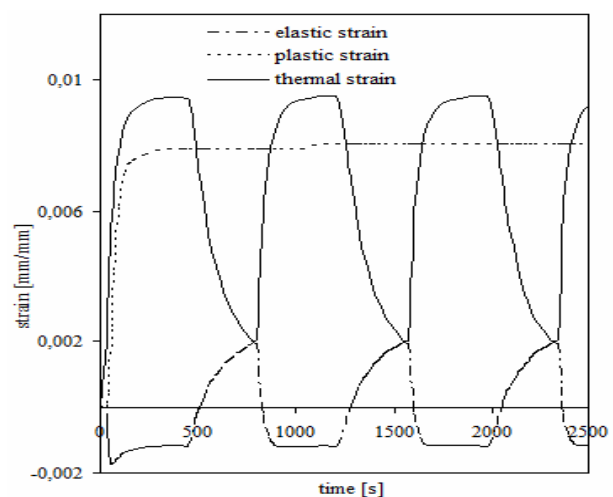


Figure 4 Longitudinal elastic, plastic and thermal strains.

6 RESULTS AND DISCUSSION

First of all it should be observed that the results of the post-processor analysis are strongly affected by the constitutive model chosen for the material. This is because the values of the element stresses, and above all of the plastic, thermal and elastic strains, change with the applied constitutive model. In [50] an analysis of this influence on stress and strain distribution is described. The influence is relevant as the input data of damage models are generally stress and strain distributions.

Skelton damage model considers an energetic approach, and then its life estimation strongly depends on the constitutive model as the hysteresis cycle depends on the constitutive model formulation. To implement the damage model in the post-processor it is thus necessary to make the following hypotheses:

- The mechanical and thermal loading histories, as well as the hysteresis cycle, must be periodic. Otherwise, it is necessary to calculate the damage for every step of the loading history or for every hysteresis cycle and then cumulate the damage;
- The constitutive material model adequately describes the material cyclic behaviour;
- When the hysteresis cycle stabilizes, it is important to evaluate if it is possible to neglect the cycles before the stabilization.

The analysis shows that the hysteresis energy stabilizes at the third cycle. The contribution to damage related to the first two cycles has been neglected if the energy difference of the first two cycles is lower than 10% with respect to the stabilized value.

As far as Chaboche damage model is concerned, it appears that the most part of the component life is spent in the initial cycles. By analyzing the results it can be seen that creep is the most influent damage cause in component life assessment. This is because while the mechanical damage term only depends on the number of cycle, the creep damage term is related to time and, in the case of a component, it is evident that the dwell time involved in the test allows the creep damage to reach relevant values.

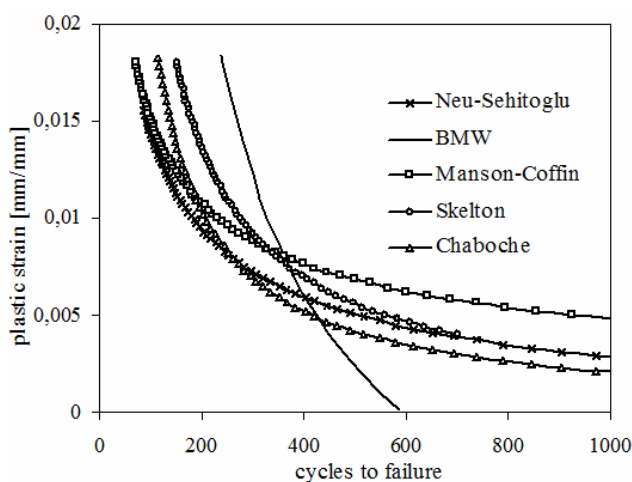


Figure 5 Life prevision results.

In Figure 5 the life assessments that are obtained using the above-mentioned procedures are shown considering an actual component, an exhaust manifold. All the damage models implemented in the post-processor are included in the diagram. but the numerical data are hidden because of confidentiality requirements.

7 CONCLUSIONS

A commercial AISI 1070 steel specimen has been numerically simulated. Numerical analysis of thermal and mechanical loads with appropriate boundary conditions has been conducted. The chosen thermal and mechanical loading conditions correspond to the loading conditions of actual components.

A post-processor has been developed with the aim of comparing different damage models and TMF life estimation methods from different points of view: implementation routines, calibration difficulties, strictness of damage estimation and applicability in the exhaust manifold load case.

It results that the energetic approach (Skelton model) and the Chaboche model are more appropriate for component life assessment for which the temperature load rates and the mechanical load history allow creep to influence fatigue life. The calibration of Chaboche model is still complex and, if data are not available in literature, it needs a wide experimental effort. This effort can be justified considering that the obtained database allows the application of the model to be extended to different thermal and load cases because it is an incremental approach.

On the contrary energetic models need experimental tests restricted to the thermal and mechanical load history that has to be analyzed. The results thus obtained are also limited to the considered thermal and mechanical load case.

REFERENCES

- [1] Ogarevic V., Wittle B., Lin X., and Anderson R., 2001, "Thermal fatigue of automotive components", *SAE Technical Paper 2001-01-0829*.
- [2] Jaske C. E., Thermal mechanical, low cycle fatigue of AISI 1010 steel, *Thermal Fatigue of Materials and Components*, ASTM STP 612, pp. 170-198, 1976.
- [3] Kraft S. A., and Mughrabi H., Thermo-mechanical fatigue of the monocrystalline Nickel-base superalloy CMSX-6, *Thermo-Mechanical Fatigue Behaviour of Materials*, ASTM STP 1263, pp. 27-40, 1996.
- [4] Remy L., Bernard H, Malpertu J. L., and Rezai-Aria F., Fatigue life prediction under thermo-mechanical loading in a Nickel-base superalloy, *Thermo-Mechanical Fatigue Behaviour of Materials*, ASTM STP 1186, pp. 3-16, 1993.
- [5] Lazan B. J., *Damping of materials and members in structural mechanics*, Pergamon Press, UK, 1968.

- [6] Sasaki K., Takashashi T., Nagayoshi T., and Kumano M., Thermal plastic-elastic creep analysis of engine cylinder head, *SAE Technical Paper 2002-01-0585*.
- [7] Lemaitre J., and Chaboche J. L., *Mécanique des matériaux solides*, Editions Dunod, F, 1988.
- [8] Webster G. A., and Ainsworth R. A., *High temperature component life assessment*, Chapman & Hall, USA, 1994.
- [9] Cai, C., Liaw, P. L., Ye, M., and Yu, J., Recent developments in the thermo-mechanical fatigue life prediction of superalloys, *JOM*, Vol. 51, No. 4, 1999.
- [10] Delprete C., Rosso C., and Sesana R., Damage criteria in thermo-mechanical fatigue models, *Proc. 8th Biennial ASME ESDA*, Torino, I, ESDA2006-95470, 2006.
- [11] Chaboche J. L., Policella H., and Kaczmarek H., Applicability of the SRP method and creep-fatigue damage approach to the LCHTF life prediction of IN-100 alloy, *ONERA TP 1978-13*, 1978.
- [12] Chaboche J. L., Policella H., and Savalle S., Application of the continuous damage approach to the prediction of high temperature low cycle fatigue, *ONERA TP 1978-70*, 1978.
- [13] Lemaitre J., and Chaboche J. L., A non linear model of creep-fatigue damage cumulation and interaction, *ONERA TP 1394*, 1974.
- [14] Charkaluk E., Bignonnet A., Constantinescu A., and Dang Van K., Fatigue design of structures under thermo-mechanical loadings, *Fatigue Fract. Eng. Mat. Struct.*, Vol. 25, pp. 1199-1206, 2002.
- [15] Sehitoglu H., Thermo-mechanical fatigue life prediction methods, *Advances in Fatigue Lifetime Predictive Techniques*, ASTM STP 1122, pp. 47-76, 1992.
- [16] Neu R., and Sehitoglu H., Thermo-mechanical fatigue, oxidation & creep: Part 1 - Experiments, *Metallurgical and Materials Transactions A*, Vol. 20A, pp. 1755-1767, 1989.
- [17] Neu R., and Sehitoglu H., Thermo-mechanical fatigue, oxidation and creep: Part 2 - Life Prediction, *Metallurgical and Materials Transactions A*, Vol. 20A, pp. 1769-1783, 1989.
- [18] Sehitoglu H., and Boismier D. A., Thermo-mechanical fatigue of Mar-M247: Part 2 - Life Prediction, *J. Eng. Mat. and Tech.*, Vol. 112, pp. 80-89, 1990.
- [19] Slavik D., and Sehitoglu H., A constitutive model for high temperature loading. Part I - Experimentally based forms of the equations, *Proc. ASME Conf. Thermal Stress, Material Deformation and Thermomechanical Fatigue*, New York, NY, Vol. 123, pp 65-73, 1987.
- [20] Slavik D., and Sehitoglu H., A constitutive model for high temperature loading . Part II - Comparisons of simulations with experiments, *ASME Conf. Thermal Stress, Material Deformation and Thermomechanical Fatigue*, New York, NY, Vol. 123, pp 75-82, 1987.
- [21] Karasek M. L., Materials engineering-mechanical behaviour", *College of Engineering - University of Illinois at Urbana*, USA, Report 132, 1986.
- [22] Song G., Exhaust system key life test, *SAE Technical Paper 2001-01-1105*.
- [23] Miller M. P., McDowell D. L., Oehmke R. L. T., and Antolovich S. D., A life prediction model for thermo-mechanical fatigue based on microcrack propagation, *Thermo-Mechanical Fatigue Behaviour of Materials*, ASTM STP 1186, pp. 35-49, 1993.
- [24] Dai J., Marchand N. J., and Hongoh H., Thermal mechanical fatigue crack growth in titanium alloy: experiments and modelling, *Thermo-Mechanical Fatigue Behaviour of Materials*, ASTM STP 1263, pp. 187-209, 1996.
- [25] Reuchet J., and Remy L., Fatigue oxidation interaction in a superalloy-application to life prediction in high temperature low cycle fatigue, *Metallurgical and Materials Transactions A*, Vol. 14 A, pp. 141-149, 1983.
- [26] Chataigner E., and Remy L., Thermo-mechanical fatigue behaviour of coated and bare nickel-based superalloy single crystals, *Thermo-Mechanical Fatigue Behaviour of Materials*, ASTM STP 1263, pp. 3-25, 1996.
- [27] Kachanov L. M., Time on the rupture process under creep conditions, *Izv. Akad. Nauk. SSR Otd Tech. Nauk.*, Vol. 8, pp. 26-31, 1958.
- [28] Rabotnov Y. N., *Creep problems in structural members*, North Holland, NL, 1969.
- [29] Halford G. R., and Saltsman J. F., Strain range partitioning - A total strain range version, *ASME Int. Conf. on Advances in Life prediction Methods*, pp. 17-28, 1983.
- [30] Saltsman J. F., and Halford G. R., An update on the total strain version of SRP, *Symposium on Low Cyclic Fatigue - Directions for the Future*, ASTM STP 942, pp. 329-341, 1987.
- [31] Saltsman J. F., and Halford G. R., Life prediction of thermo mechanical fatigue using total strain version of strain range partitioning (SRP), *NASA Technical Paper 2779*, 1988.
- [32] Halford G. R., Radhakrishnan V. M., and Kalluri S., Thermo-mechanical and bithermal fatigue behaviour of bast B1900+Hf and wrought Haynes 188, *Advances in Fatigue Lifetime Predictive Techniques*, ASTM STP 1122, pp. 120-142, 1992.
- [33] Kalluri S., and Halford G. R., Damage mechanisms in bithermal and thermo-mechanical fatigue of Haynes 188, *Thermo-Mechanical Fatigue Behaviour of Materials*, ASTM STP 1186, pp. 126-143, 1993.
- [34] Manson S. S., Halford G. R., and Hirschberg M. H., Creep-fatigue analysis by strain-range partitioning,

- Design for High Temperature Environments*, ASME, pp. 12-28, 1971.
- [35] Schmitt W., Mohrmann R., Riedel H., Dietsche A., and Fischersworing-Bunk A., Modelling of the fatigue life of automobile exhaust components, *Proc. of the Eighth International Fatigue Congress*, Stockholm, SW, 2002.
- [36] Nissley D. M., Thermo-mechanical fatigue life prediction in gas turbine superalloys: a fracture mechanics approach, *AIAA Journal*, Vol. 33, No. 6, pp. 1114-1120, 1995.
- [37] Baragetti S., La Vecchia G. M., Terranova A., Variables affecting the fatigue resistance of PVD-coated components, *International Journal of Fatigue*, Vol. 27, pp. 1541-1550, 2005.
- [38] Halford G. R., and Manson S. S., Life prediction of thermal mechanical fatigue using strain range partitioning, *Thermal Fatigue of Materials and Components*, ASTM STP 612, pp. 239-254, 1976.
- [39] Lederer G., Charkaluk E., Verger L., and Constantinescu A., Numerical lifetime assessment of engine parts submitted to thermo-mechanical fatigue. Application to exhaust manifold design, *SAE Technical Paper 2000-01-0789*.
- [40] Skelton R. P., Webster G. A., De Mestral B., and Wang C. Y., Modelling thermo-mechanical fatigue hysteresis loops from isothermal cyclic data, *Thermo-Mechanical Behaviour of Materials*, ASTM STP 1371, 2000.
- [41] Skelton R. P., Energy criteria for high temperature low cycle fatigue, *Material Science Technology*, Vol. 7, pp. 427-439, 1991.
- [42] Skelton R. P., Cyclic hardening, softening and crack growth during high temperature fatigue, *Material Science Technology*, Vol. 9, pp. 1001-1008, 1993.
- [43] Takahashi T., Koike A., and Sasaki K., Inelastic behavior and low cycle fatigue of aluminum alloy subjected to thermo-mechanical loading, *SAE Technical Paper 980688*, 1998.
- [44] Falcao C. A., and Spinelli D., Thermo-mechanical fatigue: testing methods and application, *SAE Technical Paper 2001-01-4068*, 2001.
- [45] Watanabe Y., Shiratan K., Iwanaga S., and Nishino K., Thermal fatigue life prediction for stainless steel exhaust manifold, *SAE Technical Paper 980841*.
- [46] Delprete C., and Rosso C., Exhaust manifold thermo-structural simulation methodology, *SAE Technical Paper 2005-01-1076*.
- [47] Fe-Safe User Manual, 2003.
- [48] De Carolis G., Thermo mechanical fatigue models in components (in italian), *Dipartimento di Meccanica - Politecnico di Torino*, I, Master Degree Thesis, 2005.
- [49] Bezkorovainy P., Burns T., and Rasmussen K. jr., Strength curves for metal plates in compression, *Department of Civil Engineering, University of Sydney*, AUT, Research Report R821, 2002.
- [50] Zubeck M., Su X., and Allison J., Classical plasticity hardening for finite element analysis of cast aluminium powertrain components, *SAE Technical Paper 2002-01-0392*.

EFFECTS OF NONLINEARITIES AND CONTROL LAW SELECTION ON ACTIVE FLUTTER SUPPRESSION

Lorenzo Borello, Giuseppe Villero, Matteo Dalla Vedova

Department of Aerospace Engineering, Polytechnic of Turin, Turin, Italy

ABSTRACT

Conventional active flutter and vibration control technology relies on the use of aerodynamic control surfaces operated by servo-hydraulic actuators. Currently, most aeroelastic analyses are routinely conducted using a linear approximation of the equations of the flowfield and the structure. However, aerospace systems inherently contain structural, flight controls and aerodynamic nonlinearities. The objective of this paper is to analyze the aeroservoelastic behavior of a typical wing with active flutter suppression performed by a hydraulic servomechanism equipped with an adequate control law. In particular the purpose is to point out the effects of the flutter suppression control law selection, taking into account the nonlinearities of the servo-actuator dynamics. Active control has been implemented within the model of a representative actuation system, in order to investigate active means of flutter suppression via control surface motion, employing a simple control law relating the required surface deflection angle to speeds and acceleration of the main aerofoil surface.

Keywords: flutter, flight controls, active suppression

1 INTRODUCTION

Aeroelasticity is the mutual interaction between deformations of the elastic structure and aerodynamic forces induced by the structure deformations. Combined, these effects may cause an aircraft structure to become unstable above a defined value of flight speed. If the interaction between deformations and aerodynamic forces involves also the inertia, the phenomenon, called flutter, is an oscillatory instability that occurs when the structural damping transitions from positive to negative due to the presence of aerodynamic forces. During this transition, two modes of vibration coalesce to the same frequency and achieve an aeroelastic resonance. Bending and torsion are the two most common vibration modes of a wing which coalesce to flutter. In modern aircrafts the use of automatic flight control systems with powered control surfaces has further complicated the problem. This interaction between structural dynamics, unsteady aerodynamics and the flight control system of the aircraft, known as aeroservoelasticity, has been and continues to be an extremely important consideration in many aircraft designs.

To prevent undesirable aeroelastic effects, the stiffness of the wing must be increased, adding weight to the aircraft and decreasing the overall performance: this approach is known as “passive control”. A recent alternative to passive control is the so called “active control” through feedback to control surfaces (conventional technique), or, more recently, through feedback to active materials. These vibration control technologies allow flight vehicles to operate beyond the traditional flutter boundaries, improve ride qualities, and minimize vibration fatigue damage.

Many control strategies have been applied to suppress flutter or to control unacceptable wing motion.

Conventional active flutter and vibration control technology relies on the use of aerodynamic control surfaces operated by servo-hydraulic actuators. In this conventional configuration the flutter and vibration suppression algorithms are implemented through the servovalve/hydraulic actuator, capable of producing (if necessary in presence of large oscillation amplitude) large forces and large strokes. Though widely used, conventional technologies for active control of flutter and vibrations have severe limitations, such as: multiple energy conversions (mechanical, hydraulic, electrical), large number of parts (i.e. potential failure sites), high vulnerability of the hydraulic pipes network, limited actuation speed in saturation conditions and limited frequency range.

Contact author:

lorenzo.borello@polito.it

giuseppe.villero@polito.it

matteo.dallavedova@polito.it

Corso Duca degli Abruzzi, 24 – 10129 Torino, Italy

In contrast, active materials technologies offer direct conversion of electrical energy to high-frequency linear motion (extended bandwidth), but their typical shortcomings are limited forces and strokes performed. Generally, these problems have been already studied by several authors.

Lyons et al. [1] investigate full-state feedback with a Kalman estimator for the purpose of flutter suppression. Their theoretical model was relatively simple and required only eight states. Mukhopadhyay et al. [2] and Gangsaas et al. [3] used high-order models and developed methods for reducing these higher-order systems to show the practicality of such controllers. These control systems implemented estimators to describe unmeasured states and used output feedback as the control method.

Karpel [4] compared the aerodynamic descriptions of Lyons et al. [1] to develop partial-state feedback controllers. He used pole placement techniques to develop the control laws for flutter suppression and gust alleviation.

Horikawa and Dowell [5] performed flutter analysis with control, employing proportional gain feedback methods developed from root locus plots. They used a steady aerodynamic, two degree-of freedom structural model to develop several types of feedback. The approach directly feeds one of four variables to the control surface through a proportional gain.

These researchers have shown that linear theory is applicable for elaborate control systems in many cases. Unfortunately, as flight control systems and the associated performance of current military and civilian aircraft become increasingly complicated, the needs for more sophisticated aeroservoelastic models also increase. Most systems contain nonlinearities that are either neglected by the designer or linearized within the equations of motion. Recently, researchers have studied in detail the nonlinearities inherent in aeroelastic systems.

Currently, most aeroelastic analyses are routinely conducted using a linear approximation of the equations of the flowfield and the structure. However, aerospace systems inherently contain structural and aerodynamic nonlinearities: therefore a significant increase in advancing methods to consider nonlinear aeroelasticity has taken place. When the above mentioned nonlinearities are present, an aeroelastic system may exhibit different types of response, including limit cycle oscillation and even chaotic vibrations. These nonlinearities result from unsteady aerodynamic sources (transonic flow conditions, high angles of attack, large deflections) and from structural and control behavior. In particular, the most common nonlinearities in structures and flight control systems are listed below.

Structural nonlinearities:

- nonlinear stiffness, observed in the large bending and torsion of wings and rotor blades, that become increasingly harder (hardening stiffness) or softer (softening stiffness) to strain as they are moved further from the neutral position; this behavior is well described by a cubic stress-strain relationship, i.e. respectively cubic-hardening and cubic-softening nonlinearity. For general wing motion, the flutter velocity varies as the initial disturbance grows and the

stability of the system is highly dependent on the magnitude of the initial condition. A cubic-softening stiffness in the torsional degree of freedom lowers the flutter velocity; the cubic-hardening causes stable limit cycle oscillations, rather than divergent flutter, at velocities above the open loop flutter velocity;

- friction affecting rivets slipping on a wing, causing hysteresis concerning the stress-strain relationship;

Flight control nonlinearities:

- saturation, that occurs when an increasing input will no longer increase the output of the system. This nonlinearity occurs both in electrical and in hydraulic motors and related controllers, when their operational limits are exceeded;
- free play, often seen in position transducers and in control surface mechanical subsystem, when a surface will not move until the magnitude of the input exceeds a certain value;
- dry friction in motor and mechanical subsystem, resulting in a cyclic path (hysteresis) or in a response affected by stick slip phenomena and position inaccuracy;
- hysteresis present in the motor controllers, resulting in a cyclic path or in excessively reduced stability margin;
- dead zone nonlinearity in the motor controllers, resulting in the inability to move the control system within a defined position error field.

Woolston et al. [6] investigated nonlinearities in structural stiffness and control surface linkages. They created several models with free-play, hysteresis, cubic-hardening and cubic-softening nonlinearities in the torsional mode. For general wing motion, they observed that the flutter velocity decreased as the initial disturbance increased, and that the stability of the system was highly dependent on the magnitude of the initial condition. A cubic-softening spring stiffness lowered the flutter velocity. They also noted that cubic hardening caused limit cycle oscillations rather than flutter at velocities above the open-loop flutter velocity.

Breitbach [7] showed that a poor agreement between theory and experiment in flutter is most likely due to the presence of nonlinear structural stiffness. He also presented a detailed examination of many types of nonlinearities that may affect aeroelastic systems.

Tang and Dowell [8] introduced a free-play nonlinearity in the torsional stiffness and examined the nonlinear aeroelastic response. For various initial conditions, they created maps of the system response to describe locations of periodic limit cycles, chaotic motion and divergent motion. They concluded that limit cycle motion is dependent upon free stream velocity, initial pitch condition, magnitude of the free-play nonlinearity, and initial conditions.

Lee and LeBlanc [9] performed a numerical analysis of a nonlinear wing model using a time-marching scheme that simulated aeroelastic motion. Softening and hardening cubic stiffness was examined by varying the mass ratio, increasing the distance between the elastic axis and the centre of mass, and varying the ratio of the plunge frequency to pitch frequency. For the spring-softening

case, unstable motion was encountered below the linear flutter speed for nearly every parameter examined; however, increasing the nonlinearity and increasing the mass ratio tended to make the system more unstable at lower velocities. For the spring-hardening case, limit cycle oscillations were always present instead of flutter. Varying the parameters for the spring-hardening case affected the amplitudes of the limit cycle oscillations. Regarding the considerations concerning the surface actuation system, different models have been used in literature, as follows. Allen et al. [10] used a simple mathematical model of the actuation system which converts the required flap deflection angle δ_r into a corresponding torque applied to the surface characterized by inertia, damping and aerodynamic hinge moment, thus producing the effective flap deflection angle δ . As a consequence, the motion of the main aerofoil surface (heave and pitch degrees of freedom) may be performed. Ursu et al. [11] mathematically modeled the flap actuation system by means of a first order linear model relating, substantially, the required deflection angle δ_r (expressed in terms of equivalent actuation current) to the effective angle δ . Block and Strganac [12] mathematically modeled the flap actuation system by means of a second order linear model directly relating the required surface deflection angle δ_r into the effective deflection δ ; this model is substantially equivalent to the corresponding Allen's model, but, differently from the latter, employs directly, as an input, the required deflection angle δ_r

force opposing the motion, without any consideration regarding the standstill condition in which adhesion forces are present, as taken into account in the present work.

The aim of this paper is to analyze the aeroservoelastic behavior of a typical wing with active flutter suppression performed by a fly-by-wire hydraulic servomechanism equipped with an adequate control law. In particular the purpose is to point out and synthesize the effects of the selection of the active control law, taking into account several aspects characterizing the servomechanism behavior: the saturation affecting the actuation rate, the dry friction affecting the position accuracy and more realistic models of the main components of the hydraulic servosystem, as reported in figure 2 and in references [15] and [16].

2 DESCRIPTION OF THE AEROSERVOELASTIC MODEL

Figure 1 shows the typical wing section that is used to derive the structural equations of motion. The two degrees of freedom associated with the aerofoil motions are the vertical displacement h and the pitching displacement θ . The displacements are restrained by a pair of springs attached to the elastic axis with linear spring constants K_θ and K_h and cubic one $K_{\theta c}$ and K_{hc} respectively. The airfoil is equipped with a trailing edge moving surface, whose position δ depends exclusively on the servomechanism

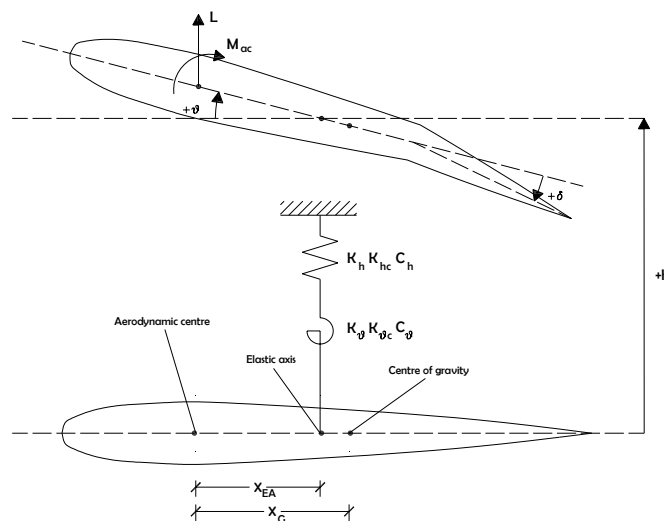


Figure 1 Aeroelastic parameter definition

instead of the corresponding torque externally applied to the surface.

Dimitriadis and Cooper [13] mathematically modeled a hydromechanical flap control system along the lines suggested in Wright [14]: it has a pressure feedback spring alternatively characterized by a bilinear behavior or freeplay or backlash, as reported in reference 13. So, the model takes into account actions related to the surface velocity and displacement; further, the effect of the oil bulk modulus is computed, while no inertial term appears in the equilibrium equation. Also a very simple friction model is considered, consisting of the introduction of a

position and is not affected by the aerodynamic and inertial loads. The servomechanism position depends, through its dynamic model, on the output of an adequate flutter suppression control law.

The aerodynamic model computes lift and pitch moment related to the aerodynamic centre as a function of the dynamic pressure, the initial value of the angle of attack α , the pitching displacement θ , the vertical and pitching rates and the surface deflection angle δ .

The structural dynamic model computes vertical and pitching accelerations related to the elastic axis as a function of aerodynamic loads L and M_{ac} , inertial loads,

weight, structural damping and stiffness. The structural damping is considered as a linear function of the speed, while the structural stiffness is modelled as a linear and cubic function of the displacement. The sign of the cubic coefficient takes into account the softening or hardening effects. The actuation system of the aerodynamic surfaces consists of a Power Control and Drive Unit (PDU, equipped with position transducers and tachometers), directly connected to the lever arm of the surfaces. The system control is performed by an Electronic Control Unit (ECU), which closes the position control loop. The PDU contains the hydraulic jack and the control valve.

The model of the actuation system, as reported in figure 2, takes into account the hydraulic and mechanical characteristics of all system components as follows:

- Coulomb friction in the PDU-surface assembly;
- third order electromechanical dynamic model of the servovalve with first and second stage ends of travel;
- fluid-dynamic model of the servovalve taking into account the maximum differential pressure, eventually time varying, performed by the hydraulic system1;
- dynamic and fluid-dynamic of hydraulic jack taking into account, beside the above mentioned Coulomb friction, viscous friction and internal leakage.

aerofoil surface (heave and pitch degrees of freedom). Hence, δ_r is evaluated according to the following equation

$$\delta_r = G_{h2} \ddot{h} + G_{h1} \dot{h} + G_{\theta 2} \ddot{\theta} + G_{\theta 1} \dot{\theta} \quad (1)$$

where the G's are the gains of the system.

3 SYSTEM COMPUTATIONAL MODELING AND RESULTS

The above described models have been used to build a mathematical model of the whole system and a dedicated computer code has been prepared. A structural model having linear and cubic softening spring characteristics around the pitch axis and linear along the vertical displacement is considered. The aerodynamic model is described as linear. Some simulations have been run in different conditions, having an operative or not flutter suppression active control. All the following figures show the behavior of the system in terms of vertical displacement h and pitching angular displacement θ : their trend is typically oscillatory, characterized by a frequency slightly depending on the corresponding amplitude, having an average value of approximately 14,5 Hz. The curves reported in the figures represent the envelopes of

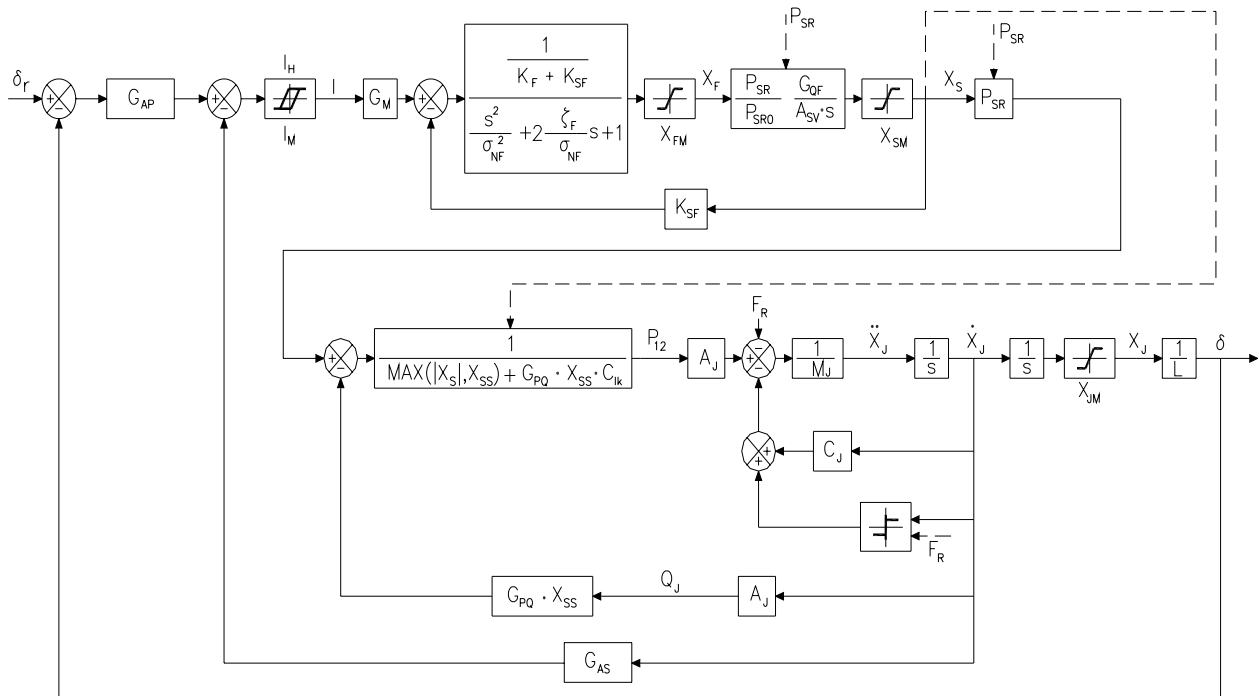


Figure 2 Block diagram of the model of the actuation system

The high complexity of the actuation system servomechanism model is requested by the necessity of taking into account the effects of the above mentioned several nonlinearities on the effectiveness of the flutter suppression active control.

Active control has been implemented within the proposed model, in order to investigate active means of flutter suppression via control surface motion. A simple control law is used which relates the required surface deflection angle δ_r to the speed and the acceleration of the main

the eventually damped oscillations.

Figure 3 shows the envelopes of the vertical displacement h and pitching angular displacement θ . The considered flight speed is slightly greater than the critical flutter speed: therefore a slow growth of the oscillations following the application of a large step perturbation concerning the pitching displacement at time $t=5$ s occurs. Figure 4 shows the effect of the active flutter control considered in this work on the behavior of the system of Fig. 3. Referring to eq. (1) the control law applies not null value only to the gain $G_{\theta 1}$. The effect of the active flutter

control is the stabilization of the system: in fact the oscillation amplitude decreases.

The trend of the oscillation decay shows the effect of important non linearities: between $t=5$ s and $t=12$ s the decay grows as the amplitude decreases, impossible behavior for a linear system.

Fig. 5 only differs from Fig. 4 in a greater value of $G_{\theta 1}$: the oscillation decay decreases. This behavior, seemingly inexplicable, can be justified as the effect of the increased actuation demand applied to the servo control, having related greater effects of the saturation concerning the actuation rate. An increased response phase delay is performed.

Fig. 6 applies (differently from Figs. 4 and 5) not null value only to the gain $G_{\theta 2}$: the behavior is much more stable than the in the previous cases. Under the same intensity of the corrective action, its effectiveness is largely due to its phase relative to the structural oscillation. In fact the ability to reduce the energy of the dynamic system is a function of the above mentioned relative phase. In the present case it has been observed that the greatest energy reduction in each cycle occurs when the corrective action phase is nearly the same as the pitch angular acceleration: so, varying the gain $G_{\theta 2}$ (related to the pitch angular acceleration), it is possible to maximize the energy reduction in each cycle and therefore the oscillation decay compared with Figs. 4 and 5. By means of a parametric analysis, justified by the strong non linearities involved in the system, the optimal value of $G_{\theta 2}$ has been obtained; in fact its damping effectiveness does not increase indefinitely as a function of the control gain. When the gain value is smaller than the optimal one, the effectiveness is lower, owing to the predominant linear behaviors; when the gain value is greater, a reduced effectiveness is shown as a consequence of the increasing phase delay by which the servo control responds to the large inputs (limited maximum actuation rate).

The previous Figs. 4, 5, 6 are referred to control laws depending only on the pitching angular displacement θ , the following Figs. 7 and 8 show the behavior of the system having a control law based on the vertical displacement h . In particular Fig. 7 applies not null value only to the gain G_{h1} , whereas in Fig. 8 the only not null value regards the gain G_{h2} . The aforesaid values too arise from a parametric optimization justified by the same above mentioned considerations.

The active control referred to the vertical displacement (as shown in the Figs. 7, 8 compared with Figs. 4, 5, 6) presents a lower effectiveness with respect to the control law referred to the pitching displacement. The reason of this behaviour is probably the consequence of the less suitable phase by which the control action interacts with the structural oscillation: it produces an energy reduction in each cycle lower than the same in the case of active control by means of the gain $G_{\theta 2}$.

It is possible that an active control having an intermediate phase between $G_{\theta 1}$ and $G_{\theta 2}$ produces more damping effects: Fig. 9 shows the case in which both $G_{\theta 1}$ and $G_{\theta 2}$ have not null values. No appreciable improvement with respect to the previous case of Fig. 6 (only $G_{\theta 2}$ not null) is

obtained. Probably that is justified by the reason that the proper corrective action, having the structural and aerodynamic data considered in this work, is that applying the only $G_{\theta 2}$.

Similarly the case regarding the contemporary presence of not null values of G_{h1} e G_{h2} has been studied (Fig. 10). No appreciable improvements with respect to the cases having only singular corrective actions [$G_{h1} \neq 0$ (Fig. 7) - $G_{h2} \neq 0$ (Fig. 8)] are observed, owing to reasons similar to the above mentioned ones. The case of contemporary presence of not null values of $G_{\theta 2}$ and G_{h2} (Fig. 11) and of $G_{\theta 1}$ and G_{h1} (Fig. 12) have been finally considered. No improvements with respect to the cases having only singular corrective actions, as previously said, are observed.

Referring to the case of Fig. 6 (with maximum effectiveness of the active control), flight conditions at higher airspeeds have been analyzed. As shown in Fig. 13, it is possible, at worst, to contrast the flutter in case of airspeed increase of 7%.

In all the above mentioned cases the initial input (applied to the pitching angular displacement at time $t=5$ s) is considered a large input because it produces appreciable structural cubic softening and corrective actions giving rise to saturations in the servo control dynamics. The case of initial small input on the pitching angular displacement at time $t=5$ s, related to the same conditions of Fig. 6, has been analyzed (Fig. 14): faster oscillation decay is shown. It is possible to assert that the gain applied to the control law in the case of large inputs (Fig. 6) is conservative in the case of small inputs.

Finally Fig. 15 shows the system behavior in the conditions of Fig. 6 having an initial input applied on the vertical displacement at time $t=5$ s. Very fast oscillation decay is shown; it is probably due to the lower weight of the non linear behaviors of the servo control dynamics.

4 CONCLUSION

The results are referred to a defined set of structural parameters and initial input (with the exception of Fig. 15, having initial input applied on the vertical displacement); this set is kept as a constant for all the cases considered in the present work. Therefore the reported remarks are valid in this context only: a modified initial input (more or less large, or applied to the vertical displacement rather than to the pitching angular displacement), modified stiffness cubic terms, etc., certainly lead to different results.

In particular the considered configuration keeps constant values, in all the simulations, for the following parameters: geometrical dimensions, positions of the elastic axis, of the mass center, of the aerodynamic center, angular and translatory linear and cubic stiffness values, inertial characteristics, structural damping values and aerodynamic characteristics.

As a consequence, the angular and translatory natural modes and their interactions are unchanged. In the previous configuration the authors have noticed that the active control action through the gain $G_{\theta 2}$ is the most efficacious (optimal solution); it demands a value of the surface deflection angle proportional and in phase

coincidence with the pitching angular acceleration. However it is not possible to generalize these considerations: having different structural parameters, it is probable that a proper set of values of G_{θ_2} and G_{θ_1} , or of G_{h_2} and G_{h_1} could be the optimal solution. Indeed the combined action of the two gains related to speed and acceleration (90 degs phase delayed each other) allows a proper adjustment of the corrective control action related to the structural oscillations.

The effect of the servomechanism nonlinearities (servo valve saturation and related phase delay due to the limited maximum actuation rate) mainly relies on the reduced ability of the flight control to damp large oscillations, as it can be expected.

To conclude, the effectiveness of the active control depends on the ratio between the amplitude of the corrective action and of the input, and on their relative phase too. In fact the aim of the corrective action must be to maximize the dissipation of energy in each oscillation cycle.

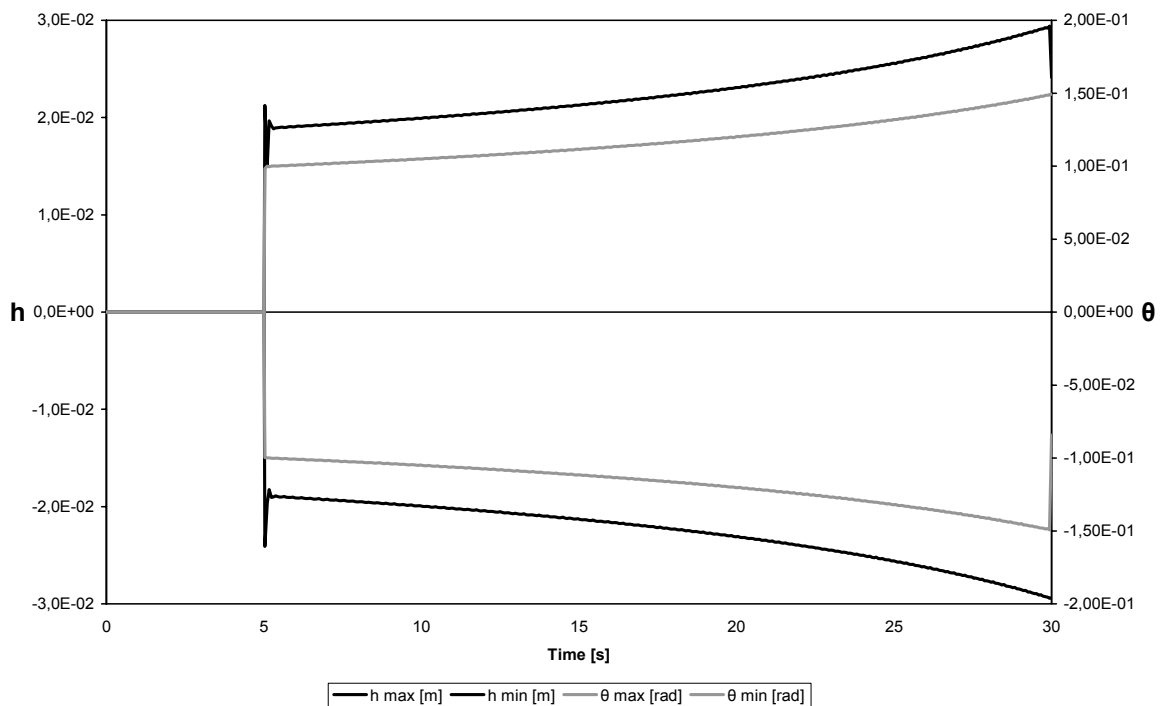


Figure 3

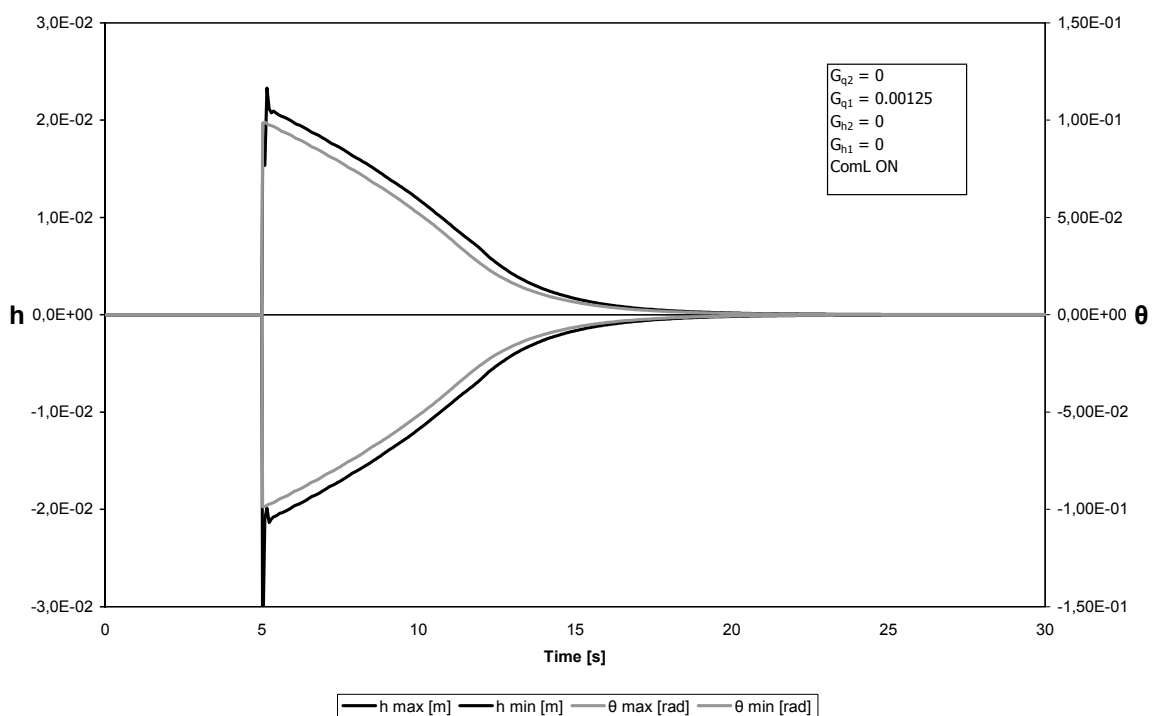


Figure 4

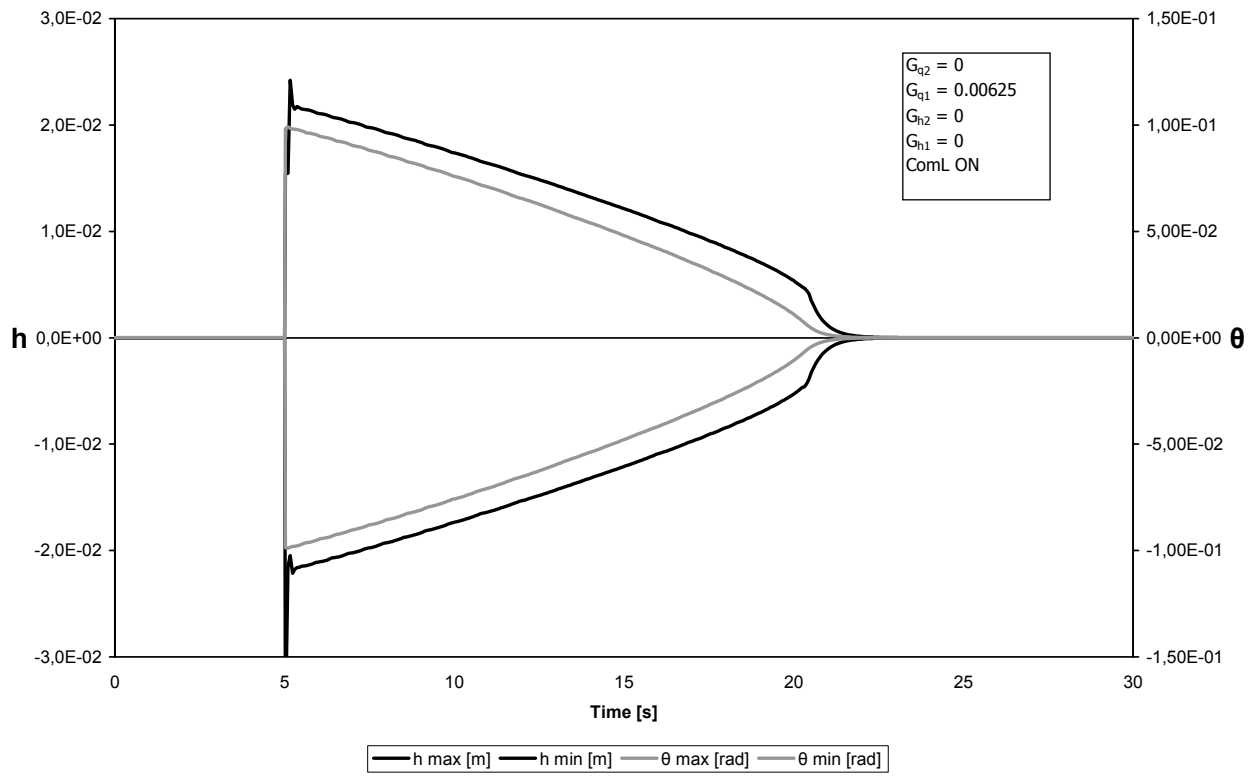


Figure 5

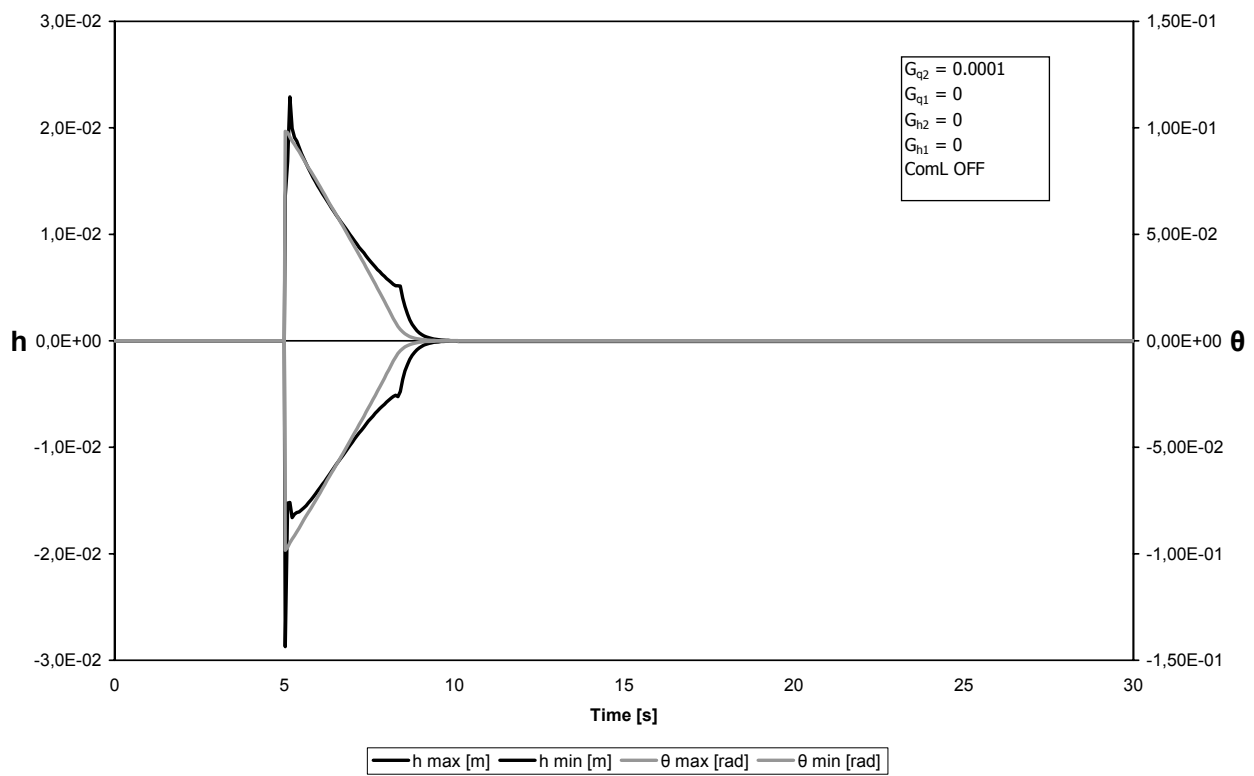


Figure 6

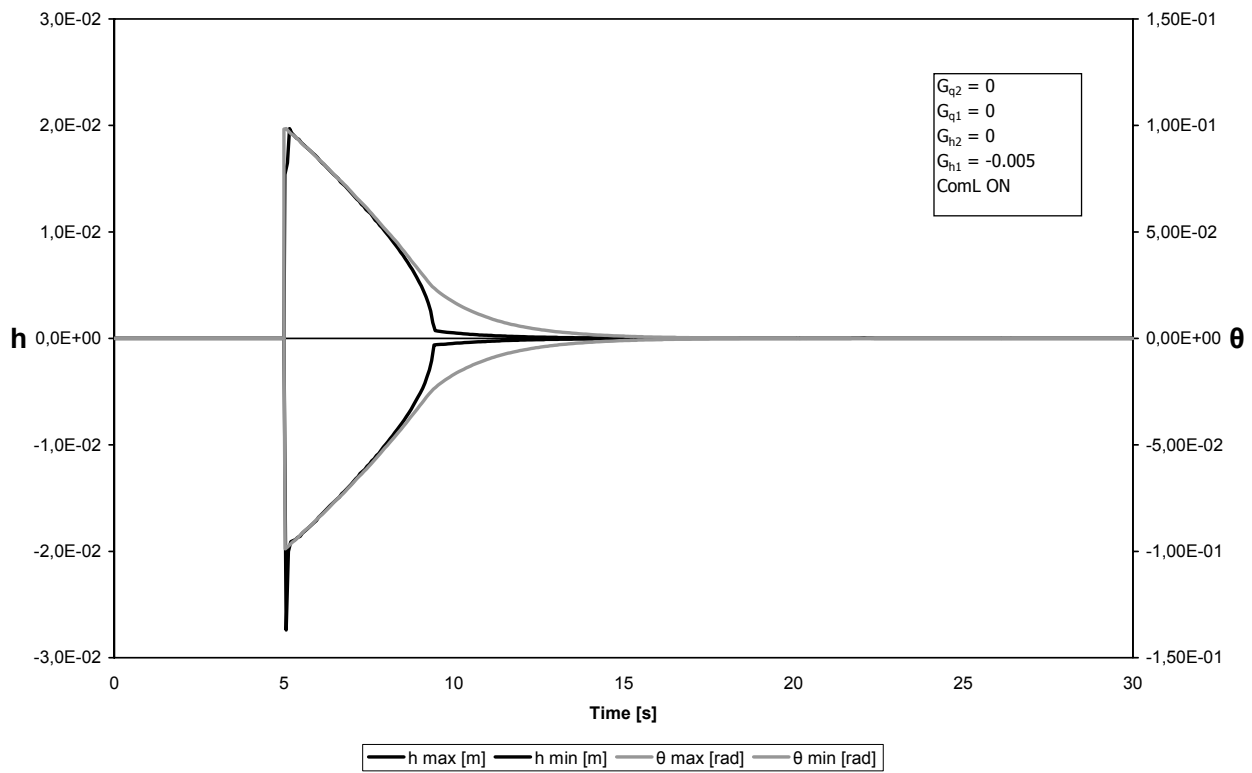


Figure 7

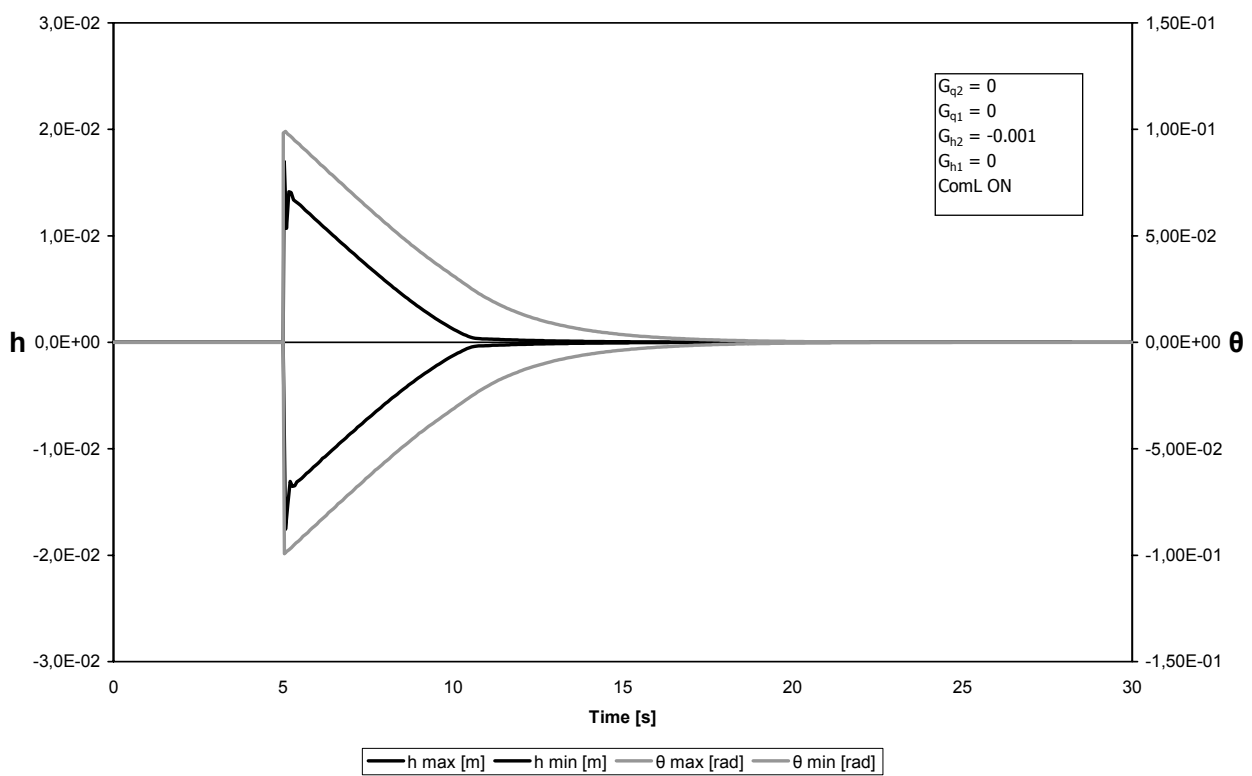


Figure 8

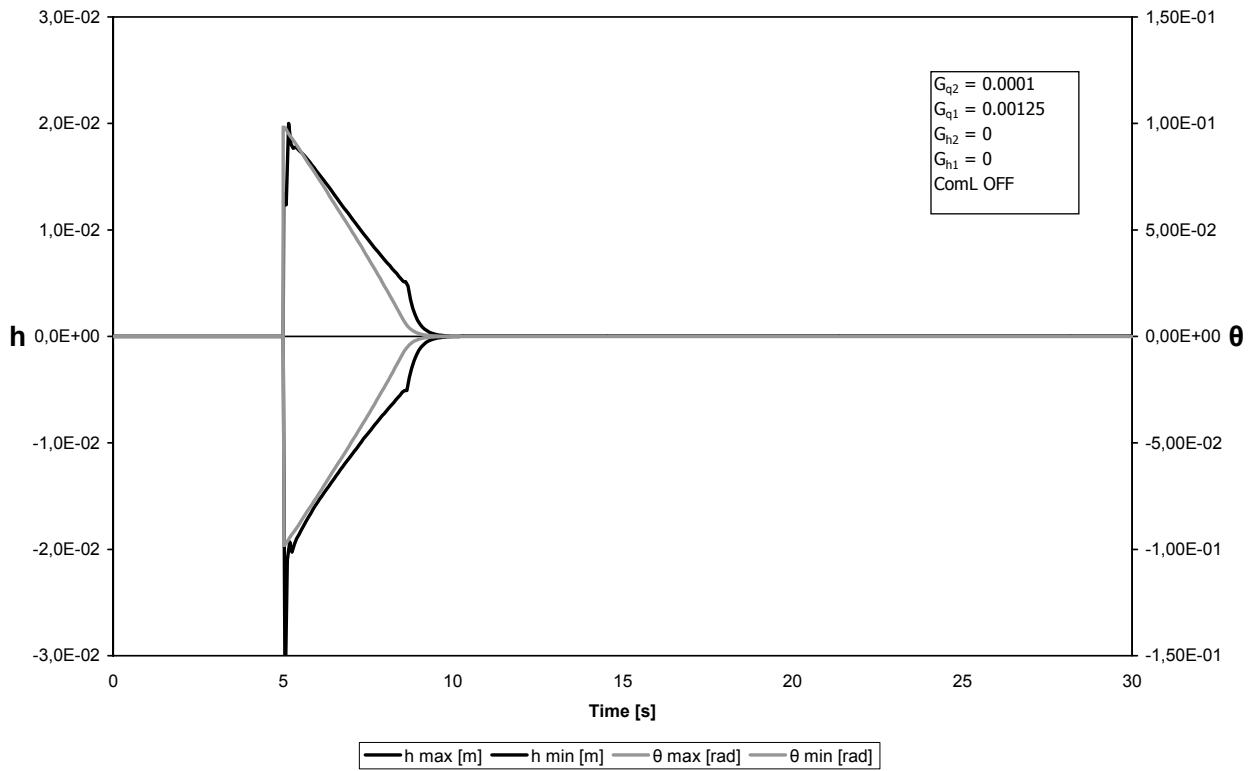


Figure 9

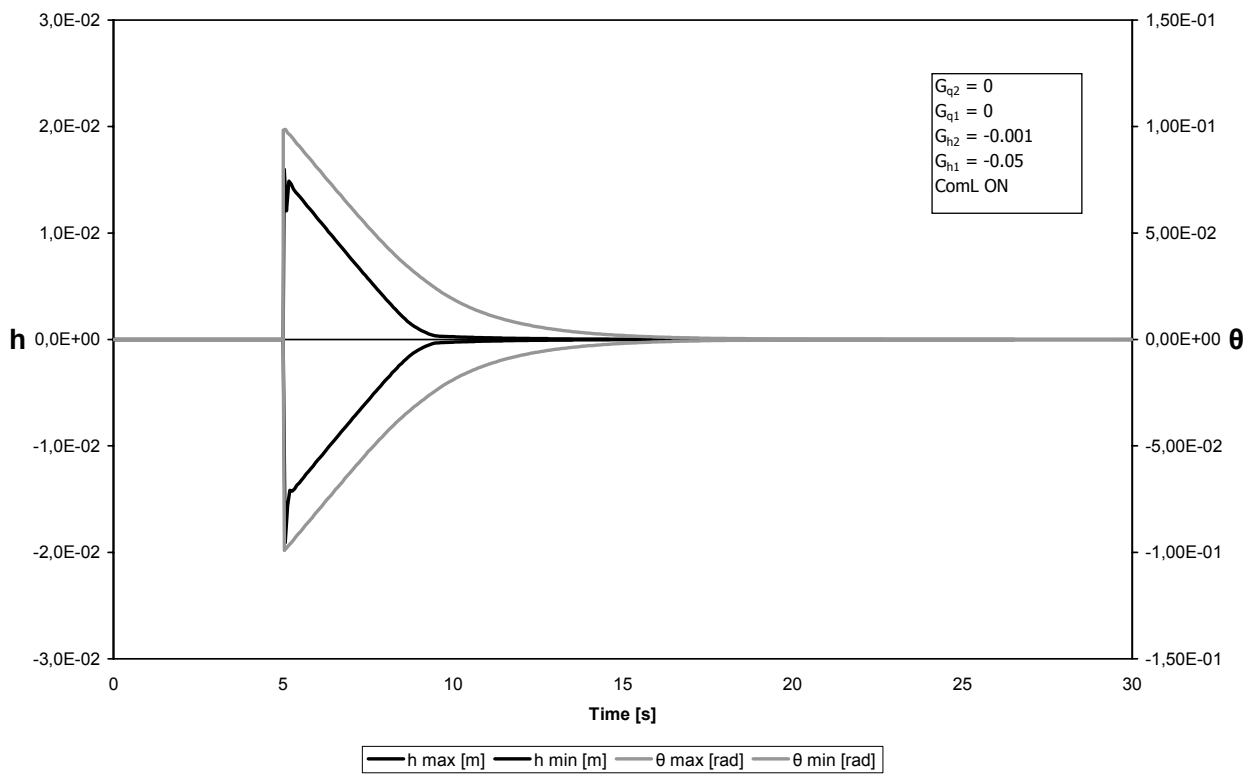


Figure 10

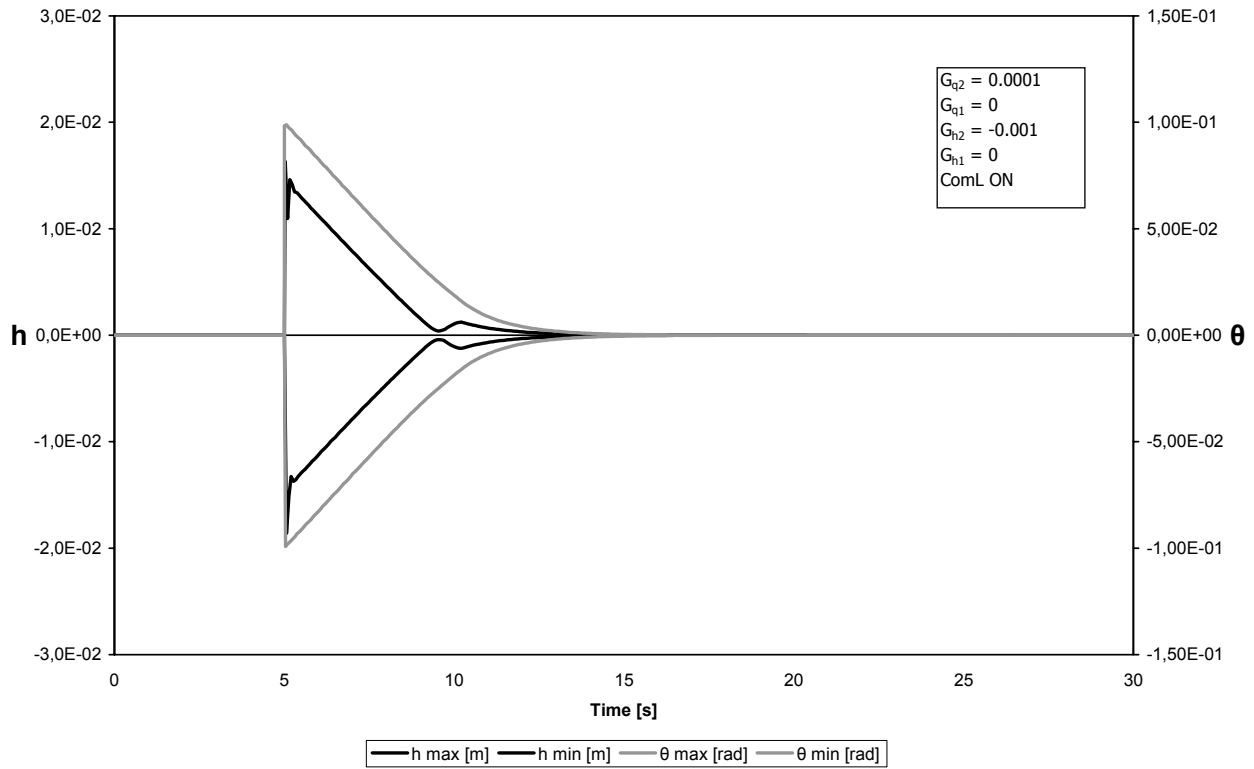


Figure 11

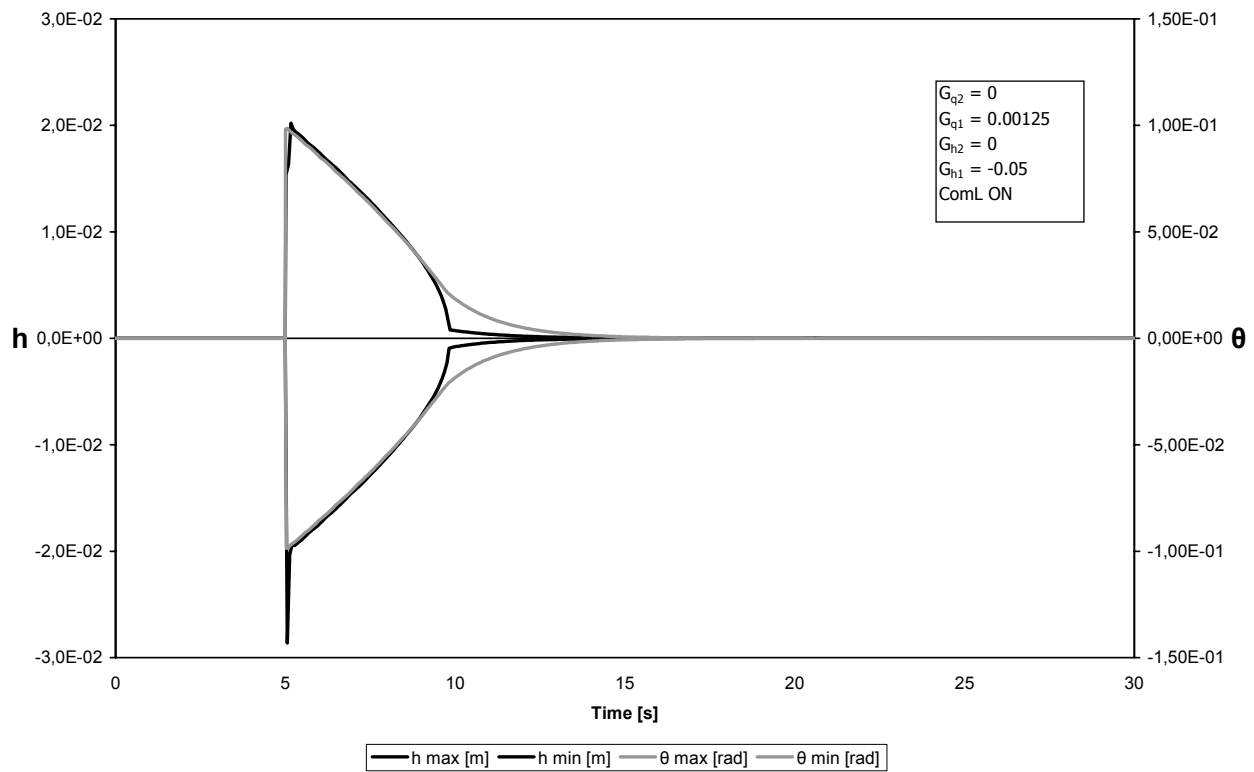


Figure 12

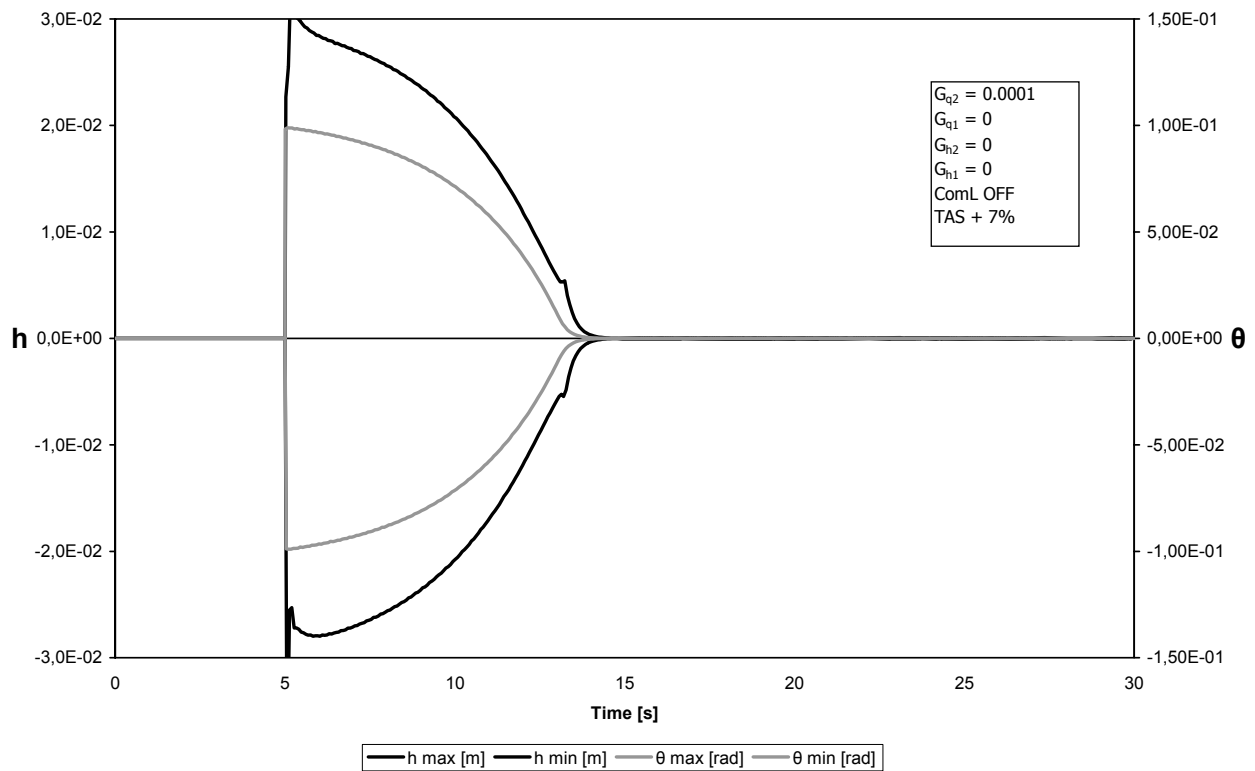


Figure 13

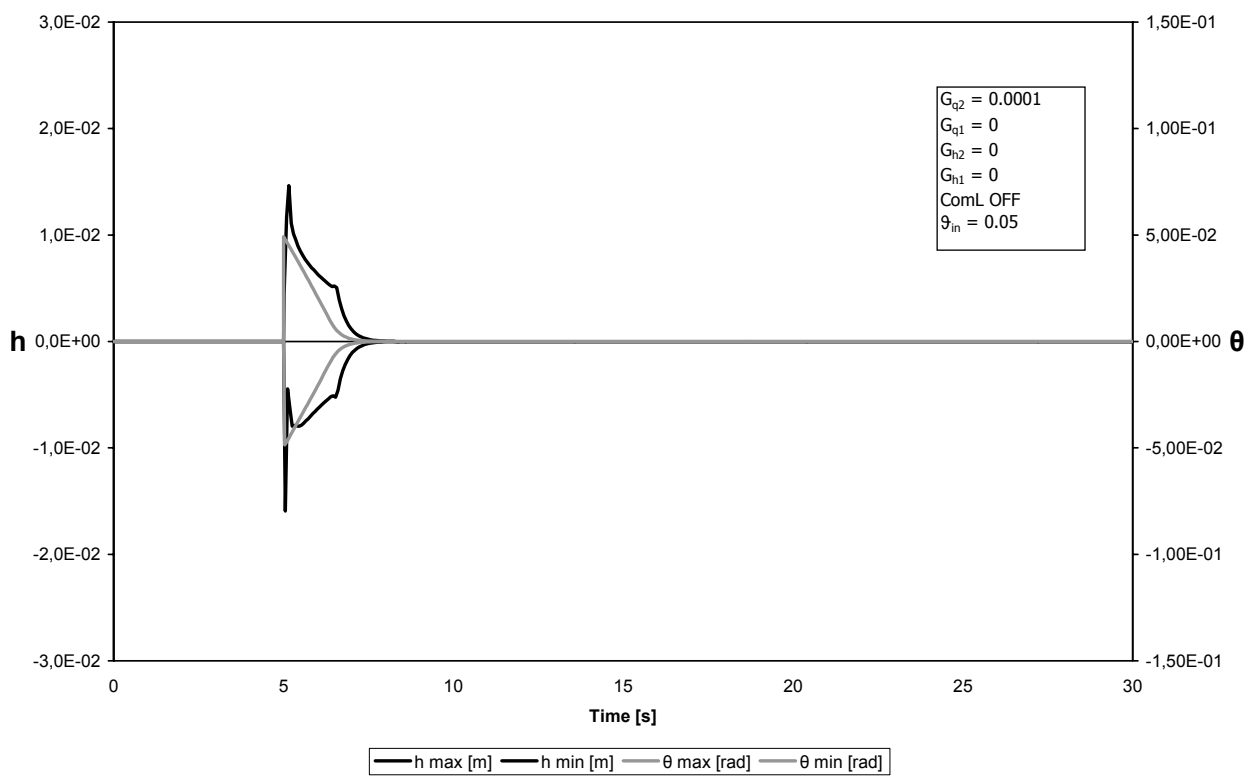


Figure 14

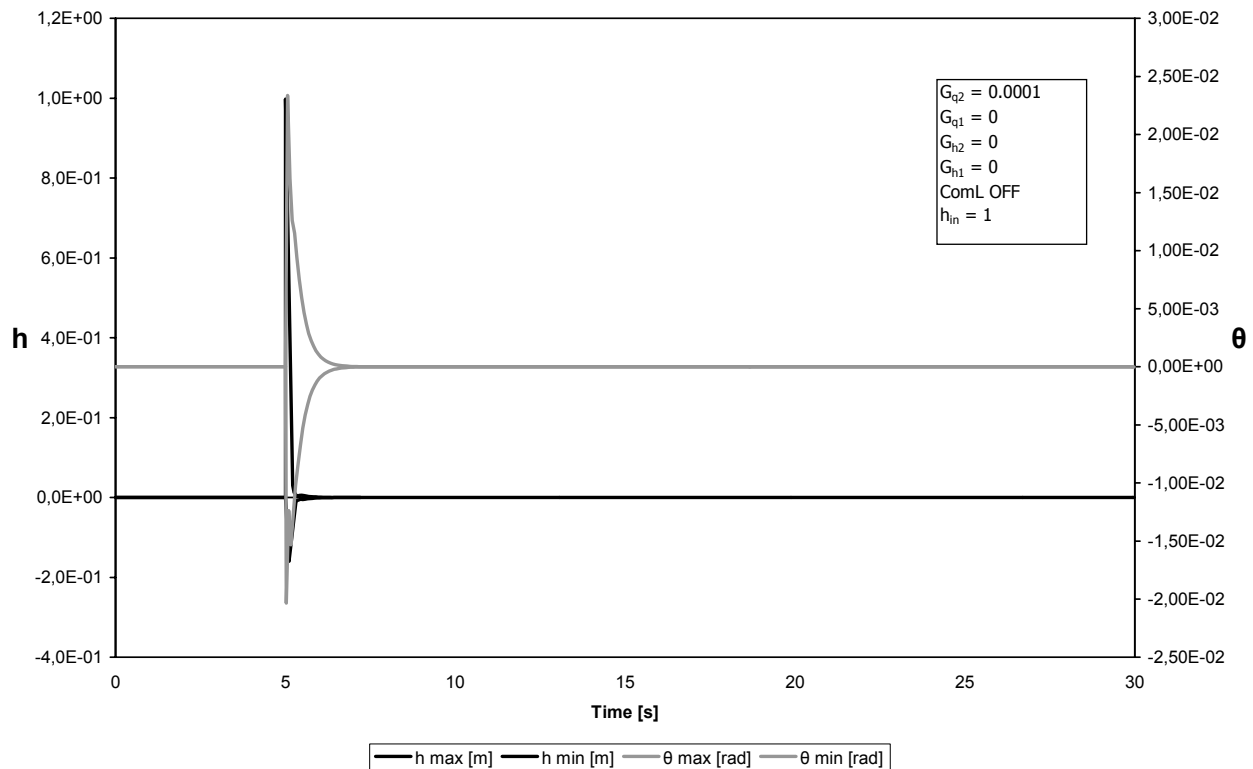


Figure 15

5 NOMENCLATURE

$ComL$	=	flight control input limitation [rad]
$G_{\theta 2}$	=	pitch acceleration control law gain [s^2]
G_{h2}	=	vertical acceleration control law gain [$rad \cdot s^2/m$]
$G_{\theta 1}$	=	pitch rate control law gain [s]
G_{h1}	=	vertical rate control law gain [$rad \cdot s/m$]
h	=	vertical displacement [m]
\dot{h}	=	vertical rate [m/s]
\ddot{h}	=	vertical acceleration [m/s^2]
K_{θ}	=	pitch displacement linear spring constant (stiffness) [$N \cdot m/rad$]
K_h	=	vertical displacement linear spring constant (stiffness) [N/m]
$K_{\theta c}$	=	pitch displacement cubic spring constant (stiffness) [$N \cdot m/rad^3$]
K_{hc}	=	vertical displacement cubic spring constant (stiffness) [N/m^3]
L	=	aerodynamic lift [N]
M_{ac}	=	aerodynamic moment [$N \cdot m$]
TAS	=	true airspeed [m/s]
α	=	angle of attack [rad]
θ	=	pitching displacement [rad]
δ	=	moving surface effective deflection angle [rad]
δ_r	=	required moving surface deflection angle [rad]

$\dot{\theta}$	=	pitch rate [rad/s]
$\ddot{\theta}$	=	pitch acceleration [rad/s^2]

REFERENCES

- [1] Lyons M. G., Vepa R., McIntosh S. C. and DeBra, D. B., Control Law Synthesis and Sensor Design for Active Flutter Suppression. *Proceedings of the AIAA Guidance and Control Conference*, New York, AIAA Paper 73-832, pp. 1-29, 1973.
- [2] Mukhopadhyay V., Newsom J. R. and Abel I., A Direct Method for Synthesizing Low-Order Optimal Feedback Control Laws with Application to Flutter Suppression. *Proceedings of the AIAA Atmospheric Flight Mechanics Conference*, New York, AIAA Paper 80-1613, pp. 465-475, 1980.
- [3] Gangsaas D., Ly U. and Norman D. C., Practical Gust Load Alleviation and Flutter Suppression Control Laws Based on LQG Methodology. AIAA, Paper 81-0021, Jan. 1981.
- [4] Karpel M., Design for Active Flutter Suppression and Gust Alleviation Using State-Space Aeroelastic Modeling. *Journal of Aircraft*, Vol. 19, No. 3, pp. 221-227, 1982.
- [5] Horikawa H. and Dowell E. H., An Elementary Explanation of the Flutter Mechanism with Active Feedback Controls. *Journal of Aircraft*, Vol. 16, No. 4, pp. 225-232, 1979.

- [6] Woolston D. S., Runyan H. L. and Andrews, R. E., An Investigation of Effects of Certain Types of Structural Nonlinearities on Wing and Control Surface Flutter. *Journal of Aeronautical Sciences*, Vol. 24, No. 1, pp. 57-63, 1957.
- [7] Breitbach E. J., Effects of Structural Nonlinearities on Aircraft Vibration and Flutter. AGARD-R-665, North Atlantic Treaty Organization, Neuilly sur Seine, France, Jan. 1978.
- [8] Tang D. M. and Dowell E. H., Flutter and Stall Response of a Helicopter Blade with Structural Nonlinearity. *Journal of Aircraft*, Vol. 29, No. 5, pp. 953-960, 1992.
- [9] Lee B. H. K. and LeBlanc, P., Flutter Analysis of a Two-Dimensional Airfoil with Cubic Nonlinear Restoring Force. *National Aeronautical Establishment, Aeronautical Note 36*, National Research Council (Canada) 25438, Ottawa, ON, Canada, Feb. 1986.
- [10] Allen C. B., Fenwick C. L., Taylor N. V. and Djayapertapa L., Investigation of Flutter Suppression by Active Control. *Proceedings 21st Applied Aerodynamics Conference*, Orlando, FL, AIAA Paper 2003-3510, 2003.
- [11] Ursu I., Stoia-Djeska M. and Ursu F., Active Control Laws for Flutter Suppression. *Annals of University of Craiova*, Vol. 27, 2004.
- [12] Block J. J. and Strganac T. W., Applied Active Control for a Nonlinear Aeroelastic Structure. *Journal of Guidance, Control, and Dynamics*, Vol. 21, No. 6, pp. 838-845, 1998.
- [13] Dimitriadis G. and Cooper J. E., Characterization of the behaviour of a simple aeroservoelastic system with control nonlinearities. *Journal of Fluids and Structures*, No. 14, pp. 1173-1193, 2000.
- [14] Wright J. R., Flutter test analysis method. *Ph. D. Thesis*, University of Bristol, U.K., 1975.
- [15] Jacazio G. and Borello L., A non-linear model of an electro-hydraulic servosystem with axial piston hydraulic motor. *International fluid power symposium*, Bath, pp. 45-55, 1986.
- [16] Borello L. and Villero, G., Flap Control Systems Actuators: Mathematical and Computational Model for Dynamic Simulation. *ECCOMAS 2000-European Congress on Computational Methods in Applied Sciences and Engineering*, Barcelona, 11-14 September 2000.

DYNAMIC ANALYSIS OF A SPUR GEAR UNDER MOVING LOAD

Tong Jingwei*, Xu Buqing**, Wang Shibin*, Bruno Picasso***

* Tianjin University, Tianjin 300072, China

** Shijiazhuang Railway Institute, Shijiazhuang 050043, China

*** Dipartimento di Ingegneria Meccanica, Università di Cagliari, Cagliari, Italy

ABSTRACT

In this paper two-dimensional and three-dimensional finite elements were used to analyze the gear dynamic root stress under moving loads.

Keywords: spur gear, moving load, finite elements.

1. INTRODUCTION

With the development of modern industry, mechanical instruments are made very subminiature or large-scale. The vibration and impact of gear on large-scale instrumentation are paid attention because gear is the most critical transmission accessory. A number of papers were published since finite element were used in gear's stress and strain analysis. For example, G. Charbet [1] analyzed stresses and deflection of spur gear teeth under strain by means of two-dimensional finite elements using one tooth model. Ramamuri and Ananda Rao [2] have calculated the variations of dynamic root stress with time using two-dimensional finite elements and a cyclic symmetry concept. D. B. Wallace and A. Seireg [3] have studied the variation of the dynamic stress with time under an impact load at three different points on the profile. M. A. Shhir Arikan and Bilgin Kaftanoglau [4] have studied the dynamic load and root stresses in a spur gear using the concept of mesh stiffness. S. Vijayarangan and N. Ganesan [6] studied the variation of the dynamic stress with time in a spur gear under a moving line load and impact load conditions by a three-dimensional finite element method.

In this paper we used two-dimensional and three-dimensional finite elements to analyze the gear dynamic root stress on a whole gear model.

2 LOAD SHARING BETWEEN TEETH

The ratio of load sharing in meshed teeth varies with time when the gear is running. According to gear handbooks, the load sharing is evaluated by the load sharing ratio χ_{Γ} in a mesh cycle. For an error-free spur gear, the load sharing ratio is shown in Figure 1.

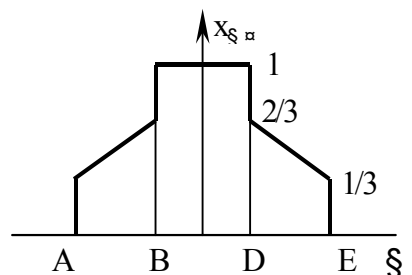


Figure 1 Load distribution coefficient along mesh line

$$\text{If } \Gamma_A \leq \Gamma < \Gamma_B \text{ then : } x_{\Gamma} = \frac{1}{3} + \frac{1}{3} \left(\frac{\Gamma - \Gamma_A}{\Gamma_B - \Gamma_A} \right)$$

$$\text{If } \Gamma_B \leq \Gamma < \Gamma_D \text{ then } x_{\Gamma} = 1$$

$$\text{If } \Gamma_D \leq \Gamma < \Gamma_E \text{ then :}$$

$$x_{\Gamma} = \frac{1}{3} + \frac{1}{3} \left(\frac{\Gamma_E - \Gamma}{\Gamma_E - \Gamma_D} \right)$$

So, the normal force at an arbitrary mesh point is

$$F = F_n x_{\Gamma}$$

The total transmission load does not vary when gear transmit torque. So the load sharing was distributed to corresponding two pairs of teeth when the mesh point is at the zone AB or DE.

3. 2-D FEM ANALYSIS UNDER MOVING LOAD

3.1 THE 2D FINITE ELEMENT MODEL

We have analysed the dynamic root stress of two involute standard spur working gear. Gear parameters are shown in the table 1 and table 2.

Table I - Gear tooth parameters

Parameters	Value
Module (mm)	5
Pressure angle	20°
Number of teeth	20
Transmission Ratio	1
Contact ratio	1.5568
Face width	1.2 m
Diameter of axial circle	4 m

Table II - Material properties

Material	Medium carbon steel
Young Modulus	205 GPa
Poisson ratio	0.3
Density	7800 kg/m ³

Because the contact ratio of a pair involute spur gear is greater than 1, the ratio of load sharing on different teeth varies with time. For an error-free gear, taking into account the effect of contact ratio, the load sharing ratio is shown in Figure 1. Because the transmission total load does not vary with time, the load sharing is distributed to corresponding teeth according to Figure 1 for FEM analysis purposes. The whole gear was meshed using plane, four-node 2-D elements. In order to increase the level of accuracy, several adjacent teeth under load were discretised using a relatively dense mesh. The whole model consisted of 1910 four-noded plane elements with 2066 nodes, 4132 degrees of freedom, as shown in Figure 2. The inner circle was fixed. The calculated gear is regarded as a driving wheel. The whole calculation process considers the whole meshing cycle during which the contact moves from the root to tip. The time origin was considered to correspond to the contact on the tooth root.

Running speed was 2000 rpm, transmission power 15 kW, total normal force is 1524.4 N. Because the contact ratio of the gear is greater than 1, the load was accordingly distributed on adjacent teeth. The total time was considered to be as 2500 μ s. This time was divided into 2500 intervals, 1 μ s each.

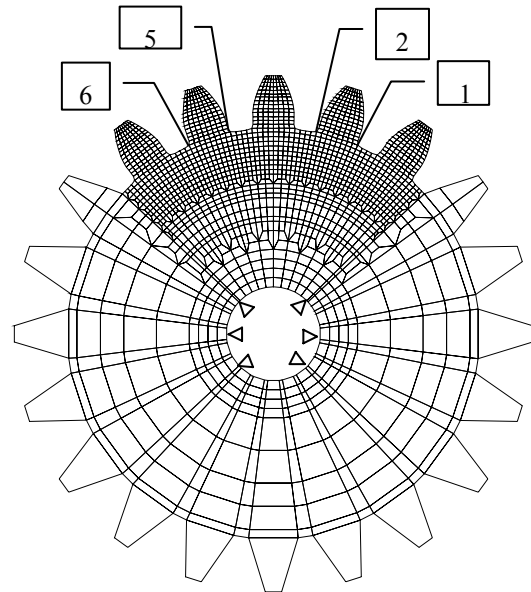


Figure 2(a) The finite element mesh of whole gear

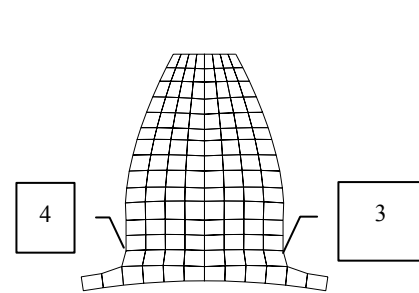


Figure 2(b) The tooth mesh

3.2 RESULTS

The following diagrams show the behaviour in time of the maximum and minimum principal stresses on different points on the tooth root. Being a 2D analysis the stresses found must be considered as a mean across the tooth depth. The analysis was linear neglecting local effects on load application points. Figure 3 shows the curve of the minimum principal stress of node 1 in I tooth with time. Figure 4 shows the curve of the maximum principal stress of node 2 in I tooth with time.

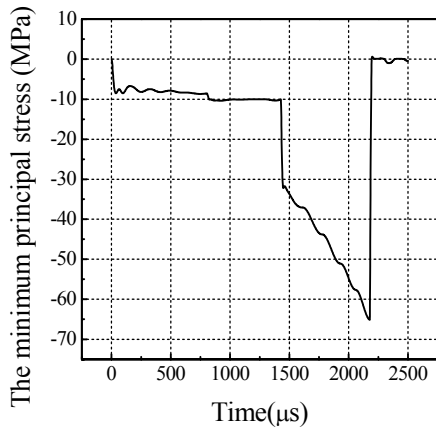


Figure 3 Root (node 1) min principal stress vs time

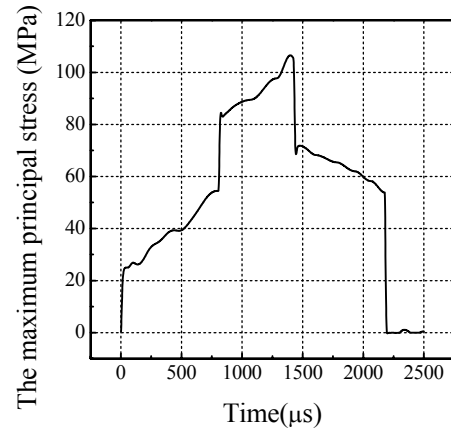


Figure 6 Root (node 4) max principal stress vs time

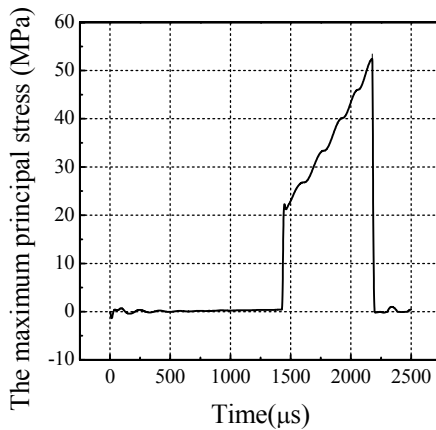


Figure 4 Root (node 2) max principal stress vs time.

Figure 7 shows the curve of the minimum principal stress of node 5 in III tooth with time. Figure 8 shows the curve of the maximum principal stress of node 10 in III tooth with time.

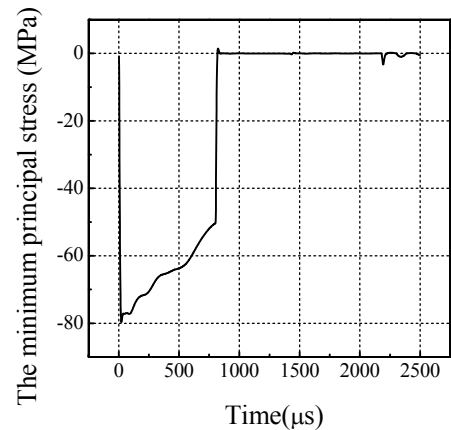


Figure 7 Root (node 5) minimum principal stress vs time

Fig. 5 shows the min principal stress on root of node II vs time. Figure 6 shows the max principal stress on node 4 in II tooth vs time.

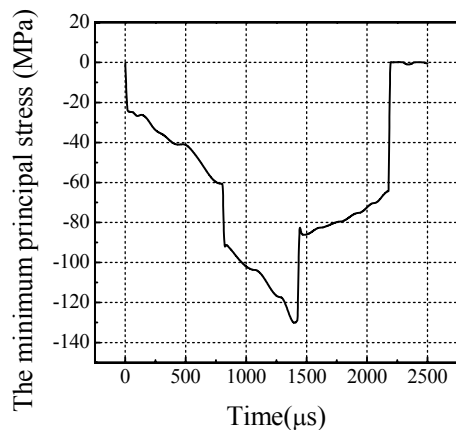


Figure 5 Root (node 3) min principal stress vs time

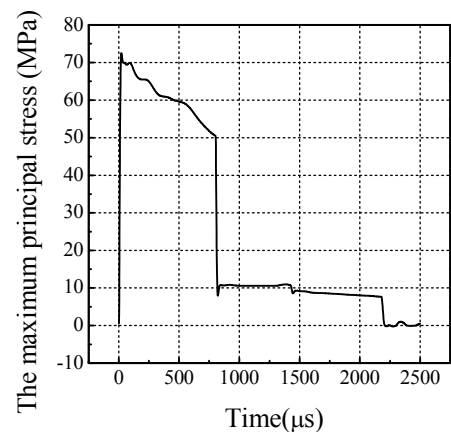


Figure 8 Root (node 6) maximum principal stress vs time

3.3 ANALYSIS

From figure 3 to figure 8 it can be seen that the root stress of nodes 1,2,3,4,5 and 6 varies with time as the mesh load. From figure 6, stress of node 4 increases more with time than the mesh load. As shown in figure 1, the reason is the mesh load increases continuously and the contact point is close to the tip in AB mesh zone. In BD mesh zone, though mesh load does not vary, the stress of node 4 still increases because the contact is close to the tip. In DE mesh zone, though the contact point is close to the tip and the meshing load decreases gradually, the stress of node 4 also decreased gradually.

From figure 3 to figure 8 it can be seen that the root stress changes abruptly at the points of the single and double pair teeth transition. The major cause is that the gearing load changes greatly on these point.

4. THREE-DIMENSIONAL ANALYSIS

4.1 3D FINITE ELEMENT MODEL

Because the analysis of three-dimensional finite elements can reflect the situation of gear more accurately, we used this method to analyze dynamic response under moving load. The size of pair of mesh gear, rotary speed and transmission power are the same as the analysis of two-dimensional finite element.

As in the two-dimensional finite element analysis, three-dimensional finite element analysis took the whole gear model. In order to obtain a high level of accuracy, several adjacent teeth under acting impact moving load were discretized using a relatively dense mesh. The whole model was divided into 2304 eight-noded brick elements with 3450 nodes. The inner circle was fixed.

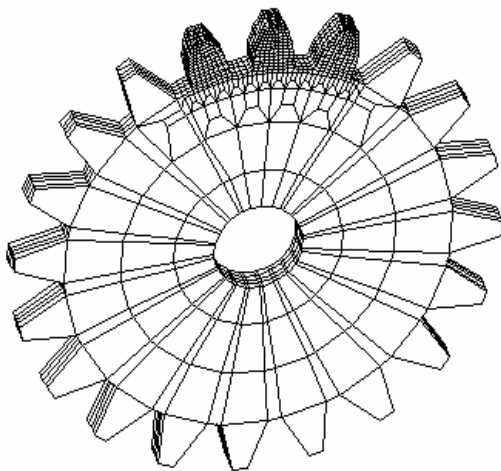


Figure 9(a) Finite element mesh of the whole gear

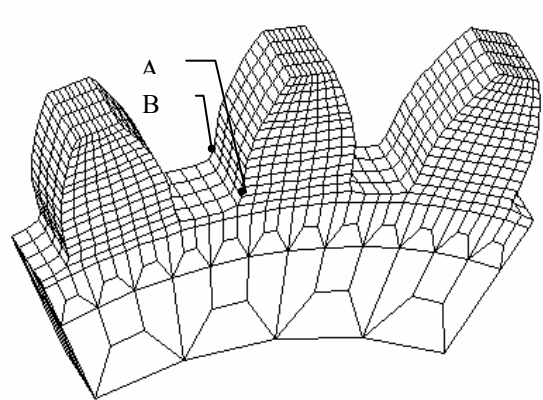


Figure 9(b) The finite element mesh of part gear

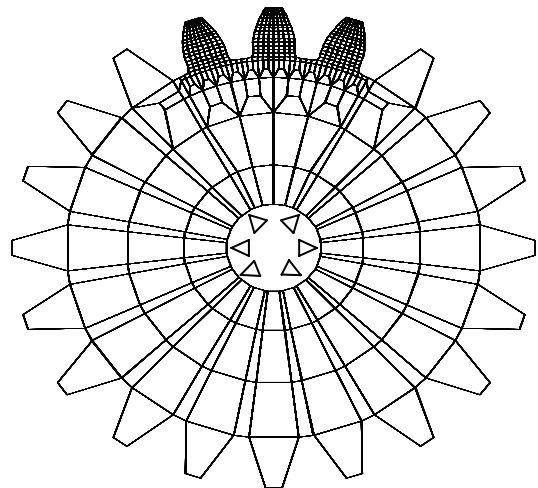


Figure 9(c) Front layer section of the whole gear

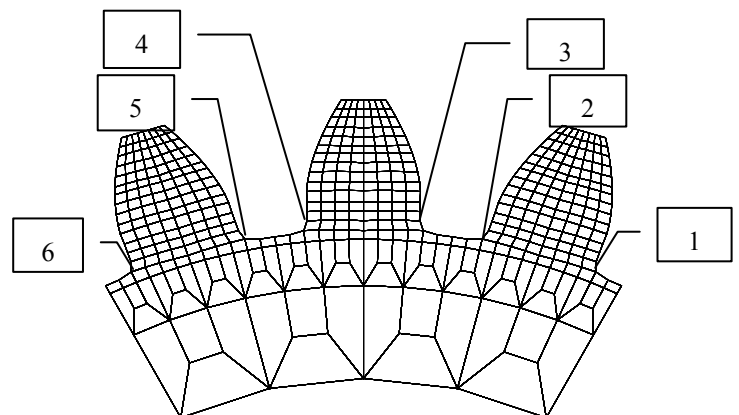


Figure 9(d) Front layer section of part gear

4.2 RESULTS

Figure 10 shows the curve of the minimum principal stress with time of root front section node 1 in tooth I. Figure 11 shows the curve of the maximum principal stress with time of root front section node 2 in tooth I.

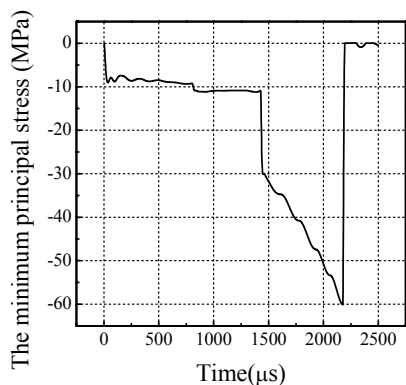


Figure 10 Min principal stress vs time (node 1)

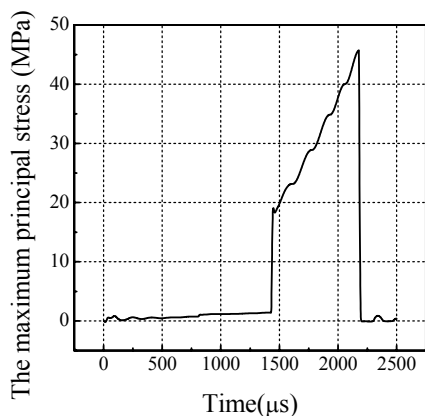


Figure 11 Root (node 2) max principal stress vs time

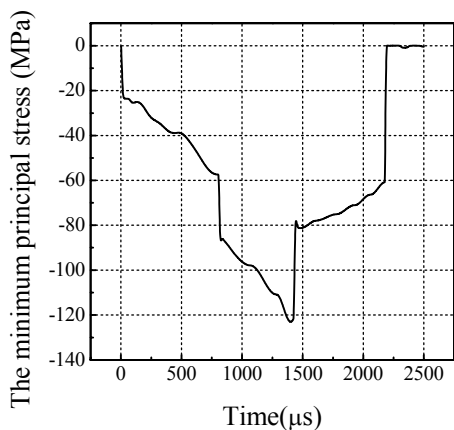


Figure 12 Root (node 3) min principal stress vs time

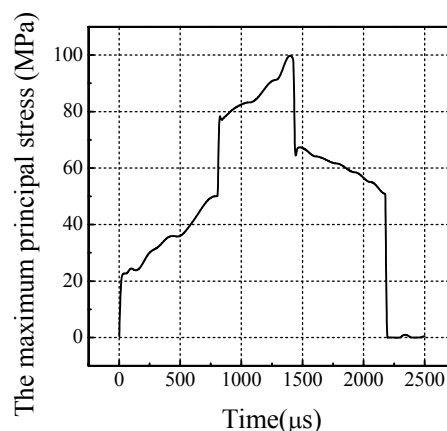


Figure 13 Root (node 4) max principal stress vs time

Figure 12 shows the curve of the minimum principal stress with time of root front section node 3 in tooth II. Figure 13 shows the curve of the maximum principal stress with time of root front section node 4 in tooth II.

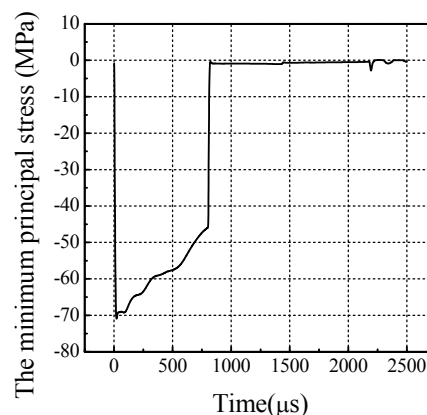


Figure 14 Root (node 5) min principal stress vs time

Figure 14 shows the curve of the minimum principal stress with time of root front section node 5 in tooth III. Figure 15 shows the maximum principal stress with time of root front section node 6 in tooth III.

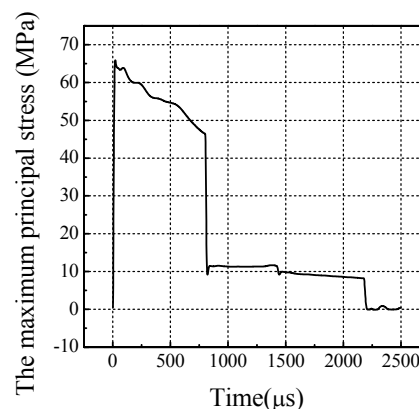


Figure 15 Root (node 6) max principal stress vs time

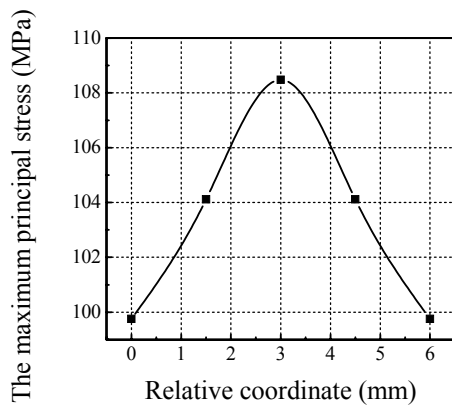


Figure 16 Maximum principal stress distribution on root nodes along gear axial direction.

Figure 16 shows the maximum principal stress of nodes along axial line AB when the stress of root node 4 comes to maximum. From Figure 16, though the contact load along axial direction is equal, it appears that the stress isn't equal and the stress of middle section is greater 8.05% than the stress on both sides.

4.3 ANALYSIS

From Figure 10 to figure 15 it can be seen that the root stress of node 1,2,3,4,5 and 6 varies with time as confirmed by the results of two-dimensional finite element analysis.

As for the root 1,2,3,4,5 and 6 of the front layer, the stresses of three-dimensional finite element analysis results are smaller than those of two-dimensional finite element analysis results.

5 CONCLUSIONS

- When the error-free spur gear was running, because the mesh load changed greatly at the point of the single and double pair teeth transition, the root stresses changed abruptly.
- As the same root point of front layer, the results of three-dimensional finite element analysis are smaller than those of two-dimensional finite element analysis.
- The results of three-dimensional finite element reflect the axial stress distribution greatly.

REFERENCES

- [1] G. Charbert, T. Dangtran, and R. Mathis, An evaluation of stress and deflection of spur gear teeth under strain, ASME, journal of Engineering for Industry, 1974,96, pp85-93.
- [2] V. Ramamurti and M. Ananda Rao, Dynamic analysis of spur gear teeth. Computers and Structures 29(5), 1988, pp832-843.
- [3] D. B. Wallace and A. Seireg, Computer simulation of dynamic stress, deformation, and fracture of gear teeth, 1973, Transaction of the ASME, Journal of Engineer for Industry, pp1108-1114.
- [3] M. A. Sahir Arilan and Bilgin Kaftanoglu, Dynamic load and root stress analysis of spur gear Annals of the CIRP 38(1), 1989, pp171-174.
- [4] T. Tobe and N. Takatsu, Dynamic loads on spur gear teeth caused by teeth impact. Bulletin of the JSME, Vol.16, No.96, Jun., pp1031-1037.
- [5] S. Vijayarangan and Ganessian. A Study of Dynamic Stresses in a Spur Gear under a Moving Line Load and Impact Load Conditions by a Three-dimensional Finite Element Method. Journal of Sound and Vibration (1993), 162(1), pp185-189.

TECHNICAL AND ECONOMIC ANALYSIS FOR THE RECOVERY OF HIGH BIOLOGICAL VALUE PRODUCTS FROM THE CHEESE-MAKING WHEY

Pier Francesco Orrù, Maria Teresa Pilloni

Mechanical Engineering Department of Cagliari University

ABSTRACT

The residuals of the milk transformation in a dairy industry are the scotta and/or the whey, depending on the production of the ricotta in addition to the cheese. Their disposal represents a technical and economical problem for the dairies due to their high pollutant content. At present, not being possible a direct disposal, such sludge are dried and used for pig nutrition. An alternative use consists in extracting, from these treatment residuals, high added value components, like, for example, lactose and serum proteins. In the present work a technical and economic feasibility study for the realisation of a plant for treating ovine milk serum is performed. The plant is located in Sardinia. Among the different technologies available on the market the one based on a membrane was employed, which allows the recovery and separation of the different components by means of subsequent crossings of different cut-off membranes. Eventually, the plant initial and operating costs were evaluated and the economic analysis of the investment was performed.

Keywords: whey, dairy, lactose, serum proteins, waste disposal

1 MILK PRODUCTION

In the last decade the dairy industry has experienced a significant growth, becoming today one of the most important industries in of the food sector. Worldwide, the milk production average annual trend of the last decade is around +1.83%. The growth peak is recorded in Asia, where the milk production has shifted from 83,3e⁶ tons in 1997 to 135e⁶ tons in 2007, resulting in an increment of 62% [1].

At the European level, Italy plays a key role in the milk transformation industry, being preceded only by France and Holland.

The majority of milk is produced in the north of Italy where the main milk cow farming are located. In the centre and in the south of Italy, conversely, ovine, goat and buffalo farming are predominant, with daily productions for single head by far lower than the ones from milk cows.

Unlike the north Europe countries, where few varieties of cheese in large dairy establishments are produced, in Italy

there is a great variety of cheese, and, more in general, of dairy products, produced by average and small size dairies. This is true with the exception of Grana Padano and Parmigiano Reggiano establishments, located in Lombardia and in Emilia Romagna, where large amounts of cow milk are treated.

Not all the milk produced in Italy is transformed in cheese: the greater part of the cow milk is employed as food in different forms (full-cream milk, semi-skimmed milk, skimmed milk).

Sardinia is the first national producer of ovine milk (67% of the national production) and goat milk (46%), a good part of which is employed for cheese-making.

Conversely, 95% of the cow milk from Sardinian production (representing about 2% of the national production) is collected by the Assegnatari Associati of Arborea and is mostly designated for human diet after UHT treatment. The production of milk is well distributed over the Sardinian territory, because, for historical reasons, in Sardinia intensive sheep farming never took place, and, till today, an extensive type of farming prevails.

The reasons of this choice are due to the fact that Sardinian territory is mainly an hilly area, and the pasture-lands are quite common and wide. In the last years the number of the

Contact author: P.F.Orrù

Piazza d'Armi, 09134 Cagliari - Italy

E-mail: pforru@dimeca.unica.it.

Sardinian dairies is remained almost constant, while the amount of milk they collected shows a growing trend. As far as the distribution of the dairies on the Sardinian land is concerned, an important concentration exists both in the regions of the low Campidano and around Sassari.

The prominent position of Italy and of Sardinia in the dairy – milk domain is certainly an advantage from the economic point of view, but, at the same time, the disposal and the treatment of its sludge (4,5 Mt/year in Italy) represent a technical-economic problem. On the basis of the DLgs 22/1997, from July 1999 [2] the first the milk whey is considered a waste to all intents and purposes.

The various milk production stages, in fact, include the use of water and washing reagents which require a purification process before their release in the environment. In the case of the skimmed and semi-skimmed milk production, the effluents become even more contaminating and difficult to dispose respect to the UHT milk production. The same is true for the plants producing milk by-products too, like, for example, the butter and the cream, in which the sludge are composed by the plant washing waters.

This sludge, due to the large amount of lactose content, reach COD (Chemical Oxygen Demand) levels between 6000 and 8000 mg/l of O₂.

Among the various activities of the milk industry, the cheese production is the most important both in terms of volumes and pollution content of the sludge. In particular, there is an high incidence of the organic rejects, the whey and the scotta.

The whey is the residue of the milk processing; from its further processing it is possible to obtain the ricotta, the reject of which is the scotta, which is very similar to the whey, but with a lower proteins content. The Sardinian production of scotta is around 223.000 t/year, 76% of which derives from ovine milk.

Whey and scotta have both very high values of COD and BOD (Biochemical Oxygen Demand), at least two order of magnitude over the limits imposed by the law.

The COD of the whey is in the range of around 60.000÷80.000 mg/l of O₂ and the COD of the scotta is in the range of 30.000÷50.000 mg/l of O₂ approximately.

The pollution generated by the whey and the scotta is quite similar because of the permanency of the lactose in the scotta. In detail, the law establishes that the waste with a COD lower than 160 mg/l of O₂ can be discharged in a surface water body, whereas, in order to be discharged in a sewerage and arrive to a consortium purifier, the COD limit is 500 mg/l of O₂.

These substances represent an heavy demand for the dairy industries mainly due to the corresponding disposal costs (quantifiable in about 3÷6 €/m³ of waste). To obviate this difficulty the dairies employ these waste as feeding material for pig farming. The feed is obtained by a thermal concentration process, followed by a drying stage, by which a whey powder is obtained characterised by serum-protein deficiency (with concentrations of about 15÷18%) and a low commercial value.

The limits of this kind of process derive by the temperatures reached during the concentration phase, which are higher than the temperatures at which the denaturation of the serum-proteins takes place. All that lowers the quality of the final product. In any case, the problem of the high environmental impact is not eliminated because the pollution coming from the evacuation of pigs fed in this way is higher than the one coming from the whey. In addition it must be taken into account that the small pig farmers are often lacking purification plants.

At present in Sardinia only one whey treatment plant exists, treating 30.000 t/year of liquid whey and scotta, from which around 2.000 t/year of feed are obtained.

In this work the technical and economic feasibility analysis of a plant for treating the ovine whey, located in Sardinia was performed. The target of the plant is the recovery of high added value components diluted in whey and scotta (lactose, serum-proteins, and so on), solving, at the same time, the problem of disposing the high pollution content substances.

2 THE WHEY COMPOSITION

The whey is a neutral, very diluted (94% of water content) solution; in suspension it contains:

- lactose: α -lactose, β -lactose;
- proteins: α -lactalbumin, β -lactoglobulin, serum albumin, immunoglobulin, lactoferrin, lacto-peroxidase, bioactive peptides;
- vitamins: B (thiamine), B2 (riboflavin), B5 (pantetine);
- mineral salts;
- fats.

Due to the high bacteria content, variable is the range 100.000÷2.000.000 UFC/ml, the whey easily ferments; this is mainly due to the high bacteria reproduction speed, which determines the transformation of lactose in lactic acid.

The chemical composition of whey and scotta is not constant, because the lactose and protein contents change as a function of both the kind of milk at the beginning of the process and the kind of cheese produced.

Table I - Average yearly composition of ovine whey and scotta [3].

PARAMETERS	OVINE WHEY	OVINE SCOTTA
pH	6,5	6,4
Density (g/cm ³)	1,02	1,03
Viscosity (cp)	0,8	0,75
Ash (g/l)	3,4	4,4
Fats (g/l)	4,2	0,5
Lactose (g/l)	44,3	45÷52,2
Proteins (g/l)	10,5	4,5÷8,0
Dry substance (g/l)	61,3	66,8

Moreover the milk composition varies during the year, because of the changes in the animal feeding. In table I a typical average yearly chemical composition of ovine whey and scotta is reported.

Among the vitamins, the riboflavin (B2) is employed for treating cardiovascular problems and cancer, for the positive effects on the eyesight and because it helps the iron absorption. The B5 vitamin produces a reduction in the cholesterol level and it is also used for the treating of cardiovascular illnesses.

The serum proteins have a biological value (BV) of 95%, greater than any other protein in nature (wheat has for example a BV of 61%). The biological value is the ratio between the quantity of ingested matter and the quantity of matter really assimilated by the intestine. In figure 1 the yearly average protein distribution of ovine whey is reported.

The most interesting among them are the β -lactoglobulin and the α -lactalbumin for their antioxidant, antitumoural and anti-hypertensive power and for their hypolipidic, antiviral and antibacterial properties. The bioactive peptides are protein fragments deriving by the breaking, by means of hydrolysis, of protein fragments (α , β , κ -caseine, α -lactalbumin e β -lactoglobulin). The peptides excite specific physiological reactions at behavioural, hormonal and gastro-intestinal level.

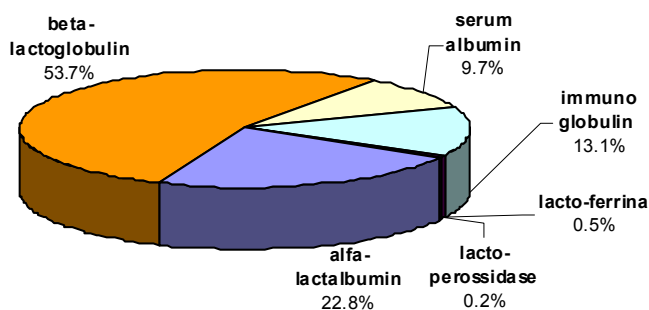


Figure 1 - Yearly average protein distribution of ovine whey.

The lactose is a sugar and may appear in two different crystalline shapes, the α -lactose and the β -lactose. The first one is the hydrous shape (at 5%), and is the most interesting from a commercial point of view; the second one, the β -lactose is the anhydrous shape, less noble and with a lower commercial value. Lactose is a widely employed component both in the food industry (for food sweetness reduction, food consistency increase, high absorption of aromatic substances, nutritive and caloric effect) and in the pharmaceutical industry (filler for tablets).

A different purity level of lactose characterise the different employments, 97% for food grade and 99.9% for the pharmaceutical grade. As a disadvantage, in some cases, a lactose intolerance at various levels was registered. From the hydrolysis of lactose (splitting by enzymatic or catalytic

way) it is possible to obtain glucose and galactose, both highly digestible and water soluble, low-calory and rich of notable sweetening properties (greater respect to lactose).

In front of β -galattosidasi, glucose and galactose may be grouped again, by means of specific industrial processes, like hydrolysis, the treatment with enzymes, or other particular processes (catalytic isomerization) to get the GOS (galacto-oligosaccharides). These components are employed as prebiotic because they encourage the proliferation of bifidobacteria in the gut, which, in turn, have positive effects on the absorption of the nutrition compounds and have, in addition, anti cancer properties. The selling prices, similar to those of the bio active peptide, are around 40 \$/kg.

3 THE MARKET OF THE WHEY BY-PRODUCTS

In the last years the serum proteins have become a sought-after item in the food-processing industry, in the pharmaceutical industry and in the firms producing sports integrators (the market grows about +13% each year).

The market presents different families of serum proteins derived products, each with different characteristics and prices.

Serum powders are obtained simply by removing almost totally the water from the serum by means of a drying process and are mainly committed to the zootechnic feeding. The proteins generally marketed in the food-processing industry have low proteins contents (around 35%) and high lactose contents.

Vice versa, the concentrated whey proteins (WPC) derive from UF and DF whey processes and have a protein contents varying in the range of 75÷85% and a content of fats and lactose under 5%. They are high quality proteins with an excellent quality/price ratio.

The isolated whey proteins (WPI) are obtained by means of ionic exchange chromatography techniques applied to the concentrate from the UF and DF processes. The powders obtained present a protein content higher than 90% and a quantity of fats and lactose lower than 1%, with very high selling prices.

All the proteins on the market are marketed under powder shape: this makes easier their transportation and guarantees a longer lifetime.

In table II the average selling prices (related to 2007) of the main serum protein substances derived from whey are reported.

Table II - Average selling prices of the serum proteins substances of whey.

SUBSTANCE	PRICE
Serum powder (zootechnic feed)	700,00 €/t
WPC 34	2.231,00 €/t
WPC 80	4.220,00 €/t
WPC 80 + WPI	29÷48 €/kg

As far as the bioactive peptides are concerned, they are still at the study stage, thus their market still does not exist, with the exception of small quantities analysed in the research laboratories.

Lactose is the most abundant (45g/l on average) and easy to market product of all the whey treatment process. Lactose is very widely employed in the food-processing and in the pharmaceutical industry. The different purity level required in these two applications also determines a difference in the selling price.

For example, the pharmaceutical grade lactose is characterised by a purity level of 99.9%, obtainable only after a double serial crystallization process. The market of lactose for food use is very competitive and its selling price is about 639,00€/t. Vice versa, as far as the pharmaceutical use lactose is concerned, the single firms have direct private contacts with their suppliers: therefore an official price trend does not exist. The only available data derives from the Bayer AG, one of the greater pharmaceutical firms of the world, which during the year 2006, has charged an average price of 9,84 €/kg [4].

4 THE RECOVERY TECHNOLOGIES

The traditional processes for treating the whey are manifold:

- Precipitation: with this method, the formation of protein complexes is generated by means of strong acidification or through the formation of a serum protein complex by poly-electrolytes (iron salts, poly-aluminates, tannin, carbosimetylcellulose, chiosane, etc.). With the poly-aluminates method, non denatured serum protein can be recovered, the main disadvantage consisting in the heavy metals final product contamination.
- Thermal concentration: it is the most widely employed method at the industrial level; the process consists in drying the whey by means of a vacuum evaporation followed by a spray dryer stage. At the end of the process, a low commercial value product is obtained, because the powder is rich of lactose and poor of serum proteins, which is generally employed in the zootechnic sector. Very often, in this treatment, the serum proteins denaturation temperatures are exceeded, both in the evaporation and in the atomisation stages, this resulting in a lower quality of the final powder. Moreover, the evaporated whey, subsequently condensed, has a COD of the order of 1.000÷2.000 mg/l of O₂, which requires a further depuration.
- Selective serum proteins adsorption: ionic exchange resins are employed; the process is very competitive in many aspects, but it is also complicated by the necessity of removing the serum proteins by the support, which also determines a dilution of the product which later will have to be dried.
- Gel filtration: it is based on the separation of the serum proteins from the solutes at low molecular weight as lactose and salts. The adsorption resins are generally composed of more or less reticulated dextrans which first adsorb the serum proteins and later release the serum proteins by employing suitable buffer substances, added with NaCl at different concentrations. This process allows the separation of the serum proteins but presents the disadvantage of high costs and is besides complicated by the production of extensive quantities of liquid effluents.
- Selective precipitation: it takes place as a function of both the pH and the ionic power, playing on the isoelectric point of the different serum proteins families. For example, by bringing the pH of the whey at 4.2 and heating the solution till 65°C, the α -lactalbumin denaturation occurs; then the α -lactalbumin precipitates. By bringing the pH of the whey at 4,65, by electro dialysis the precipitation of the α -lactoglobulin is obtained. By means of subsequent precipitations, it is possible to obtain a solution poor in serum proteins and a very diluted precipitated in which the other serum proteins families remain.
- Electro dialysis: it allows the removal of great part of the mineral salts, by means of ionic exchange membranes internal to a direct current electrical field. From a functional point of view, the whey flows in suitable compartments between them. The electrical field allows the migration of the ions from one component to the other, thus impoverishing the whey of mineral salts which accumulate in the water. This process is widely employed for the production of whey and milk powders, but has the disadvantage of an high energetic consumption (about 20÷28 kWh/kg of produced powder).
- Anaerobic process: it consists in the fermentation of the whey inside suitable fermentation vessels named UASB (Up-flow Anaerobic Sludge Blanket) in the absence of oxygen. By this anaerobic digestion biogas is produced, which is low heating value methane because diluted with carbon dioxide. In the optimal process conditions, it is possible the production of about 23 l of methane from 1 l of crude whey. This technology requires high plant and management costs. The COD cut down deriving from the anaerobic process is on average around 90%. At the end of the treatment cycle, the residual mud can be employed as agricultural amendament.
- Membrane: it is the most widely employed process in the world, and consists in forcing the whey to pass through different cut membranes for selecting the serum components.

By comparing the technical, economic and environmental performances of the technologies illustrated the membrane results the most suitable for the separation of the whey components [5]. The stages of the process are the following:

- Micro-filtration (MF): eliminates the fat residuals and the microbic charge;
- Ultra-filtration (UF): collects all the serum protein families;
- Nano-filtration (NF): concentrates the lactose;
- Reverse Osmosis (RO): it produces demineralised water with a polluting charge lower than a COD 150 mg/l of O₂.

The whey fractioning process by membrane technologies is convenient when the matrix was not subjected to fermentation processes, in which the pH of the whey remains in the range 4,5-7. In order to guarantee this condition, it is necessary to employ the whey as soon as produced by the dairy, to cool it for possible tank transportation, and to avoid as much as possible bacterium fermentation phenomena which bring to the lactic acid formation and to the serum proteins hydrolysis.

5 THE RECOVERY PLANT

In this paper the technical and economic feasibility study for the realisation of a plant treating dairy waste located in Sardinia will be discussed. The plant serves a dairy recovering butter cream, zootechnic feed, serum proteins, lactose and ultra-pure water. The process residuals, due to their low polluting content, can be disposed in sewer.

The plant will work on a daily shift of eight hours for the whole year, with the exception of the period between the end of September and the end of November, during which the dairy production is reduced at 2/3 of the nominal value

due to the lower milk production of the ovine farming.

In figure 2 a block diagram with the indication of the flow rates in the different plant sections is illustrated.

Being the process a filtration and separation process, for each module the input is the food and the output is the filtered by-product (retentate or concentrated) which is stopped and the residual matrix (permeate) which will be sent to the following module.

From a functional point of view, what makes the processes different are the pressures applied, the typology and the selectivity of the membrane employed. The filtration takes place with polymeric or ceramic tangential membranes, which are located inside a cylindrical mechanical element called module (or vessel) which must be able to resist to the operating pressures.

Unlike the traditional filtering, which takes place perpendicularly to the filter, the tangential filtering generates a minor pores occlusion, thus avoiding sudden reductions in the system productivity. The ceramic membranes have the advantage of working well also with an high degree of fouling, can be washed with any detergent and have an average life longer than the polymeric ones. The membranes will be submitted to a counter-pressure periodic washing (back pulse or back wash) which allows the full recovery of productivity.

The cascade modular structure of the plant allows to identify a primary production line (de-creaming section, MF, UF and DF, NF and IO) from which some raw by-products are obtained, and some secondary lines, in which their refining takes place. Between the different sections, some tanks will be placed, for damping the variability of the flow rate at the inlet of the plant and in the single plant sections [6].

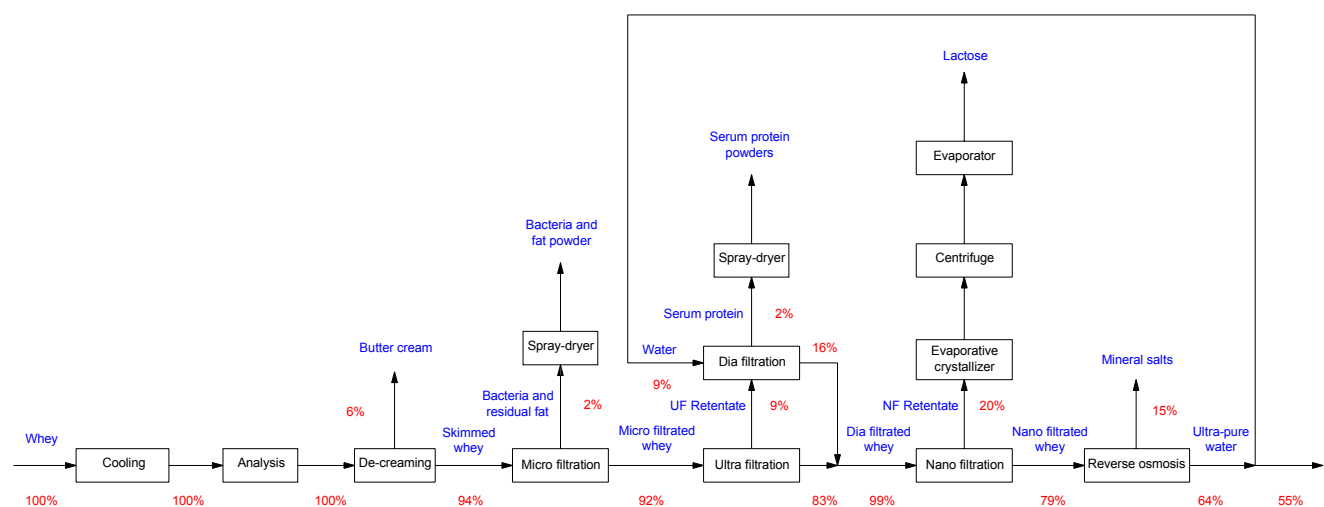


Figure 2 - Plant block diagram.

6 MAIN LINE

6.1 COOLING

The whey, which exits the dairy at a temperature of 85÷90°C, is cooled for avoiding the bacteria proliferation and the transformation of lactose in lactic acid and then is collected in a first storing insulated tank made of stainless steel AISI 304 where it is kept at a temperature of 25°C. Because of the variability of the inlet flow rate, the tank is designed for containing twice the hourly production.

6.2 WHEY ANALYSIS SECTION

Before being treated, the whey must be carefully analysed. In particular, pH and bacteria charge will be investigated. The first because of its influence on the efficiency of the filtering membrane, and the second because of its fast increase in the serum matrix; a too high bacteria charge, in fact, would make the final product unusable for commercial purposes.

The plant solution adopted allows to measure the whey pH and, if not falling in the established range, it is automatically corrected by means of a calcium carbonate supply, thus restoring the pH value inside the range (Figure 3). This guarantees a continuous production of the plant and the treatment of the whole inlet whey without losses.

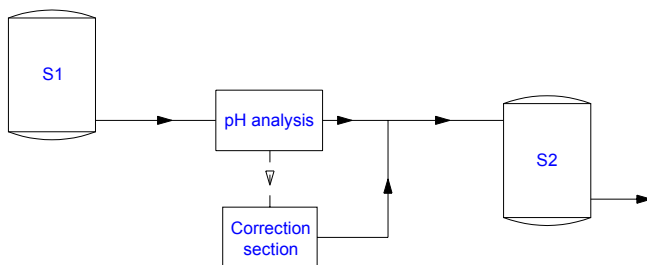


Figure 3 - Functional sketch of the analysis and correction section.

6.3 DE-CREAMING SECTION

In this section nearly all the fat included in the whey is separated. The ovine serum is a very fat effluent, and, if directly sent to the filtration section, it would occlude in a short time the MF membrane pores.

For the de-creaming process, suitable separating centrifugal machines are employed. Among the different possible options, an automatic instead of a manual de-creaming machine was chosen; in this way the discharge of the skimmed serum and the washing of the drum and of the mobile elements takes place automatically, by means of a management control unit without the aid of an operator.

On the basis of experimental tests [3] it was noticed that the de-creaming treatment takes place with an extraction efficiency of about 95÷96%, reaching a final fat concentration of about 0,185 g/l.

6.4 MICRO FILTRATION SECTION

The MF process does not allow to obtain a high added value product, but it is anyway necessary for guaranteeing the quality of the following filtrations. In fact, during the de-creaming, only a bacteria quantity lower than 1% separates by the whey, therefore the nearly entire bacterium charge of the raw serum remains unchanged in the de-creamed serum. In the dairy practice, for removing the bacteria, a pasteurization process is employed, which requires an heating of the fluid at a temperature of 60÷70°C for about 30 s.

In this case a pasteurization process cannot be applied, because the whey temperature increase up to the indicated levels would bring to the denaturation of the serum proteins, and this would cause a reduction of the quality of the powders obtained. Moreover the dead bacteria would not be separated anyway, and would remain suspended in the serum till the UF process, when they would be removed together with the serum proteins, thus resulting in a decay of the protein powder quality.

The efficiency of the process of the bacteria removal is about 97÷98% at temperatures of 25°C. The powders obtained by drying the MF retentate, can be employed for the zoo-technical feeding.

The values of the bacteria charge of the whey can be very variable on the base of the kind of milk employed, of the kind of dairy process with which it was treated, of the time elapsed before the whey treatment and on the base of several other factors.

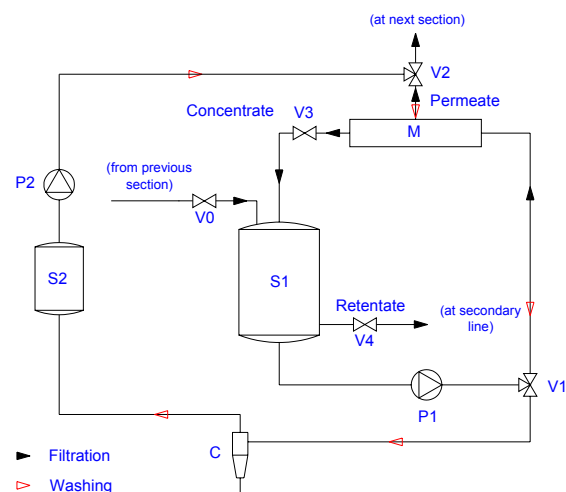


Figure 4 - Functional sketch of the filtration section.

Considering that the whey bacterium charge two hours after the production of Sardinian pecorino is on average included between 250.000 and 300.000 UFC/ml, an efficiency of 97% of the MF membrane allows to obtain an almost bacteria free permeate (9000 UFC/ml). In this section, 1.4 μm cut-off tubular ceramic membrane will be employed; their average productivity is around 180 l/(m² h) and the operating pressure is 4 bar [3].

The working cycle includes a filtration period of 25 minutes alternated with 5 minutes counter pressure washing (Figure 4).

6.5 ULTRA FILTRATION SECTION

The UF is an entirely mechanic separation process, operated with more selective cut-off membranes respect to the MF process, which allows to recover the protein component of the whey. With the simple UF of the whey, serum protein powders with a maximum concentration of 65% can be obtained. In order to obtaining powders with higher concentrations, it is necessary to remove the residual lactose from the UF retentate, by employing the DF.

Operatively, it consists in adding water to the UF concentrated, by recycling the resulting fluid in the filtering section. At the end of a DF cycle with a dilution ratio of 1:1, a retentate with a protein content higher than 85% is obtained.

Due to the low flow rates, a machine with average components between MF and UF/DF was considered. This configuration has the advantage of a lower plant cost and is commercially available, while, for daily volumes of the order of several cubic meters, specific machines are built on commission.

The disadvantages, conversely, mainly consist in the non continuity in the plant operation due to the sharing of feeding and recycling pumps, tubes and control systems, which determine an alternate operation of MF and UF/DF. In this case the alternate operation between MF and UF/DF allows to wash the membrane of the non operating section when the other one is filtering.

In this section a polymeric (polyamide) membrane is employed; it is a spiral membrane with a cut-off of 6 kDa, which, in the same operating condition of the previous section, allows to reach a productivity of 38 l/(m² h).

The tanks of the MF and UF/DF sections are made of stainless steel AISI 304; they are insulated and refrigerated in order to avoid temperature changes of their content which would compromise the quality of the extracted products; the tank size is of the same order of the hourly production.

6.6 NANO FILTRATION SECTION

The UF permeate if formed of water in which protein residual, B2 vitamin, lactose and mineral salts are diluted. In the NF process (also called low pressure IO process), and in the following IO process, a compatibility (solubility) is necessary between the solute and the membrane material, because the separation takes place for solubilization-diffusion (saline rejection).

In order to filter lactose and peptide residuals of the UF permeate, spiral polymeric membranes are employed with 200 Da molecular cut with an average productivity of about 46 l/(m² h) at an operating pressure of 15 bar [3].

As for the previous sections the operative cycle includes a 25 minutes filtering section followed by a 5 minutes back pulse washing.

The collecting tanks for permeates and retentates is made of

stainless steel AISI 304 (with size of the same order of the hourly production), of which only the retentate one is insulated.

6.7 REVERSE OSMOSIS SECTION

The IO filtration of the UF permeate, allows to obtain ultra-pure water as permeate and mineral salts (included the calcium bi-carbonate if added in the analysis section for the pH correction) as retentate, plus sugars and vitamins escaped from the NF treatment. In this section spiral polymeric membranes are employed having a rejection to NaCl of 99%, which guarantees a COD of the osmosis water lower than 150 mg/l of O₂ [7].

The average productivity of the membranes is around 30 l/(m² h) at an operating pressure of 30 bar [3]. The operating cycle requires the same durations of the previous stations. Also in this case it is possible to adopt a solution with components shared between NF and IO sections in the low flow rate cases.

The tank for collecting ultra-pure water is also made of stainless steel AISI 304, designed for containing the whole daily production. Part of the water produced is sent to the DF section for diluting the UF retentate.

7 SECONDARY LINES

7.1 BUTTER CREAM TREATING SECTION

Because of the low quantities of butter cream produced, a specific section for its treating is not considered and it will be sold to other firms for the transformation in butter. The product is stored in a stainless steel AISI 304 insulated tank designed for containing, like the other tanks for the separated products, the whole daily production.

7.2 TREATMENT SECTION FOR THE MICRO FILTRATION RETENTATE

The MF retentate is a watery solution in which fats and bacteria are suspended. For its transformation in powder it is necessary to evaporate the water in which the substances are diluted by means of a spray dryer. The retentate, suitably atomized, is introduced inside a chamber where it is invested by an hot air jet. The small water drops evaporate instantaneously, whereas the residual powder is first separated by a cyclone system and then collected in a tank. The powder collecting tank is made of stainless steel AISI 304.

7.3 TREATMENT SECTION FOR THE ULTRA FILTRATION RETENTATE

The UF retentate is a watery solution containing inside all the proteins present in the skimmed whey.

Like the MF retentate, the UF retentate is treated also in this case with a spray-dryer which reaches lower temperatures respect to the temperature of serum proteins denaturation (in the range 70÷75°C); at the same time, residual humidity values lower than those obtainable in a traditional evaporation process are guaranteed. For low flow rates, a single spray dryer can be employed, with

powder production alternatively from the MF and the UF retentate. The serum protein powder collecting tank is made of stainless steel AISI 304.

7.4 TREATMENT SECTION FOR THE NANO FILTRATION RETENTATE

The NF retentate is a watery solution containing diluted lactose. The lactose employed in the food-processing industry (food grade) is characterised by a purity of 97% which is obtained by the passage through the following stations: evaporator, crystallizer, centrifuge, dryer.

For the evaporation and the crystallization only one machine, the evaporative crystallizer is employed. The NF retentate, has an average lactose concentration of 170 g/l, insufficient for its correct crystallization, thus the evaporator has the function of increasing this concentration till 300 g/l. For the correct crystallization of the lactose a big size and a fast precipitation of the crystals are essential for not compromising the purity of the product by adsorbing or trapping internal impurities.

In order to obtaining a good quality product it is necessary that the lactose does not precipitate in the anhydrous shape β -lactose which is obtained at crystallization temperatures higher than 93,5 °C. The evaporative crystallizers work in vacuum conditions, with the advantage that the retentate treatment takes place at very low temperatures, thus reducing, in addition, the lactose deposits in the boiling chamber. This treatment implies an important reduction of the by-product volumes, because great part of the water contained in the NF retentate evaporates in the boiling tank. In general in the lactose treating processes solid mass concentrations in the range 75÷80% are reached, depending on the type of whey treated in the plant. The modern lactose crystallisation plants have an average global efficiency of 90%.

In the by-product of crystallisation, a very dense solution of water, crystallised lactose, riboflavin and peptide residuals, the separation of crystallised lactose and of the remaining substances takes place in mechanical way in a separation centrifuge, like happens in an automatic de-creamer.

After the centrifugation process the crystallised lactose is sent to the dryer where the residual humidity evaporates. The lactose, ready for the commercialisation, is collected in a stainless steel AISI 304 tank.

7.5 TREATMENT SECTION FOR REVERSE OSMOSIS PERMEATE

The IO retentate, being unusable for economical purposes, is sent to the dairy purifier, where, due to its low polluting charge, is disposed in conformity with the regulations. IO permeate, conversely, is ultra-pure water reused in the dairy both for washing operations (tanks, machines and membranes) and in the DF process.

8 ECONOMICAL ANALYSIS

For the economical analysis of the investment, the yearly cash flows are evaluated [8]. The costs are classified as

follows:

- Plant costs: land purchase and production facility building, design and testing, purchase and assembly of the treating and service plants components.
- Yearly operating costs: maintenance, energy, manpower.
- The yearly revenue obtained by the plant concern the following items:
 - Selling of the final products: butter cream, feed, concentrated serum proteins and FG lactose.
 - Savings deriving by the avoided industrial water purchase cost.
 - Savings deriving by the avoided whey disposal cost.

For the economical analysis, the following economical indicators are employed: Net Present Value (NPV), Net Present Value Ratio (NPVR), Rate Of Return (ROR), Pay Back Period (PBP).

8.1 PLANT COSTS

The cost for purchasing and assembling the whey treatment plant components is a function of the plant size.

The service plants necessary for a correct operation of the production plant are the electrical plant, the water plant, the steam and the pneumatic plants, whereas the CIP washing plant is the same which serves the dairy.

The plant also includes an hardware and a software system for the management and the automatic control of the production.

By analysing the size of the components of the different plant sections it emerges that the recovery plant size is limited and most of the space is occupied by the tanks for storing the retentates and the permeates.

For this kind of plant, about 50 m² of useful surface for each cubic meter of whey treated in an hour is evaluated. The plant area must include, in addition to the production plant, the area for the material loading and unloading and for the parking of the worker's vehicles. For this area, a surface twice the production plant area is considered. The costs for the plant design and testing are estimated as a percentage of the plant (production and service) and of the building costs.

This percentage is a function of the total costs amount.

The behaviour of the plant costs as a function of the plant capacity (treated flow rate) is shown in figure 5.

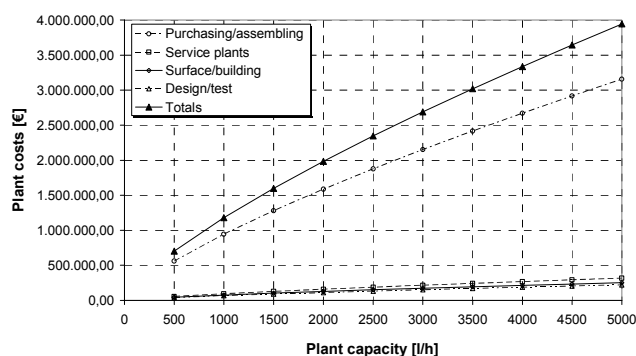


Figure 5 - Plant costs as a function of the plant capacity.

8.2 YEARLY OPERATING COSTS

The yearly costs for the regular maintenance of the plant are estimated at 3% of the initial plant cost. Every 3÷4 years, on average, the membranes of the filtration sections must be changed.

The energy costs are due to electric and pneumatic energy consumption and to the steam, and are evaluated on the base of the corresponding market cost.

For a correct plant operation, two operators for the plant management are required. The hourly gross cost of the manpower is evaluated in 16 €/h.

In figure 6 the behaviour of the yearly operating costs as a function of the plant capacity (treated flow rate) are shown.

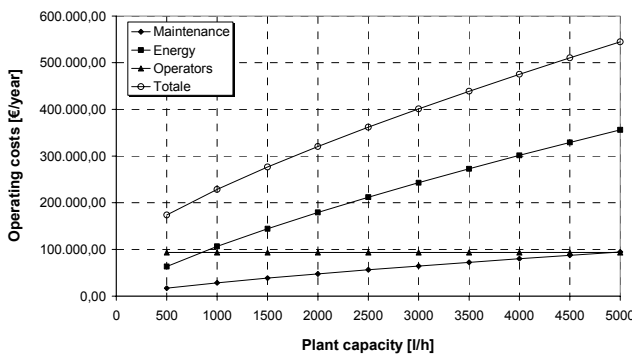


Figure 6 - Yearly operating costs as a function of the plant capacity.

8.3 INCOMES

The cost for the disposal of the treated whey varies in the range 3÷6 €/m³ of product to dispose. The recovery of high added value products determines a saving due to the avoided disposal, and this can be evaluated, on average, in about 4,5 €/m³.

The cost of the water for industrial purposes is 1,91 €/m³.

The main plant revenue is due to the marketing of the high added value products obtained by the treatment of the retentates whose selling prices are shown in table III.

Table III - Selling prices of the recovery products [1].

Product	Price [€/kg]
Butter cream	1,32
Animal feed	0,70
Concentrated serum proteins (WPC 80)	4,22
Lactose PG	1,189

In figure 7 the behaviour of the revenues as a function of the plant capacity (treated flow rate) is reported.

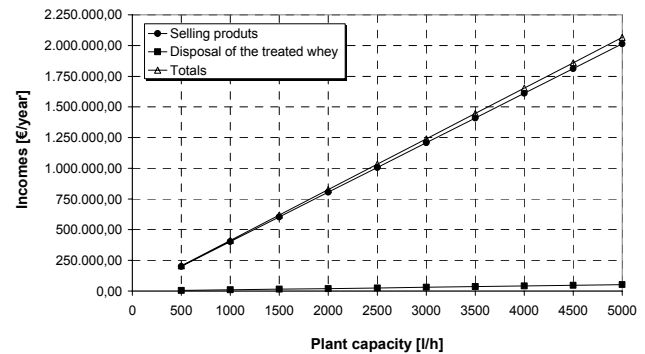


Figure 7 - Revenues as a function of the plant capacity.

8.4 SENSITIVITY ANALYSIS

A useful life of 10 years was estimated for the plant under investigation. For the economical analysis, a compound interest rate of 5% was assumed. For conservative reasons, full equity investment calculations were performed.

The behaviour of the cumulative NPV as a function of time for different values of the plant flow rate (in the range 500÷5000 l/h of whey) (see figure 8) was assumed as a basis for evaluating the curves of NPV, PBP and ROR as a function of the plant capacity (treated flow rate) (see figures 9-11).

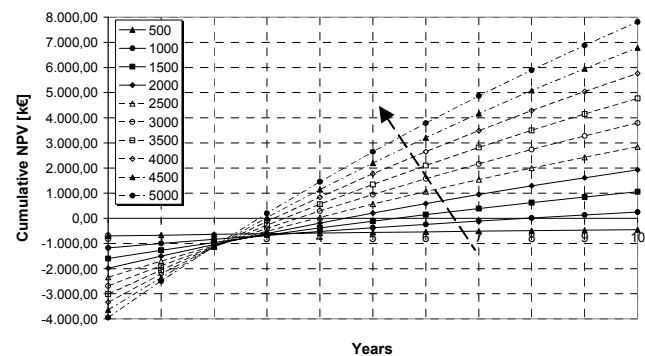


Figure 8 – Cumulative NPV versus time for different values of the plant capacity [l/h].

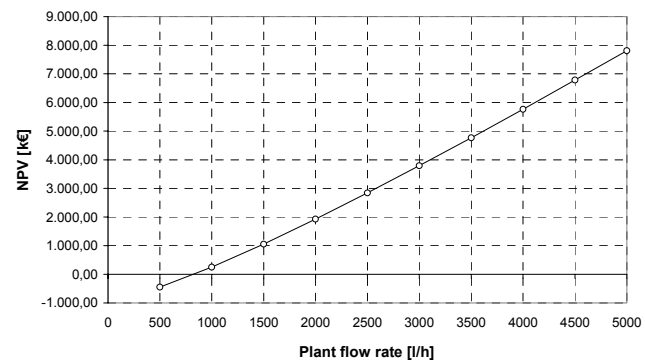


Figure 9 - NPV versus whey flow rate.

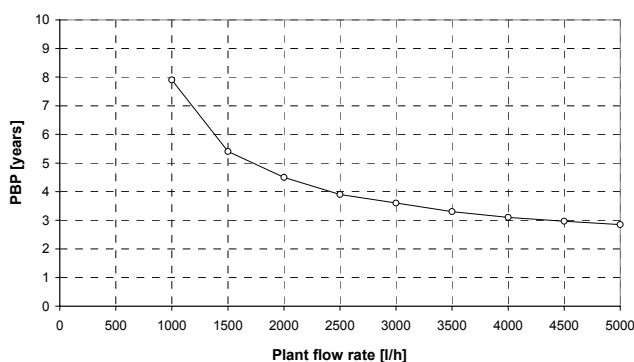


Figure 10 - PBP versus whey flow rate.

By analyzing the previous diagrams a growth of the plant profitability with the plant size emerges. A plant size of about 800 l/h corresponds to NPV=0. Above 800 l/h a positive economy emerges. A plant processing 5000 l/h, results in a NPV of about 8 M€. Vice versa, the system shows a negative economy if the plant processes 500 l/h. However, a plant size of about 2000 l/h determine PBP values around 4,5 years, which can be considered satisfactory values for industrial investments.

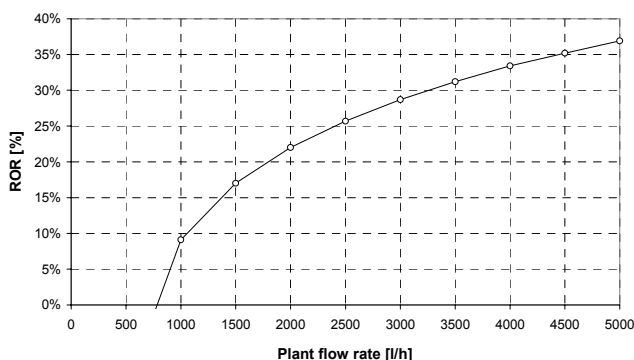


Figure 11 - ROR versus whey flow rate.

The behavior of ROR (see figure 11) also confirms the positive economy of the investment. In fact, still with little size plants, able to treat up to 1000 l/h, economic returns of about 10% are obtained.

Due to these results, the interest was focused on a medium size plant, able to treat 2500 l/h of ovine whey. This size would allow the disposal of the effluents from a medium size dairy located in Sardinia. The production of this plant would be fully absorbed by the market, which, up to now, is satisfied by the foreign imports.

Figure 12 shows the behavior of the cumulative NPV; it emerges that after 10 years, the NPV of the investment is about 2,84 M€ and the PBP, at which the initial investment can be recovered, is around 4 years. The ROR of the investment is 25,7%, a very good value for the kind of investment considered.

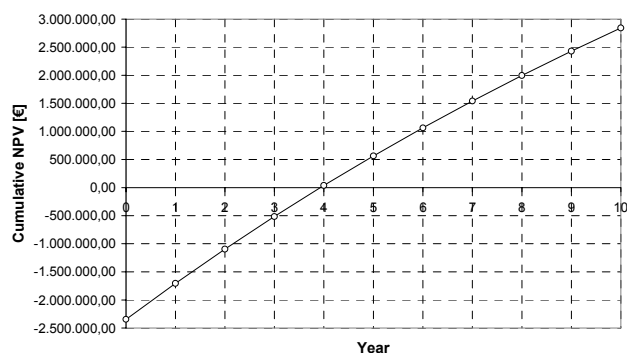


Figure 12 – Temporal behavior of the discounted cash flows.

By evaluating costs and incomes at the plant size considered for the economical analysis, a plant BEP of about 1375 l/h is obtained (see figure 13). This value is located at about 3/5 of the maximum productivity (2500 l/h). This means that positive profits can be obtained even in case of an important reduction of the average productivity.

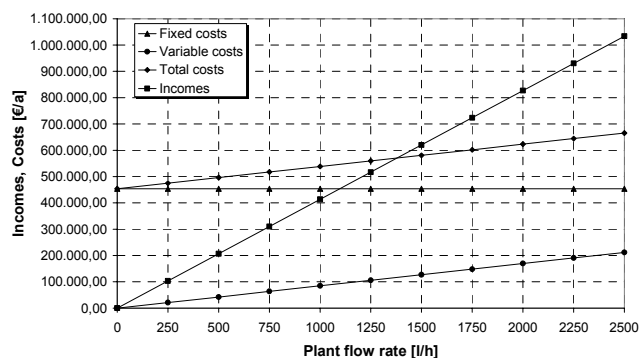


Figure 13 - BEP of the plant.

The NPVR is the ratio between the NPV and the discounted capital investment for the plant realisation (IPV – Investment Present Value). For a plant flow rate of 2500 l/h, the NPVR, indicating the economical return per unit of invested capital, is equal to 1,21.

By analysing the economical indicators employed, a positive economy of the investment for realising and operating the plant under investigation emerges.

Afterwards, a sensitivity analysis of the cumulative NPV as a function of time for different values of the compound interest rate was performed. The results obtained are reported in figure 14.

Moreover the behaviour of the different economical indicators as a function of the compound interest rate was analysed. The results obtained are reported in the figures 15-17.

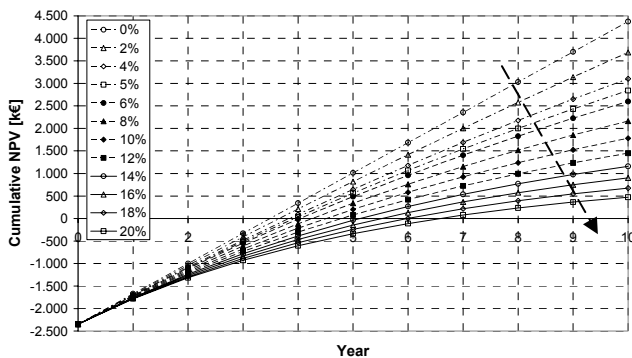


Figure 14 – Cumulative NPV versus time for different values of the interest rate.

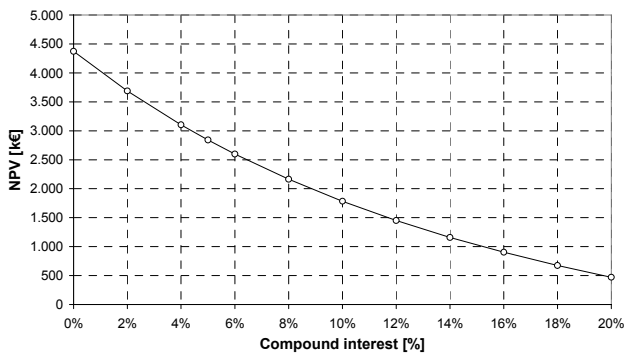


Figure 15 – NPV versus compound interest rate.

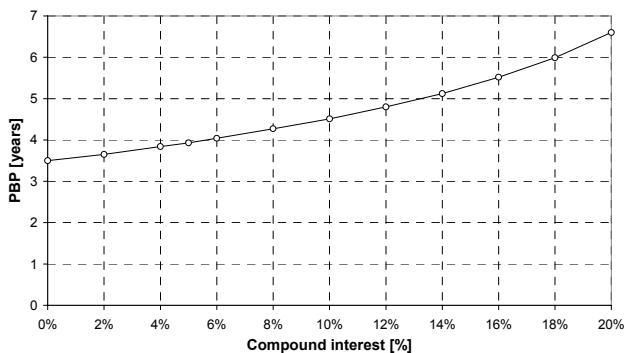


Figure 16 - PBP versus compound interest rate.

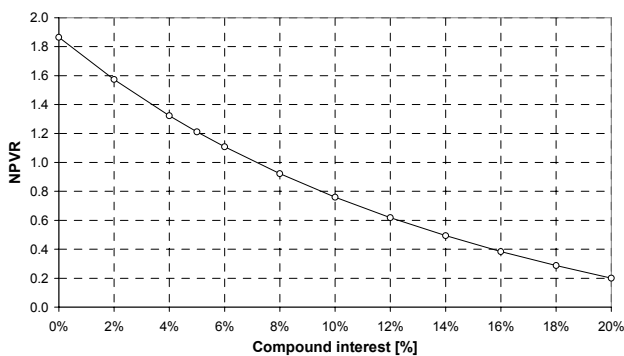


Figure 17 - NPVR versus compound interest rate.

By analysing the diagrams above, it emerges that positive returns always derive from the investment, with payback periods which arrive, in the worst case, to values around 6,5 years (see figure 16), which is still an acceptable value for an industrial investment.

NPVR varies inside the range $1,85 \pm 0,2$ (see figure 17). NPV varies between 4.400 k€ (with an interest rate of 0%) and 500 k€ (with an interest rate of 20%) (see figure 15).

Afterwards, a sensitivity analysis was performed by analysing the variations of both the selling price of some of the high added value products and the plant and the operating costs.

As far as the revenues are concerned, the selling price of the recovered products (milk cream, lactose FG, serum proteins) was varied one at a time within a range of $\pm 40\%$, leaving the remaining unchanged.

Similarly, both the plant and the operating costs were varied one at a time within the same range, the revenues remaining unchanged.

In figures 18-22, the corresponding variations of NPV, ROR and PBP with changes in revenues and costs are shown. The diagrams show positive values of the economical indicators even in presence of strong negative variations of the parameters.

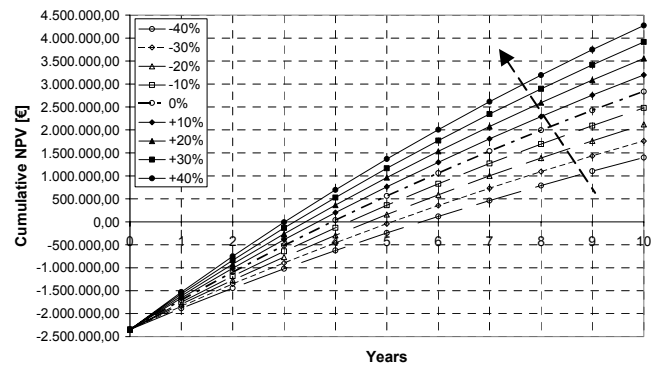


Figure 18 – Cumulative NPV versus time for different values of the selling price of the milk cream.

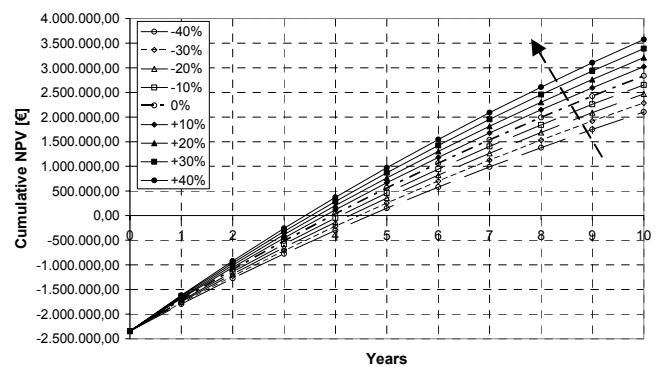


Figure 19 - Cumulative NPV versus time for different values of the selling price of the milk cream.

values of the selling price of the serum proteins.

By analysing figure 18, it can be observed that, starting from an initial PBP value of 4 years, a positive variation of 40% in the selling price of the milk cream determines a PBP reduction up to 3 years; vice versa, the same negative reduction results in a PBP increase up to 5,7 years.

The NPV, at the beginning equal to 2,9 M€, for the above mentioned variation of $\pm 40\%$, changes between 1,5 and 4,25 M€.

Figure 19 shows more thickened results around the nominal value: the variations of PBP as a function of the selling price of the serum proteins are by far less wide respect to those deriving from the variations of the selling price of the milk cream.

In fact a positive variation of 40% of the selling price of the serum proteins determines a reduction of the PBP up to 3,5 years, while the same negative variation of the selling price results in an increase of the PBP up to 4,7 years.

The same maximum variations correspond to changes in the NPV value in the range 2,1÷3,6 M€, which is a lower variation respect to the one registered in the case of the selling price of the milk cream.

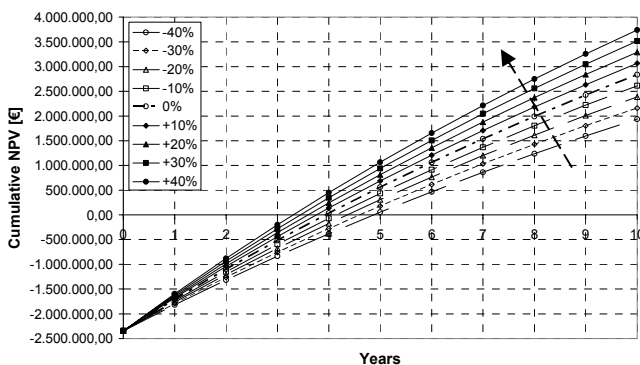


Figure 20 - Cumulative NPV versus time for different values of the selling price of the lactose FG.

Variations of $\pm 40\%$ of the selling price of the lactose FG result in values of the PBP in the range 3,2÷4,9 years and in values of the NPV between 2,0÷3,8 M€.

By analysing the previous diagrams, it turns out that, percentage variation being equal, the variation of the selling price of the milk cream has the major positive and negative influence on the economical indicators investigated.

Variations of the plant cost (see figure 21) result in important oscillations of the NPV and of the PBP of the investment. In particular, the PBP varies from 2,3 years, for a negative reduction of 40% of the plant cost, to 5,8 years for the same positive variation. In parallel, NPV oscillates between 1,9 and 3,8 M€.

In figure 22 the cumulative NPV versus time for different values of the operating costs is illustrated. In this case the oscillations of the economical indicators employed are moderate respect to the same percentage variations of the plant costs.

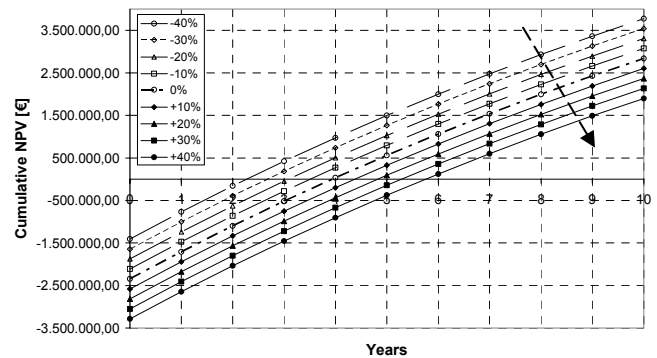


Figure 21 - Cumulative NPV versus time for different values of the plant costs.

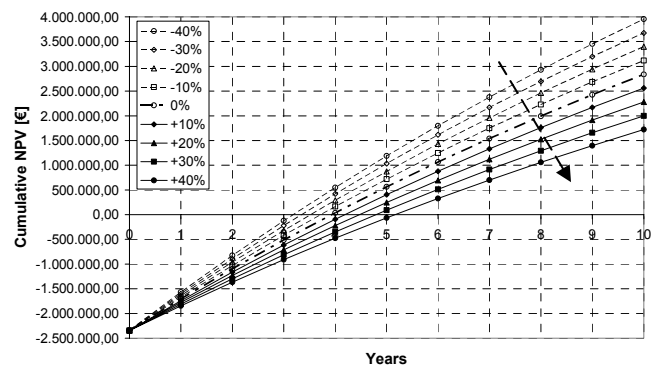


Figure 22 - Cumulative NPV versus time for different values of the operating costs.

Figures 23-25 illustrate the behaviour of NPV, ROR and PBP as a function of the percentage variation of the selling price of the recovered products (milk cream, WPC80, lactose FG) and of the costs (plant costs and operating costs).

The first diagram (figure 23) shows how the parameter with the highest influence on the NPV is the selling price of the milk cream. Vice versa, the variations of the plant costs determine the greater oscillations of ROR and PBP (see figures 24-25).

By analysing all the diagrams, it emerges that, among the different parameters on which it is possible to operate for increasing the investment profitability, the most convenient one is represented by the plant costs rather than by the operating costs; whereas minor influence have the variations of the selling price of the recovered products.

However it must be kept in mind that all the sensitivity analysis are based on a serum flow rate of 2500 l/h. In this regard it must be observed that, at national level, most of the request of high added value products derived from whey is presently satisfied by foreign imports. It is therefore reasonable to believe that the national market could be able to absorb the final products obtained from the plant.

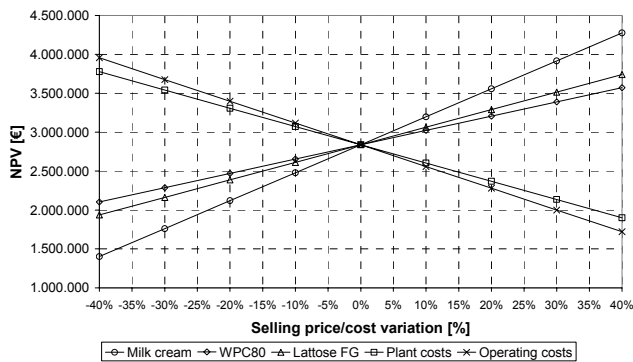


Figure 23 - NPV curves as a function of the variations of the selling price of the final products and of the costs.

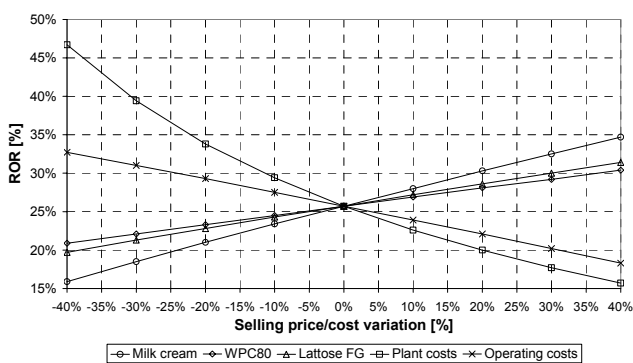


Figure 24 - ROR curves as a function of the variations of the selling price of the final products and of the costs.

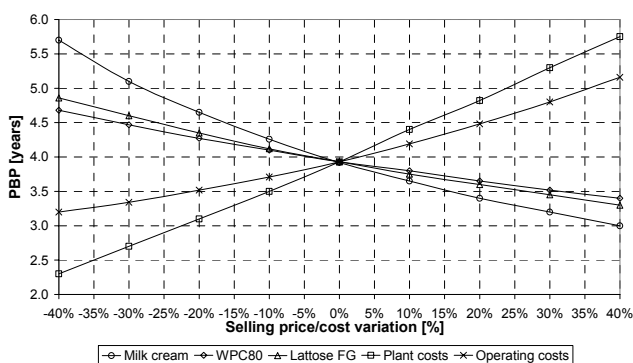


Figure 25 - PBP curves as a function of the variations of the selling price of the final products and of the costs.

9 CONCLUSIONS

In this paper the technical and economical feasibility study of the realisation of a plant located in Sardinia for treating ovine whey was performed.

This realisation would allow to eliminate the problem of disposing the waste of the Sardinian dairy production presently employed as a feed for the zootechnic industry, for which the quantity of milk produced shows a growing trend.

The twofold target is to eliminate the problem of the disposal of a very polluting component, recovering, at the

same time, high added value components (butter cream, zootechnic feed, serum proteins WPC 80, lactose and ultra-pure water).

The plant structure is formed by a primary production line (creaming sections, MF, UF and DF, NF and IO), from which the gross by-products are obtained, and by some secondary lines, in which their refining takes place.

The plant scale-up was performed, and, for a plant size of 2500 l/h of elaborated whey, the economical analysis allowed to calculate an investment NPV of 2,84 M€, an NPVR of 1,21 and a discounted PBP of about 4 years. The BEP is about 1375 l/h. By analysing all the diagrams, it emerges that, among the different parameters on which it is possible to operate for increasing the investment profitability, the most convenient one is represented by the plant costs rather than by the operating costs; whereas minor influence have the variations of the selling price of the recovered products.

REFERENCES

- [1] <http://www.clal.it>
- [2] D.Lgs. n.22/1997 (Legge Ronchi), "Attuazione delle Direttive 91/156/CEE sui Rifiuti, 91/689/CEE sui Rifiuti Pericolosi e 94/62/CE sugli Imballaggi e sui Rifiuti di Imballaggio".
- [3] Pizzichini M., *Tecnologie di Processo per il Recupero e la Valorizzazione delle Componenti del Siero di Latte*, Ed. ENEA, 2003.
- [4] <http://www.bayer.com>
- [5] Pizzichini M., Montani R., Ruscio F., *Il Siero di Latte: da Rifiuto Zootechnico a Materia per Alimenti e Farmaci*, L'Informatore Agrario, No. 16, pp. 49-52, 2001.
- [6] Pizzichini M., Iasonna A., Rosi M., Ruscio F., Erbisti F., *L'Innovazione Tecnologica nell'Industria Lattiero-Casearia*, Energia Ambiente Innovazione Ed. ENEA, No. 1, pp. 43-57.
- [7] Pizzichini M., *Recupero di Sieroproteine e Acqua Depurata dalla Scotta Ovina con Tecnologie di Membrana*, Scienza e Tecnica Lattiero-Casearia, No. 46, pp. 361-379, 1995.
- [8] Pizzichini M., Russo C., Erbisti F., *Prodotti ad Alto Valore Biologico dal Siero di Caseificazione*, AGRICulture, No. 3, pp. 15-19.

TEMPLATE FOR PREPARING PAPERS FOR PUBLISHING IN INTERNATIONAL JOURNAL OF MECHANICS AND CONTROL

Author1* Author2**

* affiliation Author1

** affiliation Author2

ABSTRACT

This is a brief guide to prepare papers in a better style for publishing in International Journal of Mechanics and Control (JoMaC). It gives details of the preferred style in a template format to ease paper presentation. The abstract must be able to indicate the principal authors' contribution to the argument containing the chosen method and the obtained results. (max 200 words)

Keywords: keywords list (max 5 words)

1 TITLE OF SECTION (E.G. INTRODUCTION)

This sample article is to show you how to prepare papers in a standard style for publishing in International Journal of Mechanics and Control.

It offers you a template for paper layout, and describes points you should notice before you submit your papers.

2 PREPARATION OF PAPERS

2.1 SUBMISSION OF PAPERS

The papers should be submitted in the form of an electronic document, either in Microsoft Word format (Word'97 version or earlier).

In addition to the electronic version a hardcopy of the complete paper including diagrams with annotations must be supplied. The final format of the papers will be A4 page size with a two column layout. The text will be Times New Roman font size 10.

2.2 DETAILS OF PAPER LAYOUT

2.2.1 Style of Writing

The language is English and with UK/European spelling. The papers should be written in the third person. Related work conducted elsewhere may be criticised but not the individuals conducting the work. The paper should be comprehensible both to specialists in the appropriate field and to those with a general understanding of the subject.

Company names or advertising, direct or indirect, is not permitted and product names will only be included at the discretion of the editor. Abbreviations should be spelt out in full the first time they appear and their abbreviated form included in brackets immediately after. Words used in a special context should appear in inverted single quotation mark the first time they appear. Papers are accepted also on the basis that they may be edited for style and language.

2.2.2 Paper length

Paper length is free, but should normally not exceed 10000 words and twenty illustrations.

2.2.3 Diagrams and figures

Figures and Tables will either be entered in one column or two columns and should be 80 mm or 160 mm wide respectively. A minimum line width of 1 point is required at actual size. Captions and annotations should be in 10 point with the first letter only capitalised *at actual size* (see Figure 1 and Table VII).

Contact author: author1¹, author2²

¹Address of author1.

²Address of author2 if different from author1's address.

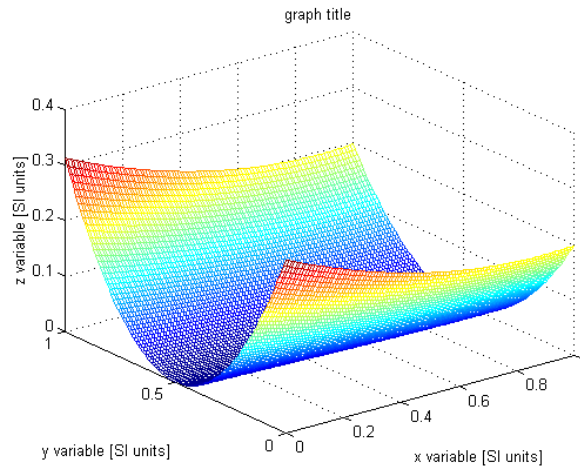


Figure 1 Simple chart.

Table VII - Experimental values

Robot Arm Velocity (rad/s)	Motor Torque (Nm)
0.123	10.123
1.456	20.234
2.789	30.345
3.012	40.456

2.2.4 Photographs and illustrations

Authors could wish to publish in full colour photographs and illustrations. Photographs and illustrations should be included in the electronic document and a copy of their original sent. Illustrations in full colour ...

2.2.5 Equations

Each equation should occur on a new line with uniform spacing from adjacent text as indicated in this template. The equations, where they are referred to in the text, should be numbered sequentially and their identifier enclosed in parenthesis, right justified. The symbols, where referred to in the text, should be italicised.

- point 1
 - point 2
 - point 3
- 1. numbered point 1
- 2. numbered point 2
- 3. numbered point 3

$$W(d) = G(A_0, \sigma, d) = \frac{1}{T} \int_0^{+\infty} A_0 \cdot e^{-\frac{d^2}{2\sigma^2}} dt \quad (1)$$

3 COPYRIGHT

Authors will be asked to sign a copyright transfer form prior to JoMaC publishing of their paper. Reproduction of any part of the publication is not allowed elsewhere without permission from JoMaC whose prior publication must be cited. The understanding is that they have been neither previously published nor submitted concurrently to any other publisher.

4 PEER REVIEW

Papers for publication in JoMaC will first undergo review by anonymous, impartial specialists in the appropriate field. Based on the comments of the referees the Editor will decide on acceptance, revision or rejection. The authors will be provided with copies of the reviewers' remarks to aid in revision and improvement where appropriate.

5 REFERENCES (DESCRIPTION)

The papers in the reference list must be cited in the text. In the text the citation should appear in square brackets [], as in, for example, "the red fox has been shown to jump the black cat [3] but not when...". In the Reference list the font should be Times New Roman with 10 point size. Author's first names should be terminated by a 'full stop'. The reference number should be enclosed in brackets.

The book titles should be in *italics*, followed by a 'full stop'. Proceedings or journal titles should be in *italics*. For instance:

REFERENCES (EXAMPLE)

- [1] Smith J., Jones A.B. and Brown J., *The title of the book*. 1st edition, Publisher, 2001.
- [2] Smith J., Jones A.B. and Brown J., The title of the paper. *Proc. of Conference Name*, where it took place, Vol. 1, paper number, pp. 1-11, 2001.
- [3] Smith J., Jones A.B. and Brown J., The title of the paper. *Journal Name*, Vol. 1, No. 1, pp. 1-11, 2001.
- [4] Smith J., Jones A.B. and Brown J., *Patent title*, U.S. Patent number, 2001.

International Journal of Mechanics and Control – JoMaC
Published by Levrotto&Bella
TRANSFER OF COPYRIGHT AGREEMENT

<p>NOTE: Authors/copyright holders are asked to complete this form signing section A, B or C and mail it to the editor office with the manuscript or as soon afterwards as possible.</p>	<p><i>Editor's office address:</i> Andrea Manuello Bertetto Elvio Bonisoli <i>Dept. of Mechanics</i> <i>Technical University – Politecnico di Torino</i> <i>C.so Duca degli Abruzzi, 24 – 10129 Torino – Italy</i> <i>e_mail: jomac@polito.it</i> <i>fax n.: +39.011.564.6999</i></p>
--	---

The article title:

By: _____

To be Published in *International Journal of Mechanics and Control JoMaC*
Official legal Turin court registration Number 5320 (5 May 2000) - reg. Tribunale di Torino N. 5390 del 5 maggio 2000

- A Copyright to the above article is hereby transferred to the JoMaC, effective upon acceptance for publication. However the following rights are reserved by the author(s)/copyright holder(s):
1. All proprietary rights other than copyright, such as patent rights;
 2. The right to use, free or charge, all or part of this article in future works of their own, such as books and lectures;
 3. The right to reproduce the article for their own purposes provided the copies are not offered for sale.
- To be signed below by all authors or, if signed by only one author on behalf of all co-authors, the statement A2 below must be signed.*

A1. All authors:

SIGNATURE _____ DATE _____ SIGNATURE _____ DATE _____

PRINTED NAME _____ PRINTED NAME _____

SIGNATURE _____ DATE _____ SIGNATURE _____ DATE _____

PRINTED NAME _____ PRINTED NAME _____

A2. One author on behalf of all co-authors:

"I represent and warrant that I am authorised to execute this transfer of copyright on behalf of all the authors of the article referred to above"

PRINTED NAME _____

SIGNATURE _____ TITLE _____ DATE _____

B. The above article was written as part of duties as an employee or otherwise as a work made for hire. As an authorised representative of the employer or other proprietor. I hereby transfer copyright to the above article to Editel-Pozzo Gros Monti effective upon publication. However, the following rights are reserved:

1. All proprietary rights other than copyright, such as patent rights;
2. The right to use, free or charge, all or part of this article in future works of their own, such as books and lectures;
3. The right to reproduce the article for their own purposes provided the copies are not offered for sale.

PRINTED NAME _____

SIGNATURE _____ TITLE _____ DATE _____

C. I certify that the above article has been written in the course of employment by the United States Government so that no copyright exists, or by the United Kingdom Government (Crown Copyright), thus there is no transfer of copyright.

PRINTED NAME _____

SIGNATURE _____ TITLE _____ DATE _____

CONTENTS

3 Low Cost Indoor Navigation System for Autonomous Vehicle

S. Chiesa, V. De Iakovo, G. Malnati, M. Murciano, K. M. Pluciński, F. Stesina, C. Zunino

17 Comparison between Damage Criteria in Thermo-Mechanical Fatigue

C. Delprete, C. Rosso, R. Sesana

27 Effects of Nonlinearities and Control Law Selection on Active Flutter Suppression

L. Borello, G. Villero, M. Dalla Vedova

41 Dynamic Analysis of a Spur Gear under Moving Load

T. Jingwei, X. Buqing, W. Shibin, B. Picasso

47 Technical and Economic Analysis for the Recovery of High Biological Value Products from the Cheese-Making Whey

P. F. Orrù, M. T. Pilloni

next number scheduled titles:

Robot Driven by Parallel Bicycles

M.Q. Feng, T. Kawamura, K. Yamafuji

Lifting up Modulus for Lunar Rover Vehicle

A. Manuello Bertetto, C. Falchi

Nonlinear Elastic Characteristic of Magnetic Suspensions through Hilbert Transform

E. Bonisoli

Kinematics Survey of Swift Harvesting Handle by High Speed Camera

A. Manuello Bertetto, R. Ricciu

High Deformation Strain Gauge for non Conventional Robotics

W. Franco, D. Maffiodo, A. Manuello Bertetto